Near-Nozzle Holographic Imaging of Dispersion-Induced Reductions in Combustible Dust Particle Size Distributions

Tyler James Reaker
Marquette University

Recommended Citation

Reaker, Tyler James, "Near-Nozzle Holographic Imaging of Dispersion-Induced Reductions in Combustible Dust Particle Size Distributions" (2021). *Master's Theses (2009 -)*. 650.
https://epublications.marquette.edu/theses_open/650

NEAR-NOZZLE HOLOGRAPHIC IMAGING OF DISPERSION-INDUCED REDUCTIONS IN COMBUSTIBLE DUST PARTICLE SIZE DISTRIBUTIONS

by

Tyler J. Reaker, B.S.M.E

A Thesis submitted to the Faculty of the Graduate School,
Marquette University,
in Partial Fulfillment of the Requirements for
the Degree of Master of Science

Milwaukee, Wisconsin

May 2021

ABSTRACT
NEAR-NOZZLE HOLOGRAPHIC IMAGING OF DISPERSION-INDUCED REDUCTIONS IN COMBUSTIBLE DUST PARTICLE SIZE DISTRIBUTIONS

Tyler J. Reaker, B.S.M.E

Marquette University, 2021

Dust explosibility data are a critical input to the design of equipment and strategies for reducing the risk of a combustible dust deflagration or explosion. These data, which include minimum explosible concentrations, deflagration indices, and explosion overpressures, are obtained using formally accepted, standard techniques, and are known to be sensitive to the particle size characteristics of the dust being evaluated. Published literature demonstrates that the standard techniques can alter the particle size distribution during dispersion, making interpretation of the explosibility data challenging because the particle characteristics are altered from their original, raw state. Digital in-line holography (DIH) presents a novel method for measuring airborne dust particle size distributions and imaging three-dimensional particle flows during dispersion to characterize the changes to the particle size characteristics and to investigate the underlying mechanisms.

In this work, a DIH imaging system was designed to work in conjunction with a dust dispersion system to capture particle size distributions of dust clouds exiting a nozzle. The image capture system utilizes a 21 mW helium-neon laser to create a hologram of pressurized dust as it passes through a nozzle and into a 2.5 L chamber. A study conducted to quantify the resolution of holographic particle location, established an average in-plane resolution of 10.51 µm with a lens and 20.31 µm without a lens. The residual standard error for axial measurements taken of a resolution target, sugar particles, and lycopodium particles ranged from 80.41 – 146.19 µm without a camera lens and 66.63-98.58 µm with magnification from a camera lens.

Holographic analysis of dispersion videos of non-brittle (lycopodium) and brittle (ascorbic acid) dust, using HoloSand analysis tools, resulted in less than 15% reduction in particle size for lycopodium and more than 50% reduction for ascorbic acid. The particle size distribution of the ascorbic acid was also shown to decrease with an increase in dispersion pressure. The scale of the particle distribution change for both materials was consistent with results from previous studies using the 20-L Siwek vessel, validating the dispersion and DIH imaging method.

ACKNOWLEDGMENTS

Tyler J. Reaker, B.S.M.E

I would first like to express my sincere appreciation to my advisor Dr. Casey Allen, for encouraging me to return to Marquette to work on research and for serving as my mentor through the last two years. Your guidance has helped me become a better engineer and researcher. Thank you for always challenging me and for being there to discuss questions or bounce ideas off. I have learned a lot from working with you and will miss working together.

I would also like to thank those who provided support and technical assistance on this project: Dr. Ashok Dastidar, Zach Hachmeister, and Rachelle Andreasen for their assistance with particle sizing of the raw samples and for financial support of the vessel apparatus, Dr. Daniel Guildenbecher of Sandia National Laboratories for all of your help with the customization and use the HoloSand program, and Dr. Raymond Fournelle for the SEM particle analysis.

Thank you to my thesis committee of Dr. Somesh Roy and Dr. Simcha Singer for your valuable feedback on my research and for all that you have taught me in the classroom.

I owe a huge thanks to my parents for igniting my love of learning that has kept me going through this process and allowed me to reach this milestone. I am who I am today because of all of the love and support you have shown me through every phase of my life. Also, thank you to my brother Austin for setting the example by always following your dreams and encouraging me to do the same.

I would also like to thank my incredible wife Sara for all the sacrifices she has made, which have allowed me to pursue this degree. Your love and friendship have helped me get through the stress and challenges of the past two years, and there is no way I could have done it without you. You’re my best friend and every day with you is better than the last.

Last but not least, I want to thank my dog Sadie for being my co-worker throughout the past year. You never fail to cheer me up and make me feel loved.

TABLE OF CONTENTS

LIST OF TABLES

LIST OF FIGURES

CHAPTER 1

INTRODUCTION

The risk of dust explosions is a major concern for those working in the manufacturing and processing industries. Although the National Fire Protection Association (NFPA) has established several standards for the safe handling of combustible dust and ASTM standard test procedures exist to characterize the explosibility behavior of a material, accidents continue to occur, causing severe injuries and loss of life. Between 2006 and 2017, the US Chemical Safety and Hazard Investigation Board (CSB) identified 105 “dust incidents,” resulting in 303 injuries and 59 deaths [41]. The continued occurrence of these incidents led the CSB to release a “Call to Action” in October of 2018 in order to understand why the ”efforts to manage [dust] hazards have often failed to prevent a catastrophic explosion” [40].

To adequately assess and mitigate the risk posed by combustible dust, standard testing procedures have been developed to quantify the ignition sensitivity and ignition severity for a specific dust material. These procedures generally involve using pressurized air to disperse dust into an enclosed chamber (e.g., ASTM E1226 and ISO 6184-1). The two most common chamber sizes are 1 m^3 and 20-L (known as the Siwek vessel). The explosibility parameters measured by these tests are dependent on the conditions in the dust cloud when the ignition source is initiated, which are not always representative of the raw input sample for the test or the nominal concentration loaded in the apparatus. For example, changes in particle size during the dispersion process resulting from particle breakage have been shown to cause a significant difference between the expected and actual concentrations in testing chambers [24]. Furthermore, dust reactivity (e.g., ignition severity) is inversely proportional to particle size, thus particle breakage leads to enhanced reactivity relative to the raw sample loaded into the test. This behavior is problematic because the measured explosibility data are used to design explosion protection measures, and overly conservative and costly strategies may be unnecessarily implemented based on data that are influenced by the non-ideal effects described here.

Characterization of particle breakage behavior during sample dispersion is important for understanding the extent to which material properties are altered during a test. Holography presents a novel technique for recording the particle size distribution of dust as it is dispersed through a nozzle and into a combustion chamber. This study details the design of a holographic imaging system and a dust dispersion system used in combination with holographic imaging software to measure changes in particle distribution sizes during the dispersion process. By comparison with previous studies of particle breakage in the dispersion process, this work aims to validate the ability of this experimental method to detect and measure particles exiting the nozzle, allowing for the possibility of further holographic analysis of the dispersion process.

1.1 Thesis Outline

This thesis begins in Chapter 2 with a background introduction to holography and the formation of the scalar diffraction integrals, which form the mathematical basis of holographic imaging. The three main image reconstruction methods used with holography are explained, along with several focusing, particle locating, and particle tracking methods utilized in this system.

Chapter 3 provides an overview of the current method of characterizing combustible dust. A review of the current research into particle breakage during the dispersion process and the dynamics of dust clouds in the dispersion chamber concludes Chapter 3.

Chapter 4 details the design of the optical system for creating hologram images of the dust dispersion system. In addition to the component selection and design, a description of the method for setting up and calibrating the collimating lens and magnification lens is included.

Chapter 5 provides resolution analysis to quantify the ability of this optical system to locate objects and dust particles in three-dimensional space. An initial background on the theoretical basis for holographic resolution is provided, along with a description of the python code used for the studies. The resolution of the system is calculated using a USAF 1951 target, sugar, and lycopodium, and analysis is performed with and without a magnifying lens on the camera.

Chapter 6 describes the dust dispersion system design used to investigate particle breakage. Initial testing of the system at different initial pressures and solenoid timings is used to characterize how changes to system parameters can be used to adjust the flow of the dust through the nozzle and into the chamber.

Combining the holographic imaging system described in Chapters 4 and 5 with the dust dispersion system developed in Chapter 6, Chapter 7 demonstrates the ability of this system, in combination with Sandia Particle Holography Processor software, to measure particle size distributions of the near-nozzle flow. The post-dispersion particle size distributions for lycopodium and ascorbic acid are compared to the pre-dispersion distributions, and the change in particle size is compared to previous results from other dispersion chambers.

Chapter 8 provides a summary of the results along with a discussion of future work in this area. This future work includes expansions of the dispersion tests to a broader range of materials, pressures, and nozzle designs, investigation of other holographic imaging methods, including DIH-PIV, and investigation into shock wave distortion removal for imaging closer to the dispersion nozzle.

CHAPTER 2

DIGITAL HOLOGRAPHY IN PARTICLE SIZING AND TRACKING

Holography, a method of image capture developed by Dennis Gabor in 1948, involves recording and reconstructing both the phase and amplitude of a light wave field [43]. This method differs from traditional photography, which only records the amplitude of light waves. The additional encoding of phase information in the image allows for complete image reconstruction with all the necessary information required to appear 3D to the human eye [34]. In addition to its use in realistic image creation, the phase information contained in a hologram can be used to determine the depth or three-dimensional location of an object. This feature of holography makes it useful in a number of scientific applications, including holographic interferometry [2], topography [33], microscopy [25], stress-strain analysis [43], and fluid dynamics [29]. In this work, holography is used to record and reconstruct the dimensions and locations of dust particles in three dimensions.

The creation of a hologram image requires recording the interference between a coherent reference wave of light and a light wave scattered by the object of interest. Most holograms require a monochromatic and coherent light source and are therefore created using a laser as the reference light wave. Figure 2.1a shows the most basic hologram recording setup, known as in-line holography, consisting of a laser beam scattering as it passes an object. The combination of this scattered object wave and the unscattered reference wave, which has passed around the object unaffected, creates an interference pattern on a piece of film. This image is known as the hologram. Reconstruction of this hologram image involves passing the reference beam back through the recorded hologram image, which results in the appearance of a real and virtual image, as

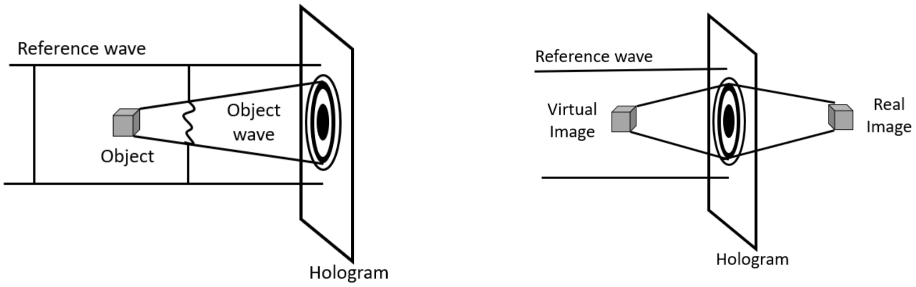

(a) Hologram capture (b) Reconstruction

Figure 2.1: Image capture and reconstruction of an in-line hologram

shown by Figure 2.1b.

With the development of digital cameras, the hologram recording and reconstruction process can now be performed digitally in what is known as digital holography [43]. The general method of using digital in-line holography (DIH) for object locating involves the following steps. First, a hologram image is captured using a digital camera (usually CCD or CMOS) which records the interference pattern between the object and reference waves. The object image is then reconstructed using either the Fresnel, convolution, or angular spectrum method. Section 2.2 provides more background on each of these methods and the reasoning behind the use of the convolution method for particle location and tracking with holography. These reconstruction methods consist of numerically solving the Fresnel-Diffraction integral at an axial distance from the camera in order to recreate the original object image at that location. A detailed description of the development of this integral from the general scalar wave theory of light is provided in Section 2.1.

By reconstructing the 2D object image at different locations along the axial path of the beam, the propagation of the light from the object to the camera becomes apparent. Similar to dropping a pebble into a lake, the object causes a ripple pattern in the light wave, which spreads out as it moves farther away from

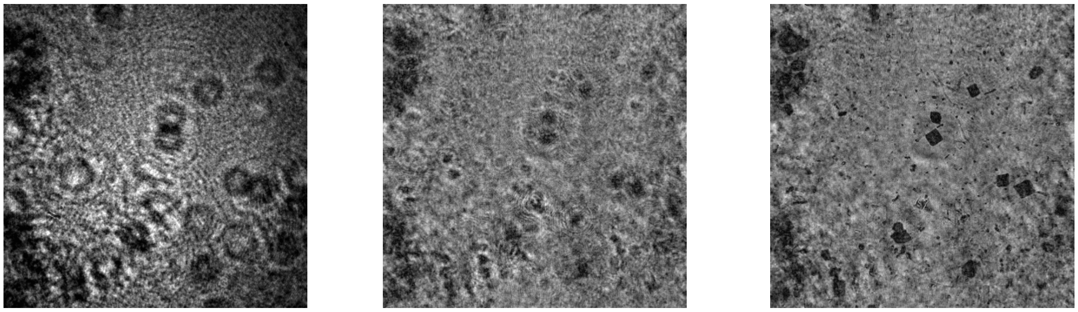

(a) Hologram image (b) Unfocused distance (c) Focused distance

Figure 2.2: Reconstruction of a hologram of sugar particles at two distances

the object. When the hologram image is numerically reconstructed at the original particle location, these ripples collapse back into an in-focus image of the object. This phenomenon can be seen in Figure 2.2, which shows a hologram image of sugar particles (2.2a), along with images that are numerically reconstructed at an out-of-focus distance (2.2b) and an in-focus distance (2.2c).

When holography is utilized in three-dimensional particle locating, each hologram image is reconstructed multiple times over a range of distances to create an array of slices that make up the image field for that hologram. By cycling through this field of images and finding the image in which the particle of interest is in focus, the axial location of that particle can be determined. To use this locating process, some quantitative variable must be assigned to the image to identify when an object is in focus. There are a number of different methods for determining the in-focus image and, therefore, the distance from the camera to the object. A more detailed description of some of these methods is provided in Section 2.3.

Section 2.1 begins this chapter with a review of the mathematical equations which create the foundation for DIH. Next, the four steps of hologram image processing are presented in the subsequent sections, as summarized in Figure 2.3. For each step, several possible methods are discussed further. The first three steps

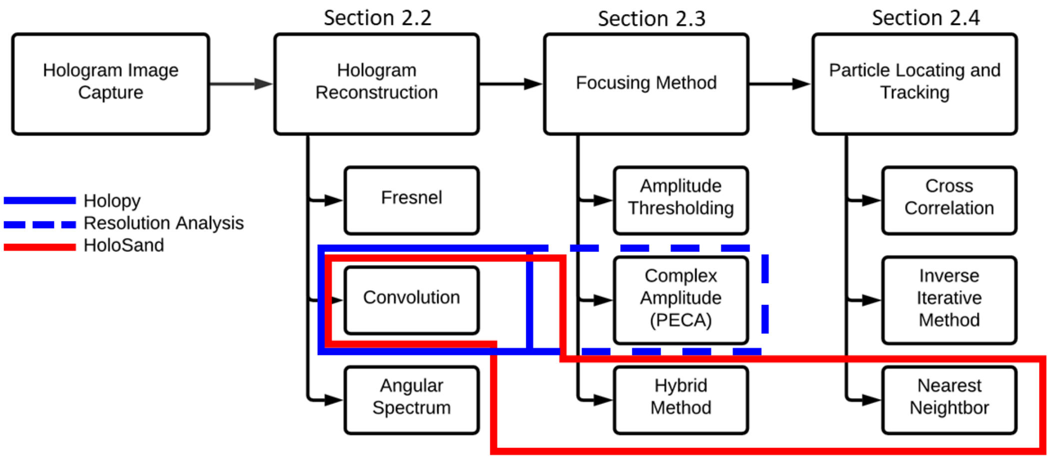

Figure 2.3: Summary of hologram processing methods and software packages

are used to record the image resolutions discussed in Chapter 5 and measure the particle size distribution results presented in Chapter 7. The methods implemented for this analysis in the HoloPy/ResAnalysis (Section 5.3) and HoloSand (Section 7.1) programs are highlighted in Figure 2.3. Although not utilized in this work, particle locating and tracking methods are also included in Section 2.4 for reference as a likely focus of future work. The addition of this step to the process allows for flow field reconstruction through particle image velocimetry (PIV) which could serve as a valuable tool for future analysis of dust concentration and turbulence in the chamber.

2.1 Scalar Diffraction

What follows is a short introduction to the formulation of the equations that describe the scalar diffraction of light, and a brief discussion of the methods and approximations used. The resulting Fresnel diffraction integral will be used to model light propagation and will serve as the foundation of the hologram reconstruction methods described in Section 2.2

2.1.1 Development of the Huygen's-Fresnel Diffraction Integral

When modeling light as a three-dimensional wave, its propagation through space can be modeled by the scalar wave equation

$$\nabla^2 u - \frac{n^2}{c^2}\frac{\partial^2 u}{\partial t^2} = 0, \tag{2.1}$$

where n is the refractive index of the medium in which the wave is traveling ($n = 1$ for air), u is the field, t is time, and c is the speed of light ($3 * 10^8$ m/s). This equation can be rewritten using the form of a spherical wave of amplitude A at location P,

$$U(P) = A(P)e^{-j2\pi\nu t} \tag{2.2}$$

as

$$(\nabla^2 + k^2)U = 0, \tag{2.3}$$

which is known as the Helmholtz equation [19]. The k term in this equation is known as the wave number

$$k = \frac{2\pi}{\lambda} = \frac{2\pi n\nu}{c} \tag{2.4}$$

where λ is the wavelength and ν is the frequency of the light.

To solve the Helmholtz equation, Green's theorem can be used to formulate a solution which in turn can be solved through integration. What follows is a summary of this method and the two resulting diffraction formulae, the derivation of which is thoroughly detailed by Goodman [19]. The use of Green's theorem requires the selection of an auxiliary function and boundary conditions. In his solution, Kirchhoff used an auxiliary equation for a spherical wave at point 1 (P_1)

$$G\left(P_1\right) = \frac{e^{jkr_{01}}}{r_{01}} \tag{2.5}$$

and a boundary condition consisting of an aperture on a screen on the edge of this expanding wave as shown in Figure 2.4a. The variable r_{01} in this equation

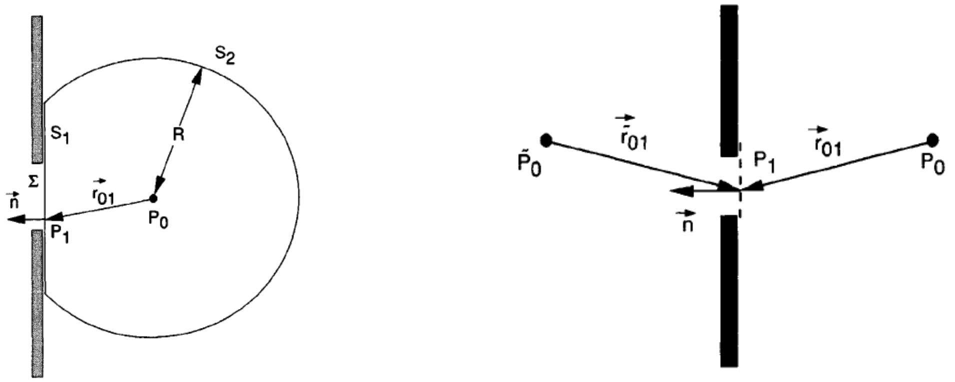

(a) Kirchhoff formulation of diffraction. Figure 3.6 from Goodman [19].

(b) Rayleigh-Sommerfeld formulation. Figure 3.8 from Goodman [19].

Figure 2.4: Comparison between Kirchhoff and Sommerfeld Boundary Conditions

refers to the distance from point 0 (the starting point of the wave) to point 1 (the aperture on the screen). Adding a second point source at P_2 led to the formulations of what is known as the Fresnel-Kirchhoff diffraction formula

$$U(P_0) = \int\int \frac{e^{jkr_{01}}}{jkr_{01}} \frac{1}{j\lambda} \left[\frac{Ae^{jkr_{21}}}{r_{21}} \right] * \left[\frac{\cos(\vec{n}, \overrightarrow{r_{01}}) - \cos(\vec{n}, \overrightarrow{r_{01}})}{2} \right] ds. \tag{2.6}$$

While this formulation has shown to yield accurate experimental results,the choice of boundary condition leads to some internal inconsistencies [19]. For a more exact solution, Sommerfeld realized that the single point source for the auxiliary equation could be replaced with 2 point sources(P_0 and $\tilde{P}_0$) which are mirror images of each other and either oscillating in phase or at a 180° phase difference as shown in Figure 2.4b. This resulted in a Green's function of

$$G^{+}(P_1) = \frac{e^{jkr_{01}}}{r_{01}} \pm \frac{e^{jk\tilde{r}_{01}}}{\tilde{r}_{01}} \tag{2.7}$$

and removed the requirement of a boundary condition of the aperture on the screen. The result of this formulation is known as the Rayleigh-Sommerfeld diffraction formula,

$$U(P_0) = \frac{-A}{jk} \int\int \frac{e^{jk(r_{21}+r_{01})}}{r_{21}r_{01}} \cos(\vec{n}, \overrightarrow{r_{21}}). \tag{2.8}$$

This solution can be applied to the propagation of a light source which is described by the Huygen's-Fresnel diffraction integral,

$$U(P_0) = \frac{1}{j\lambda} \int\int U(P_1) \frac{e^{jkr_{01}}}{r_{01}} ds. \tag{2.9}$$

In the case of inline holography, in which the light wave is propagating in a planar instead of spherical fashion, it makes sense to define this integral in a Cartesian coordinate system.

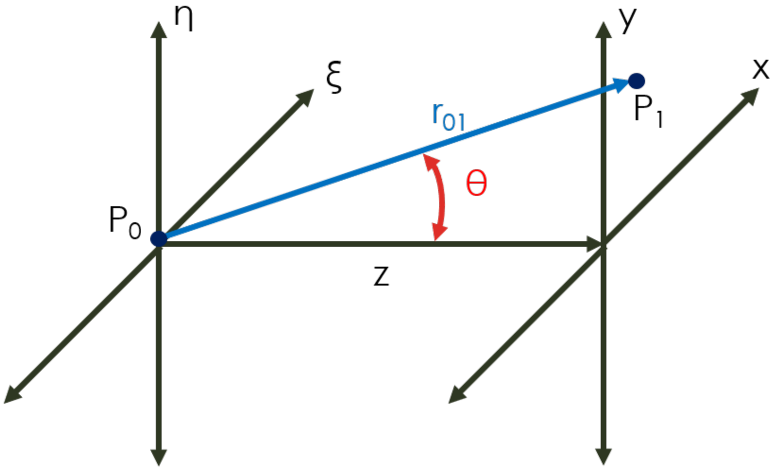

Figure 2.5: Cartesian coordinate system for defining the Huygens-Fresnel diffraction integral

Using the coordinate system shown in Figure 2.5, the Huygen's-Fresnel diffraction integral can be defined as

$$U(x,y) = \frac{z}{jk} \int\int U(\xi,\eta) \frac{e^{jkr_{01}}}{r_{01}} d\xi d\eta \tag{2.10}$$

where the distance between points (r_{01}) is defined exactly as,

$$r_{01} = \sqrt{z^2 + (x-\xi)^2 + (y-\eta)^2}. \tag{2.11}$$

2.1.2 Approximations

While the Fresnel-Huygen's diffraction integral (2.9) provides an exact model for light propagation, in order to determine the light intensity of a diffracted wave over an entire surface, the integral must be calculated for every point on the surface. Attempting to automate this process over a volume becomes time-consuming since the r_{01} value must be recalculated for every change in x, y, and z location. For this reason, there are two possible approximations of the Fresnel-Huygen's integral (2.9). The complete derivation of each approximation is provided by Goodman [19]. The first approximation, which involves a binomial expansion of the r_{01} term, is known as the Fresnel diffraction integral

$$U(x,y) = \frac{e^{jkz}}{jkz} \int\int U(\xi,\eta) e^{\frac{jk}{2z}\left[(x-\xi)^2+(y-\eta)^2\right]} d\xi d\eta \tag{2.12}$$

and is applicable in cases where

$$z^3 >> \frac{\pi}{4\lambda}\left[(x-\xi)^2+(y-\eta)^2\right]^2_{\max}. \tag{2.13}$$

A further approximation of this integral when

$$z >> \frac{k(\xi^2+\eta^2)_{\max}}{2}, \tag{2.14}$$

is known as the far field or Fraunhofer diffraction integral

$$U(x,y) = \frac{e^{jkz} e^{\frac{jk}{2z}(x^2+y^2)}}{jkz} \int\int U(\xi,\eta) e^{-j\frac{2\pi}{z\lambda}(x\xi+y\eta)} d\xi d\eta. \tag{2.15}$$

For use in dust particle locating and tracking, the requirements for the Fresnel diffraction integral are met, and therefore, equation (2.12) will be used to model light propagation.

2.1.3 Angular Spectrum Approach

A different approach to formulating a diffraction integral involves using a Fourier transform to create what is known as an angular spectrum. Similar to how a Fourier transform can be used to break down a signal into a collection of waves at different frequencies, it can also be used to break down a three-dimensional light wave into a collection of simple plane waves at multiple angles (known as the angular spectrum). The result of this approach is detailed by Goodman [19] and results in the following integral

$$A(\frac{\alpha}{\lambda},\frac{\beta}{\lambda},z) = \int\int U(x,y,z)e^{-2j\pi(\frac{\alpha}{\lambda}x+\frac{\beta}{\lambda}y)}dxdy \tag{2.16}$$

where the transfer function of the wave propagation is,

$$H(f_x,f_y) = \begin{cases} e^{2\pi j\frac{z}{\lambda}\sqrt{1-(\lambda f_x)^2-(\lambda f_y)^2}} & \sqrt{f_x^2+f_y^2} < \frac{1}{\lambda} \\ 0 & \sqrt{f_x^2+f_y^2} \geq \frac{1}{\lambda}. \end{cases} \tag{2.17}$$

Comparing this to the Rayleigh-Sommerfeld diffraction integral (2.8) it can be shown that they are the same equation [19]. Therefore, even though a different mathematical approach was used, once the Fresnel approximation is applied,

$$\sqrt{1-(\lambda f_x)^2-(\lambda f_x)^2} \approx 1 - \frac{(\lambda f_x)^2}{2} - \frac{(\lambda f_x)^2}{2} \tag{2.18}$$

the result can be transformed into the Fresnel diffraction integral (2.12) through a Fourier transform. The angular spectrum approach results in an angular representation of the Fresnel diffraction integral (2.12).

2.2 Reconstruction Methods

The creation of a hologram results from interference between a light wave that has been diffracted off an object, known as the object wave, and an unaltered reference wave. Figure 2.6 defines the location of each of the image planes and the coordinate systems that will be used to describe points on each plane. The hologram reconstruction process aims to separate the object wave phase and amplitude information encoded in the image. Reconstruction can be

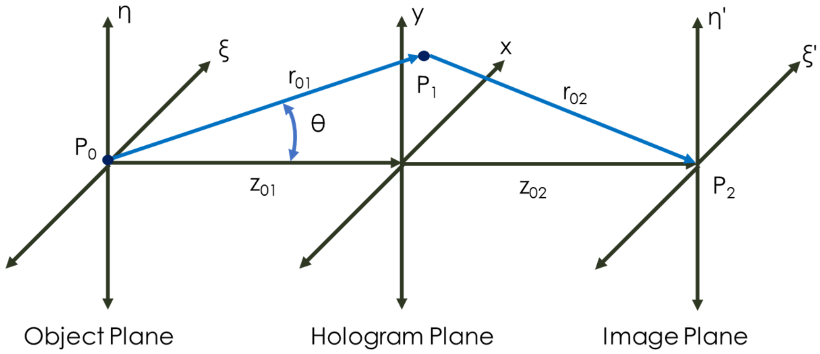

Figure 2.6: Coordinate system for reference in all reconstruction equations

accomplished by adding either the reference wave or its conjugate to the hologram image, resulting in the real image of the object wave appearing either at the object or image plane. Figure 2.7 shows the difference between using the reference wave or the conjugate reference wave and the location of the resulting images. From a mathematical standpoint, this combination of the reference wave and the hologram can be solved using the previously discussed Fresnel Integral (2.12) as defined using the coordinates in Figure 2.6,

$$\Gamma(\xi,\eta) = \frac{e^{jkz} e^{\frac{jk}{2z}(\xi^2+\eta^2)}}{jkz} \int\int U(x,y) e^{\frac{jk}{2z}(x^2+y^2)} e^{-j\frac{2\pi}{z\lambda}(x\xi+y\eta)} dxdy \\ U(x,y) = E_R^*(x,y)h(x,y). \tag{2.19}$$

In this equation, the function h(x,y) is the amplitude of the hologram image at point (x,y) and E_R^* is the amplitude of the reference wave. To find the object wave image at some distance from the hologram (z), this integral will need to be solved. There is no closed-form solution for this integral, but it can be solved using analytical methods. A short description and comparison of the three most common methods for finding this analytical solution, the Fresnel, convolution and, angular spectrum methods are now discussed.

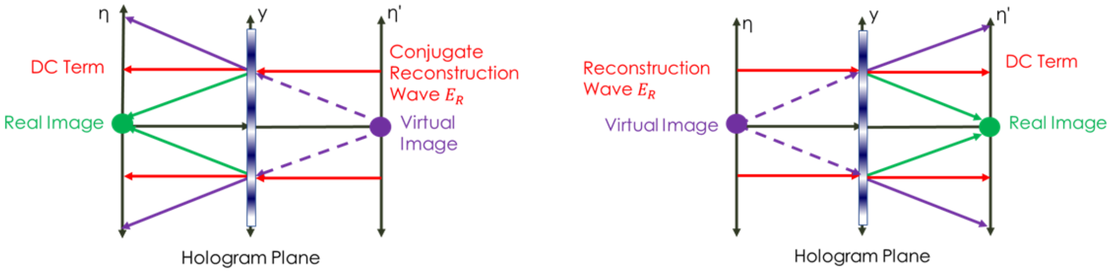

Figure 2.7: Use of reference wave or conjugate in hologram reconstruction

2.2.1 Fresnel

The Fresnel method seeks to rearrange the Fresnel integral (2.19) into the form of a 2D Fourier Transform which can then be solved using a fast Fourier transform (FFT). In order to accomplish this goal, the following substitutions are made,

$$\nu = \frac{\xi}{\lambda z}, \quad \mu = \frac{\eta}{\lambda z}, \quad \text{and} \quad \frac{jk}{2z} = \frac{\pi j}{\lambda z} \tag{2.20}$$

which leads to the following equation in the form of a Fourier transform.

$$\Gamma(\nu,\mu) = \frac{e^{jkz} e^{j\pi\lambda z(\nu^2+\mu^2)}}{jkz} \mathcal{F}^{-1}\{E_R^*(x,y)h(x,y)e^{\frac{\pi j}{\lambda z}(x^2+y^2)}\}. \tag{2.21}$$

Since the end goal is to perform this reconstruction on a digital image, this equation can be digitized making the following substitutions:

$$\begin{gathered} \nu = m\Delta\nu, \quad \mu = n\Delta\mu, \quad x = r\Delta, \quad y = s\Delta y, \\ \xi = \nu\lambda z = m\Delta\nu\lambda z, \quad \text{and} \quad \eta = \mu\lambda z = n\Delta\mu\lambda z \end{gathered} \tag{2.22}$$

resulting in the Discrete Fourier Transform,

$$\Gamma(m,n) = \frac{e^{jkz} e^{j\pi\lambda z\left(\frac{m^2}{N^2\Delta x^2}+\frac{n^2}{N^2\Delta y^2}\right)}}{jkz} \mathcal{F}\{U(r,s)e^{\frac{\pi j}{\lambda z}(r^2\Delta x^2+s^2\Delta y^2)}\} \tag{2.23}$$

which can be solved using a fast Fourier transform method in MATLAB or other signal processing software. The significant advantage of this method is that it only requires one FFT calculation which makes it a fast method. The main disadvantage of this method is that the pixel output size ξ is a function of distance from the hologram ($\Delta\xi = \frac{\lambda z}{N\Delta x}$). Therefore this method not useful for focusing on multiple particles at multiple distances since the pixel size will constantly be changing while scanning through the different distances. Therefore, while computationally quick, this method will not work for imaging particle fields.

2.2.2 Convolution

Instead of rearranging the Fresnel diffraction integral into the form of a Fourier transform, the integral can be rearranged into the form of a convolution

$$\Gamma(\xi,\eta) = \int\int h(x,y)E_R^*(x,y)g(\xi - x, \eta - y)dxdy, \tag{2.24}$$

where the convolution kernel is

$$g(x,y) = \frac{e^{jkz}}{jkz}e^{\frac{jk}{2z}(x^2+y^2)}. \tag{2.25}$$

For the discrete version, the kernel becomes,

$$g(x,y) = \frac{e^{jkz}}{jkz}e^{\frac{jk}{2z}(r^2\delta x^2+s^2\delta y^2)}. \tag{2.26}$$

This integral can then be solved using the FFT [2]

$$\Gamma(\xi,\eta) = \mathcal{F}^{-1}\left[\mathcal{F}(hE_R^*) * \mathcal{F}(g)\right]. \tag{2.27}$$

With this equation, the hologram can be reconstructed into the original image using the original z distance in the convolution kernel. In turn, by finding the in-focus image, the distance from camera to particle can be measured.

2.2.3 Angular Spectrum

For situations where the Fresnel approximation is not applicable the angular spectrum approach provides a method for solving the

Rayleigh-Sommerfeld diffraction integral through the use of equations 2.16 and 2.17. The situations where the Fresnel approximation (2.13) cannot be applied include situations where the relative size of the objects x and y dimensions are similar to or larger than z dimension, i.e., the object is fairly large or close to the camera. Since the particle tracking used here does not involve either of these situations the angular spectrum methods is not required.

2.3 Focusing Distance

One advantage of using holographic imaging is that the original location of an object in three-dimensional space can be determined from a two-dimensional image. In order to determine the depth location of the object, the hologram image must be reconstructed at a number of successive distances. The reconstruction distance where the object of interest is most in-focus is the z location of that object. Therefore, the key to correctly locating a particle in space is determining when the reconstructed image of the particle is most focused. There are many varied methods for qualitatively comparing the level of focus between images. Several of these methods, which have been successfully integrated with holography techniques (amplitude threshold, complex amplitude, and the hybrid method), are discussed in more detail.

2.3.1 Amplitude Threshold

When using the amplitude threshold method, the amplitude of the light for each frame is measured and averaged for an area near the particle. The distance for which the frame is in focus is where this amplitude is minimized, since this is the frame where the diffraction pattern collapses down to a solidly opaque object. The distance between the camera and the particle is the location of this frame.

2.3.2 Complex Amplitude

One of the limitations of the amplitude threshold method is that diffraction patterns, from other out-of-focus particles, can impact the amplitude of the particle of interest. For this reason, Pan and Meng [37] have suggested using the complex amplitude instead of the real amplitude of the light as a locating method. The theory behind this approach is that the in-focus image of a particle will consist only of the real object image and therefore contain no imaginary components. This method that Pan and Meng developed from this approach is known as particle extraction using complex amplitude (PECA).

2.3.3 Hybrid

Another method, known as the Hybrid method and developed by Guildenbecher et al., combines image intensity and edge sharpness to determine particle depth [21]. The hybrid method works by

> ″...apply[ing] various thresholds to the minimum intensity map to find a family of possible particle edges. Then, the values of the Tenengrad map from the pixels on the particle edge are averaged to estimate the edge sharpness of each possible particle edge. Finally, the particle edge with the maximum Tenengrad operator is chosen as the in-focus edge, and its depth is calculated from the average Z location along the selected edge of the Tenengrad depth map [21].″

The Tenengrad operator used here is a method of quantifying the sharpness of an image as defined by,

$$T(k,l,z_r) = [A_r(k,l,zr) \bigotimes S_x]^2 + [A_r(k,l,z_r) \bigotimes S_y]^2, \tag{2.28}$$

where S_x is the vertical and S_y the horizontal Sobel kernel. Based on Guildenbecher's analysis, this method is more accurate in determining the depth position of a particle than the PECA method. Experimental results show the uncertainty of particle location measurements using the hybrid method are 1.74

times the mean particle diameter [21] compared to an uncertainty of approximately 2.3 times the particle diameter in measurements from the PECA method [37].

2.4 Particle Location and Tracking Methods

While the above methods are useful in locating the depth of a single particle, to track and locate a large number of particles over time requires additional software algorithms. Pan and Meng [36] developed a holographic PIV system which used the complex amplitude focusing method [37] along with a Concise Cross Correlation (CCC) and particle pairing algorithm as developed by Pu and Meng [39]. Toloui has proposed using an inverse iterative particle extraction (IIPE) method, which relies on an inverse approach of comparing the actual hologram to a modeled hologram image and adjusting the model until it matches the actual hologram [48]. Mallary and Hong applied a fused lasso regularization algorithm to the inverse method and demonstrated an ability to process flows with concentrations of 0.035 particles/pixel compared to 0.0035 particles/pixel concentration resolved by Toloui [29]. The Hybrid method developed by Guildenbacher[21] and Gao [18] was implemented along with a nearest neighbor matching method to create the Sandia Particle Holography Processor (HoloSand) suite of MATLAB functions [20].

CHAPTER 3

DUST COMBUSTION CHARACTERIZATION

Dust combustion occurs when solid particles of combustible material are suspended in air and provided an energy source such as a spark or hot surface, leading to ignition and flame propagation throughout the dust cloud. In order to prevent dust explosions in processing facilities, it is critical to understand the conditions necessary for combustion of the dust present. Only then can a robust mitigation and safety plan can be developed. Since conditions vary based on the material composition and particle size of the dust, samples from the facility in question are collected and tested to characterize the explosibility of the material.

3.1 Characterization Methods

When characterizing the explosibility of a dust sample, there are two general areas of interest; the conditions under which combustion will occur and the severity of the resulting explosion. Some of the characteristics that describe the likelihood of combustion (i.e., ignition sensitivity) are the minimum explosible concentration (MEC), the minimum ignition energy (MIE), the limiting oxygen concentration (LOC), and the minimum autoignition temperature (MAIT). The characteristics which describe the resulting ignition severity of the explosion include the maximum explosion pressure (P_{max}), maximum rate of pressure rise($[dP/dt]_{max}$), and deflagration index (K_{st}) [24].

The general method for determining these characteristics consists of the following procedure. First, a dust sample is dispersed into a closed container and allowed to spatially distribute as a cloud before an ignition source is provided. Pressure sensors record the existence and/or severity of an explosion. One chamber commonly used for this testing is the Siwek 20-L chamber, shown in

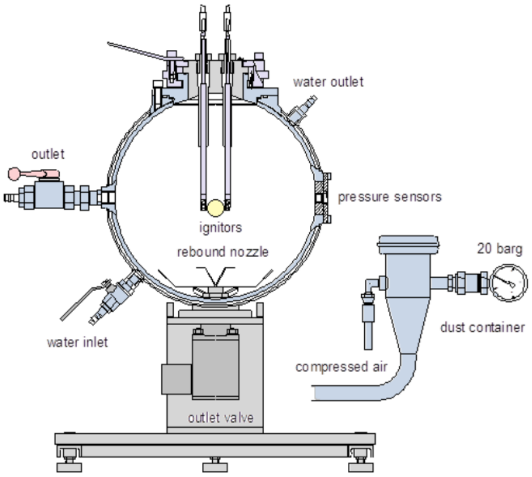

Figure 3.1: 20-L Siwek chamber diagram.
Image from Siwek chamber manual [8]

Figure 3.1. The dispersion of dust in this chamber is assumed to be relatively uniform as required by the ASTM standard E1515 [24]. The dust dispersion process begins by pulling a vacuum in the chamber of 0.4 bar absolute and pressurizing the dust in the dust container to 21 bar absolute [9]. Opening the outlet valve allows the pressurized air and dust in the dust container to flow through the nozzle and into the chamber until it reaches atmospheric pressure. After a short delay, the chemical igniters are initiated, and the pressure sensors record any pressure rise resulting from an explosion. The chamber is equipped with either the rebound nozzle or the perforated annular nozzle, both of which are shown in Figure 3.2.

3.2 Testing Concerns

The goal of dust combustion testing is to accurately quantify the likelihood and severity of dust combustion under certain environmental conditions. If testing cannot provide consistent results between different methods and devices

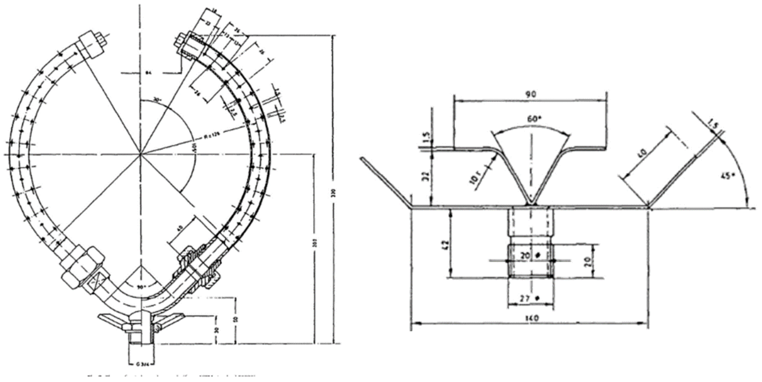

Figure 3.2: Rebound and perforated annular nozzle from ASTM standard E1226

and scale those results to match real world conditions, then the safety procedures designed to mitigate the risk of explosions may be ineffective, insufficient, or overly conservative. For example, the calculation of the explosion or deflagration severity index,

$$K_{st} = \left(\frac{dP}{dt}\right) V^{\frac{1}{3}} \tag{3.1}$$

relies on the assumption that the rate of pressure rise $\frac{dP}{dt}$ found in testing can be scaled for use in production equipment based on the cube root of the volume of the testing chamber V [9]. Unfortunately, some studies [32] [9] [3] have shown that the pressure rise is a direct result of the turbulence in the chamber and therefore does not always scale with volume. The main issues with replicating results between testing vessels and applying them to actual production equipment can be grouped into two general areas: the impact of the feeding process on the dust and the transient dynamics of the dust after dispersion.

3.2.1 Dust Feeding and Dispersion

When feeding dust particles into the chamber, not all particles will pass through the nozzle. Di Sarli et al. have identified this incomplete loading as one reason for a lower than nominal dust concentrations in the vessel, leading to misleading MEC values [13].

In addition to the concentration, another significant factor affecting the likelihood and severity of explosion for a specific dust is the size of the particles. The specific surface area available for mass transfer (A_v) is inversely related to the diameter of the individual particles (d_p) [35],

$$A_v = \frac{\pi d_p^2}{\frac{\pi}{6} d_p^3} = \frac{6}{d_p}. \tag{3.2}$$

As the diameter of a particle gets smaller, the ratio of surface area to volume increases. Since the surface area of the particle represents the amount of material available for oxidation through combustion, particles with a greater specific surface area release more energy during the combustion process. As a result, any explosibility characteristics for a dust are only valid for the particle size distribution used in testing. It is therefore essential that the particle size of the dust under evaluation matches that of the actual dust of concern.

Unfortunately, multiple studies have shown that the dispersion method used in the 20-L chamber results in significant particle breakage. When attempting to measure the uniformity of the dust distribution in the 20-L Siwek vessel using Pittsburgh Research Laboratory (PRL) optical dust probes, Kalejaiye et al. [24] found transmission data that was significantly lower than expected. Kalejaiye et al. hypothesized that the reason for this discrepancy was a change in particle size. This theory was confirmed by particle analysis which showed a 40%-80% reduction in the size of the dust before and after dispersion. This reduction in particle size was mainly attributed by Kalejaiye et al. to shearing action in the outlet valve, arguing that the contribution of the dispersion nozzle was minimal. Sanchirico et al. [42] further built on the results from Kalejaiye et al. [24] by comparing particle breakage to the elasticity of the material and demonstrating that materials with higher elasticity experience less particle breakage. This relationship between particle breakage and elasticity was also shown by Bagaria et al. [4] in a study which correlated particle breakage with the brittleness index of the material. An earlier study by Bagaria et al. [5] contradicted the conclusions of Kalejaiye et al. [24] concerning the output valve by demonstrating particle breakage using a 36-L vessel in which the particles did not pass through an output valve. These results suggest that significant particle breakage occurs as a result of particle collisions in both the dispersion nozzle and the turbulence of the dispersion cloud in addition to the output valve.

All of these studies agree that significant particle breakage occurs in the process of dispersing dust into the testing chamber. Additionally, the degree of particle breakage can be correlated to the elasticity or brittleness of the dust material. The discrepancy between these results is the extent to which each stage of the dispersion process: flow through the outlet valve, flow through the nozzle, and turbulence in the dispersion cloud contribute to the particle breakage.

Since all of these tests involve particle size measurements of the dust after dispersion, a method for demonstrating and measuring particle breakage at the nozzle and in the dust cloud as it occurs would help further the understanding of this mechanism. While further development is needed, recent work by Schweizer et al. [44] has demonstrated holography as a possible means of particle sizing and tracking in a dust dispersion chamber. A similar holographic method developed in this paper is used to build on the understanding of particle breakage in the dust dispersion process. The particle breakage results and analysis are presented in Chapter 7.

3.2.2 Turbulence and Homogeneity of Dust

Although this work is focused on particle sizing and not measuring turbulence or concentration in the dispersion chamber, the possibility exists of using digital in-line holographic particle image velocimetry (DIH-PIV) to measure turbulence with the combined dispersion and DIH imaging system developed here. Therefore, a short description of the significance of understanding the turbulence in the chamber and the current methods to measure and model these flows is presented here.

One of the main differences between dust and vapor combustion is that once a vapor is fully mixed with air, it will remain a homogeneous mixture with a fixed state [35], whereas the state of a dust cloud is always dynamic (i.e., the fixed state of a dust cloud would entail all the particles settling out of suspension and no longer existing as a cloud) [16]. The dynamic nature of dust clouds means that fully understanding and attempting to standardize the flow of dust in the testing chamber during dispersion and ignition is critical. Previous studies have shown that the turbulence patterns between the 20-L Siwek vessel and the 1 m^3 vessel are not the same at the time of ignition [9] [32]. Also, since the turbulence will decay once the initial flow of air has stopped, the K_{st} pressure rise is a direct result of the ignition time used. Therefore, the ignition time which results in the highest K_{st} [14] and lowest MEC [49] value is not consistent for all materials and accurate measurement of the K_{st} and MEC may require varying the ignition time.

Turbulence in the Siwek 20-L chamber has been experimentally characterized using light transmission [14], PRL optical probes [24], laser Doppler anemometers [9], and bi-directional velocity probes [32] [15]. Additionally, multiple CFD models of the turbulence have been developed by Di Benedetto et al. [11] and Di Sarli et al.[12], among others, to model these flow patterns.

CHAPTER 4

OPTICAL HOLOGRAM SYSTEM

4.1 Optical Components

As it relates to the rest of the holographic imaging system, the purpose of the optical subsystem was to create a beam large enough to reach every pixel on the image sensor without oversaturating any one pixel. Additionally, it was critical that all pixels received enough light from the laser to register an amplitude value distinguishable from noise.

The laser selected for this experimental setup was a 21 mW Helium-Neon (HeNe) Laser (Lumentum 1145P). The $1/e^2$ diameter of the beam from this laser is 0.7 mm, and the full angle beam divergence (θ_B) is 1.15 mrad [28]. These two properties are enough to fully describe the shape of the beam as it exits the laser. Assuming the beam to be Gaussian, the following set of equations can be used to model the shape and distribution of the beam as it passes through the optical setup and eventually reaches the camera sensor. A Gaussian shape for the beam is a reasonable model since the laser beam has $>$ 95% purity [28] to the TEM_{00} mode, which is the mathematical representation of a spherical Gaussian wave. As a Gaussian beam, the irradiance distribution at a radial distance r from the center of the beam at location z along the beam path is

$$I(r,z) = I_0 e^{\frac{-2r^2}{\omega(z)^2}} \tag{4.1}$$

where the peak irradiance I_0 is defined as

$$I_0 = \frac{2P}{\pi\omega(z)^2} \tag{4.2}$$

and P is the total power of the beam [45]. The $\frac{1}{e^2}$ diameter of the beam $(\omega(z))$ is a function of the distance (z) from the beam waist (ω_0) and the wavelength of the

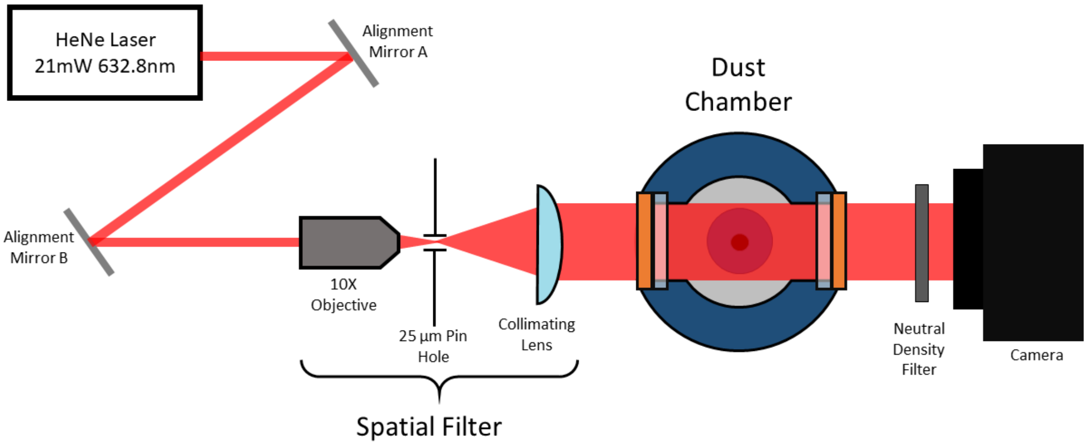

Figure 4.1: Schematic of beam path through holographic imaging system.

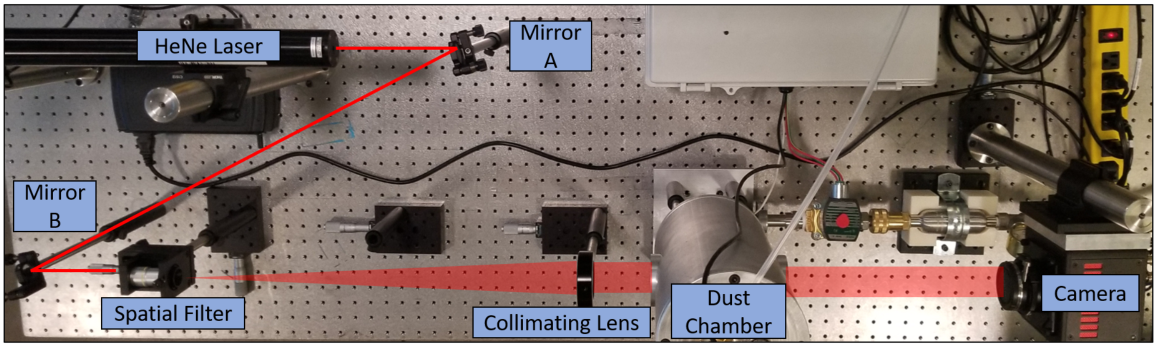

Figure 4.2: Picture of optical imaging setup with beam path added.

light (λ), [45]

$$\omega(z) = \omega_0 \sqrt{1 + \left(\frac{\lambda z}{\pi \omega_0^2}\right)^2}. \tag{4.3}$$

The beam waist, which occurs inside the laser itself, is a function of the laser beam divergence (θ_B) and wavelength of the laser light (λ)

$$\omega_0 = \frac{\lambda}{\pi \theta_B}. \tag{4.4}$$

Combining equations 4.1 - 4.4, the beam $\frac{1}{e^2}$ diameter will increase, and the peak irradiance will decrease as the beam moves away from the laser. The spreading of the beam will lead to a more even distribution of the amplitude of the laser which is beneficial for image capture with a digital camera.

Figure 4.1 shows the general path and size of the beam as it moves through the optical setup from the laser to the camera. This diagram is not to scale, but Figure 4.2 shows the locations each of theses components when placed on the optical table. A red line was added to this image to show the relative location and size of the beam since the beam is not visible to the naked eye or in photographs when passing through space.

Mirrors A and B, shown in Figures 4.1 and 4.2, were used for adjusting the alignment of the laser beam as it moved through the rest of the optical setup. It can be assumed that they only impact the direction of the beam and do not change the shape or divergence.

After reflecting off the mirrors, the beam passes through a spatial filter, shown in Figures 4.1 and 4.2, which removes noise from the beam, resulting in a more Gaussian distribution. The spatial filter works by focusing the beam down to a small waist and passing it through a pinhole. At this focused spot, the higher spatial frequencies caused by noise in the signal will appear at the edge of the beam distribution curve and will be filtered out by the edges of the pinhole, as shown in Figure 4.3.

Once the beam exits the pinhole, it will continue to diverge at the same angle at which it entered the pinhole. The pinhole was sized based on the supplier recommendation that the pinhole be 30% larger than the diffraction-limited spot size at the 99% contour, which is given by

$$D_{pin} = \frac{\lambda f_1}{r_1}, [47] \tag{4.5}$$

where f_1 if the focal length of the focusing objective and r_1 is the radius of the incoming beam. Based on this calculation, a 25 μm pinhole (D_{pin}) was selected for use inside the spatial filter.

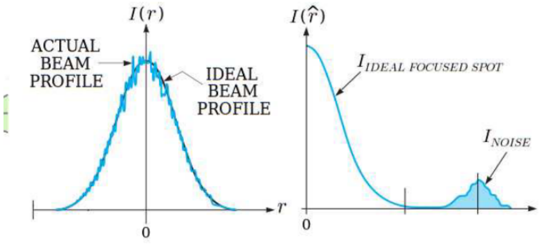

Figure 4.3: Movement of high-frequency noise components to the edge of the focused beam. Image from Abrantes [1]

Figure 4.1 shows that the diverging beam can be collimated, by placing a lens after the spatial filter. In order to collimate the beam, this lens must be placed so that the focal point is located directly at the beam waist as it passes through the pinhole. In order to fully cover the camera sensor, the beam waist size needed to be greater than the diagonal size of the sensor 28.96 mm. For the rough design of the location and focal length of the two lenses in the spatial filter, the geometric beam tracing shown in Figure 4.4 was used. In order for this setup to fit into the spatial filter mount (Edmund Optics #39-976), a 10x objective with a focal length of 17.02 mm and a working distance of 4.4 mm (Edmund Optics #33-437) and a collimating lens with a focal length of 500 mm (Edmund Optics #69-464) were selected. From this geometric method, the waist radius of the output beam was estimated from the following relationship

$$\frac{r_1}{f_1} = \frac{r_2}{r_1} \tag{4.6}$$

to be 20.54 mm, which is sufficient to cover the entire camera sensor with some extra overhang to account for the assumptions used in this method.

For a more precise calculation of the beam propagation through the spatial filter, which takes into account Gaussian propagation, the following equations

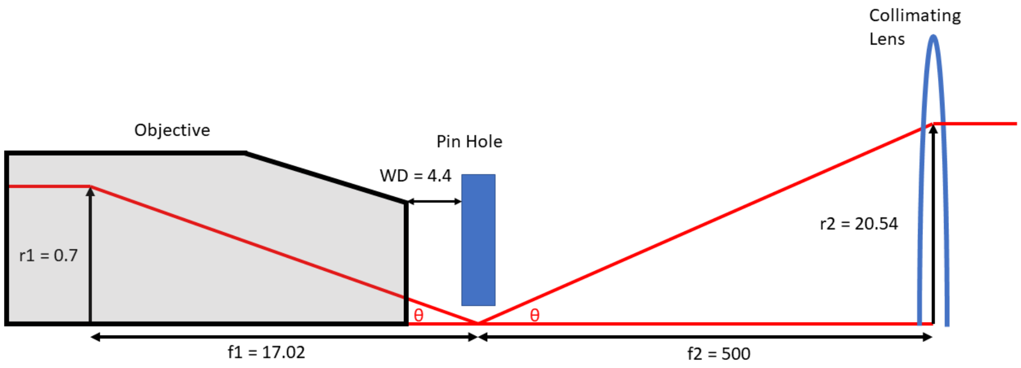

Figure 4.4: Geometric relationship between lenses in the spatial filter

developed by Self [45]

$$s' = f + \frac{s - f}{\left[\frac{s}{f} - 1\right]^2 + \left(\frac{z_R}{f}\right)^2} \tag{4.7}$$

$$\omega_0' = \frac{\omega_0}{\sqrt{\left[1 - \frac{s}{f}\right]^2 + \left(\frac{z_R}{f}\right)^2}} \tag{4.8}$$

can be used to find the location s' and radius ω_0' of the beam waist after each focusing component (objective and lens). This beam waist after each component is a function of the location s and radius ω_0 of the beam waist prior to the component along with the focal length of the element f and Rayleigh range of the beam z_R.

In some cases an absorptive neutral density filter with an optical density (OD) of 1.0 was added in front of the camera to prevent over-saturation. Based on the definition of optical density,

$$OD = \log_{10} \frac{1}{T} \tag{4.9}$$

the percentage transmission of light (T) from the beam into the camera, for an optical density of 1.0 is 10%.

Knowing the laser beam distribution as it reaches the camera, the output value of each pixel can be calculated to determine the amount of saturation. The frequency of photons contacting a given pixel f_γ can be calculated from the intensity distribution I by diving power by the energy of a single photon,

$$f_\gamma = \frac{I\lambda}{hc} \tag{4.10}$$

where h is Plank's constant and c is the speed of light [22]. Then, the number of electrons created by this pixel E_p can be determined by incorporating the fill factor FF (the amount of the pixel area that can capture photons), the quantum efficiency QE (the number of electrons output per photon revived), and the shutter time t_s (the amount of time the pixel is open to receive photons) [22]

$$E_p = QE * FF * t_s. \tag{4.11}$$

Finally, the output voltage of each pixel V_p is a result of the percentage of the well capacity W_{cap} that is filled by the electrons created E_p represented as an 8-bit number [22].

$$V_p = \frac{E_p}{W_{cap}} * 255. \tag{4.12}$$

For this holographic setup the camera used was a Fastcam Mini AX200 with the following properties: $QE = 49\%$, $FF = 58\%$, $W_{cap} = 16,000[\mathrm{e}^-]$ [38].

Using a combination of equations 4.1-4.9, the size and shape of the laser beam can be calculated at any point along its path. A model of the beam size throughout the optical setup and the beam distribution shape at specific points is shown in Figure 4.5. Using equations 4.10-4.12, the output of each pixel on the camera can also be modeled to confirm that the unobstructed beam is not over-saturating the sensor.

In order to confirm this model for the holographic setup, an image of the beam was captured using the camera set to the fastest shutter speed of 260 ns.

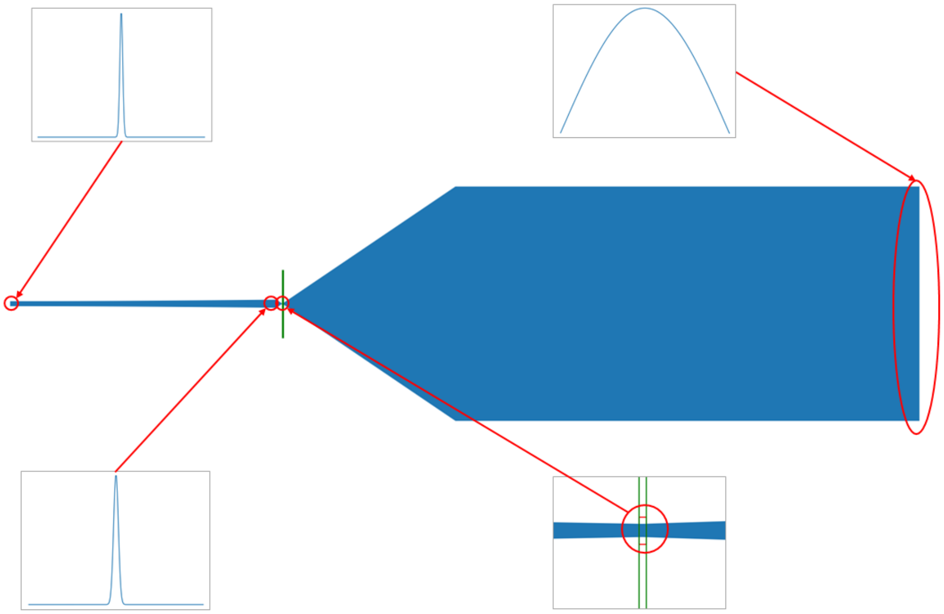

Figure 4.5: Beam waist size and irradiance distribution throughout the optical setup

The comparison of the light distribution between the models and the actual setup is shown in Figure 4.6 along the X and Y-axis through the peak of the Gaussian curve. If the beam size or power needs to be adjusted to capture a different volume of dust, this model allows quick calculations of which optical components need to be changed and the impact those changes will have on the light captured by the camera.

4.2 Setup and Calibration

Before beginning any data capture using the holographic optical system, it is essential that the optical components are correctly located, and the system is calibrated. First, the laser must be plugged into the power supply (Edmund Optics #11-391) and allowed to run for at least 20 minutes before collecting any images. After 20 minutes, the laser will have reached at least 95% power and will be adequately stable [28]. The laser and camera height should be set so that the

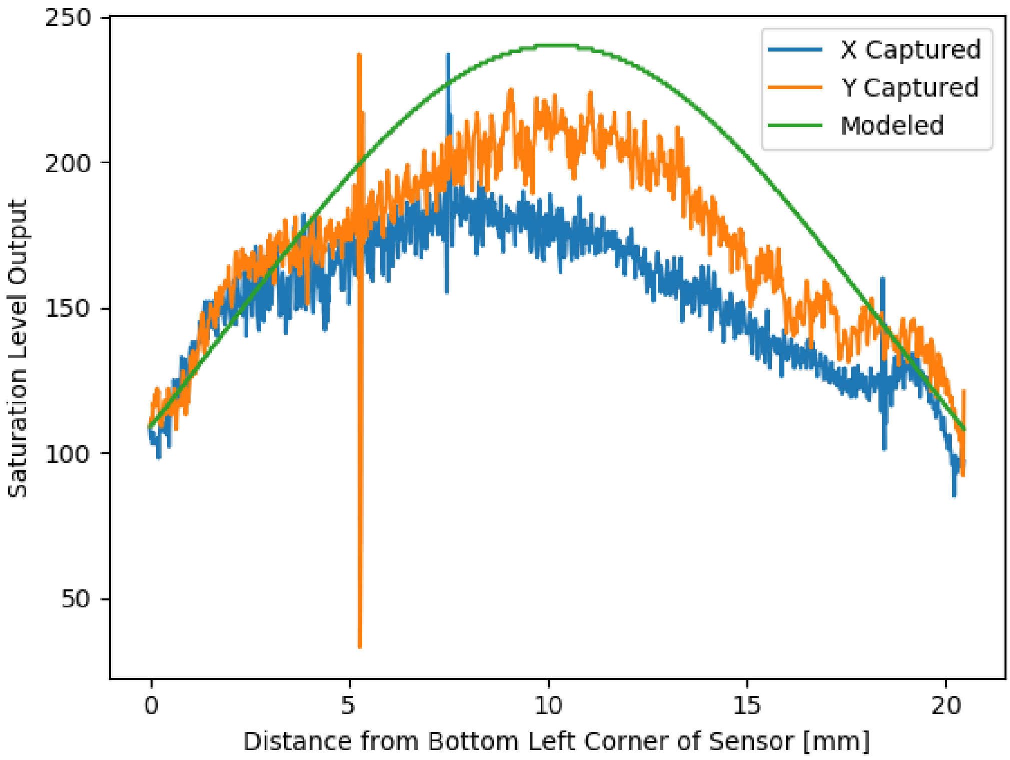

Figure 4.6: Comparison of modeled and recorded light intensity.

center of the beam and the center of the camera chip align with the windows on the dispersion chamber. Throughout the process of setting up the optical components, it is useful to check the height and rough size of the beam diameter at different locations on the table, which can be quickly accomplished using a magnetic alignment screen (Thorlabs #TPSM2/M).

Once the beam is set at the correct height, the spatial filter can be placed on the table, aligned, and calibrated, resulting in a clean beam coming out at the correct location. The general process of setting up the spatial filter involves lining up the optical mounts with the beam; installing and aligning the objective; installing and aligning the pinhole; and moving the objective towards the pinhole until the output beam switches from an Airy pattern to a single solid circle. Although written for a different model than the one used in this setup, the

Thorlabs manual for the KT310 spatial filter [46] provides a clear step-by-step description of how to align the filter assembly.

After the spatial filter is set up, the collimating lens should be installed on a translational stage at a distance from the pinhole located at approximately the focal distance of the collimating lens. The collimating lens used with a magnification lens on the camera has a focal length of 200 mm, while the collimating lens used with just the camera has a focal length of 500 mm.

The neutral density filter can be installed between the collimating lens and the camera. A neutral density filter is only necessary if the beam image is over-saturated by the laser beam and is therefore not required in all setups. Finally, the cover on the camera can be removed, and an image of the beam should appear in the camera viewing software.

4.2.1 Calibrating the Collimating Lens

When placing the collimating lens into the optical setup, it must be located near its focal length of the lens in order to collimate the beam. The alignment screen can be used to check that the size of the beam is relatively consistent from the lens to the camera, but is it not possible to determine the degree of beam divergence with just the naked eye. The particle sizes being relatively small compared with their distance from the camera, slight convergence or divergence of the beam can lead to significant differences when determining the focusing distance. Therefore, instead of relying just on visual confirmation, the collimation of the beam is checked and the focal distance calibrated through holographic reconstruction of a known object at measured distances.

The object, in this case, is either the USAF 1951 target [17] or a collection of dust particles on a sheet of glass (Chapter 5). The object is placed at two separate distances from the camera, and the hologram reconstruction method is used to determine the relative distance of each image from the camera. The difference between the holographically calculated distance and the amount the target was moved is used to adjust the location of the collimating lens until the two values match. A detailed description follows.

The USAF target is placed in a two-axis optical mount with an in-plane range of 50 mm x 30 mm and a resolution of 100 µm (Thorlabs #XYF1). This mount is attached to a single axis translational stage with a travel range of 25 mm and a resolution of 10 µm (Thorlabs #PT1/M). The two-axis mount is used to locate the target in the middle of the collimated laser beam so that the highest resolution lines are centered at the highest intensity part of the beam. The mount is then installed on a translational stage centered where the middle of the dispersion chamber will be located.

Starting with the translational stage micrometer set at 0 mm and the target centered in the middle of the beam, a hologram is recorded and focused using the ResAnalysis software (Section 5.3) to find the focused distance z. The translational stage is then used to move the target until the micrometer reads 25 mm and another hologram is captured and analyzed to find the z location. The difference between these two hologram-focused locations should be 25000 microns. If the distance is too great, then the collimating lens is moved towards the camera, and if it is too small, the lens is moved away from the camera. This process is repeated until the lens is within 100 microns of the correct distance.

The data collected in collimating the 500 mm lens is presented in Figure 4.7. The Y-axis on this chart is the distance calculated from the hologram analysis, and the X-axis is the relative location of the collimating lens translational stage for that pair of holograms. The numbers next to each data point represent the order in which the holograms were recorded. Each iteration of the process is attempting to move the output distance closer to the actual distance of 25,000 microns, which

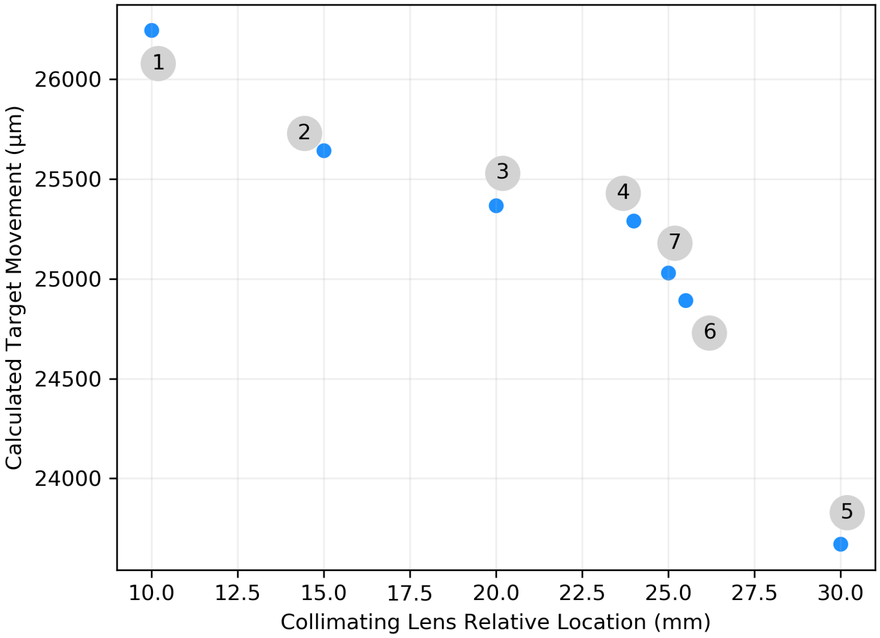

Figure 4.7: Example calibration of collimating lens

is achieved on the seventh iteration when the lens is located at 25 mm on the translational stage micrometer and the output distance measurement is 25,031 micrometers, within 0.031 mm of the measured distance. The final location of the transitional stage should be recorded for re-adjusting the lens in case it is accidentally moved. This collimating process only needs to be repeated if the collimating lens or any optical components upstream are changed. It does not need to be performed for each setup, although one iteration of the process can confirm results if a new method or software program is being used.

Since the focal distance of the two collimating lenses differs by 300 mm, each lens was collimated separately using a separate translational stage. By leaving the two stages set up with the post holders installed, switching between lenses does not require a full re-calibration, only a single check. The calibration of lens location can be performed with or without a lens on the camera since both

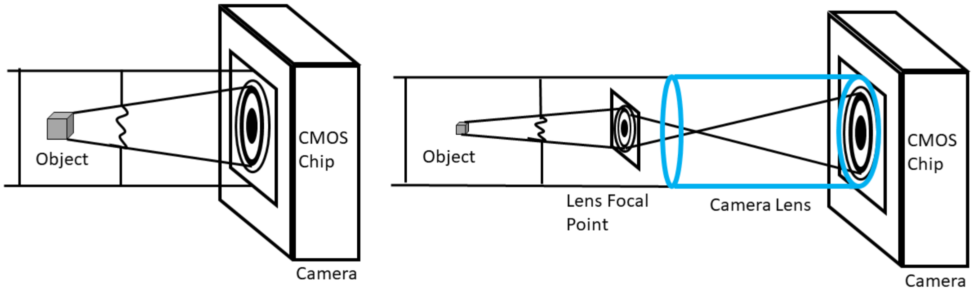

Figure 4.8: Hologram image with and without a camera lens

cases require a collimated beam. For the 200 mm collimating lens, the collimation process was first performed without the camera lens to limit variables affecting the z location to only the collimation of the beam. Once the collimating lens was correctly located, the camera lens was added, and the magnification of the system was calibrated.

4.2.2 Camera Lens Magnification

An Infinity Infiniprobe TS-160 lens was used with the camera to magnify the images. Magnification of the hologram images is critical for smaller particle sizes where the size of the particles without any magnification is similar to the size of the pixels. As detailed in Section 2.2.2, the convolution reconstruction method results in an image with pixel sizes spaced at the same distance on the camera as the object. Therefore, when trying to size particles without magnification, the smallest differentiation available with this camera is 20 µm. Since the dust particles being sized in these tests are on the magnitude of 20-200 µm, this gradation is too coarse. By adding a magnifying lens into the system, the relative size of each pixel can be reduced to give more definition to the image and measurements. The trade-off of increased magnification is that since the number of pixels is not increasing, the overall field of view of the camera will shrink. In

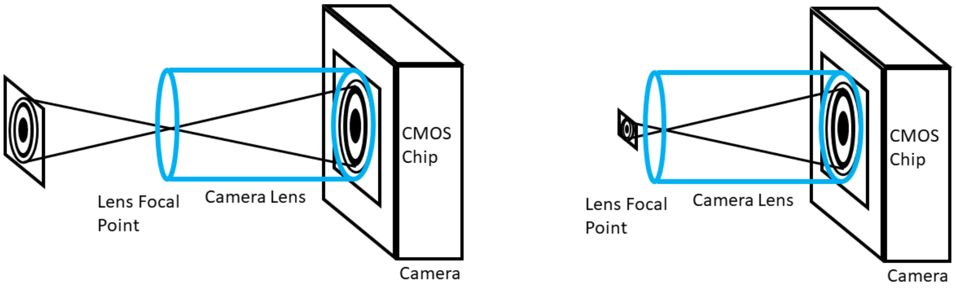

Figure 4.9: Camera lens magnification and focal distance relationship

other words, the magnification selected should balance the precision required of the diameter measurement with the number of particles visible in a single frame. Based on the size of the lycopodium dust, a magnification of approximately 4.5x was selected.

To set the magnification of the camera lens, the focus of the lens is adjusted to move the lens focal point. Figure 4.8 shows how this focal point serves as a type of intermediate image location between the camera and the object. The image at the focal point would appear if one were to place a screen at this location. The image that appears on the camera is just a magnified version of this focal point image. By moving the focal point, the magnification of the hologram image changes. As Figure 4.9 demonstrates the closer the lens focal point is to the camera, the greater the magnification of the image.

To determine the magnification of the lens, the location of the focal point must first be determined. The focal point can be located by taking a known object image, back-lit by the laser, and moving it closer to the camera until the image comes into focus. When the image comes into focus, the current location of the object is at the focal point of the camera lens. By taking an image at this point and comparing the pixel size of the image to the actual size of the object, the magnification factor can be determined. The previously discussed USAF 1951

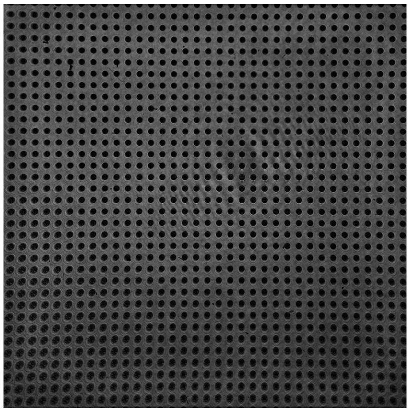

Figure 4.10: Dot chart used for estimating lens magnification factor

Target can be used for this calculation, but using a dot chart will give a more precise measurement. The image of a dot chart shown in Figure 4.10 was captured to determine the magnification of this setup. Since the target manufacturer precisely reports the dot spacing, the spacing present in this image can be compared to the reported spacing to determine the amount of magnification. If there is insufficient magnification, the focus adjustment knob is used to move the focal point closer to the camera or away from the camera if the magnification is too great. Any adjustment in the focus will bring the image out of focus, so the target will need to be moved in the necessary direction until it is back at the focal point. The process is then repeated until the desired magnification is set. At this point, the set screw in the focus adjustment knob should be tightened so that the magnification is not accidentally changed.

While this method is useful in getting a good approximation of the magnification, there is still a fair amount of uncertainty in how the distance between objects on the target are measured. Therefore, the magnification as determined by this method is not sufficiently accurate. This inaccuracy in the magnification value appeared when performing the resolution analysis with the camera lens (Section 5.4.1). The initial results showed that software calculated distances were much larger than the actual distance. Since the collimating lens had already been calibrated to show agreement between these values, the only variable that changed with the addition of the camera lens was the magnification factor used in processing the data. With a slight adjustment in the magnification factor from 4.56x to 4.63x, the two methods of measuring distance came into agreement. As a result, a calibration method similar to the one used for the collimated lens in Section 4.2.1 should be used to find the actual magnification of the camera lens. Since the magnification determines the relative pixel size used in the reconstruction equations, it directly impacts the refocusing distance and is critical for getting accurate distance measurements.

CHAPTER 5

RESOLUTION ANALYSIS

When describing the ability of an optical system to create an image of an object, the two main parameters of interest are resolution and contrast. For a standard two-dimensional image, the resolution is the ability of the system to distinguish between object details. Figures 5.1a and 5.1b show the difference between an optical system that is able to resolve a set of black lines and one that is not. The contrast of an optical system is the extent to which the original maximum and minimum amplitude of the object are reproduced in the final image. In Figure 5.1c, as the square wave travels through the optical system, the discontinuities are rounded off into a sine wave. When this wave reaches the camera sensor, each pixel serves to integrate the area above or below the curve. The result is a loss of contrast, meaning that the maximum and minimum values read by the pixel are less than in Figure 5.1a, i.e., the black and white regions of the image have become greyer. If the decrease in contrast is significant enough, it can result in an inability to distinguish between two pixels. Therefore, while two distinct phenomena affect the ability to distinguish between objects in an image, sensor resolution and optical contrast; for this study, the term resolution will not differentiate between the two but only describe the general ability of the imaging system to distinguish individual objects.

When determining the resolution of a hologram, in addition to the standard in-plane image resolution, the imaging system can also be characterized by its ability to discern the depth of an object. The precision of this axial or depth resolution is limited by the spacing between reconstruction frames (Δz), as shown in Figure 5.2. Since the depth measurement relies on information collected from the pixels, the accuracy of this measurement is also correlated to the in-frame

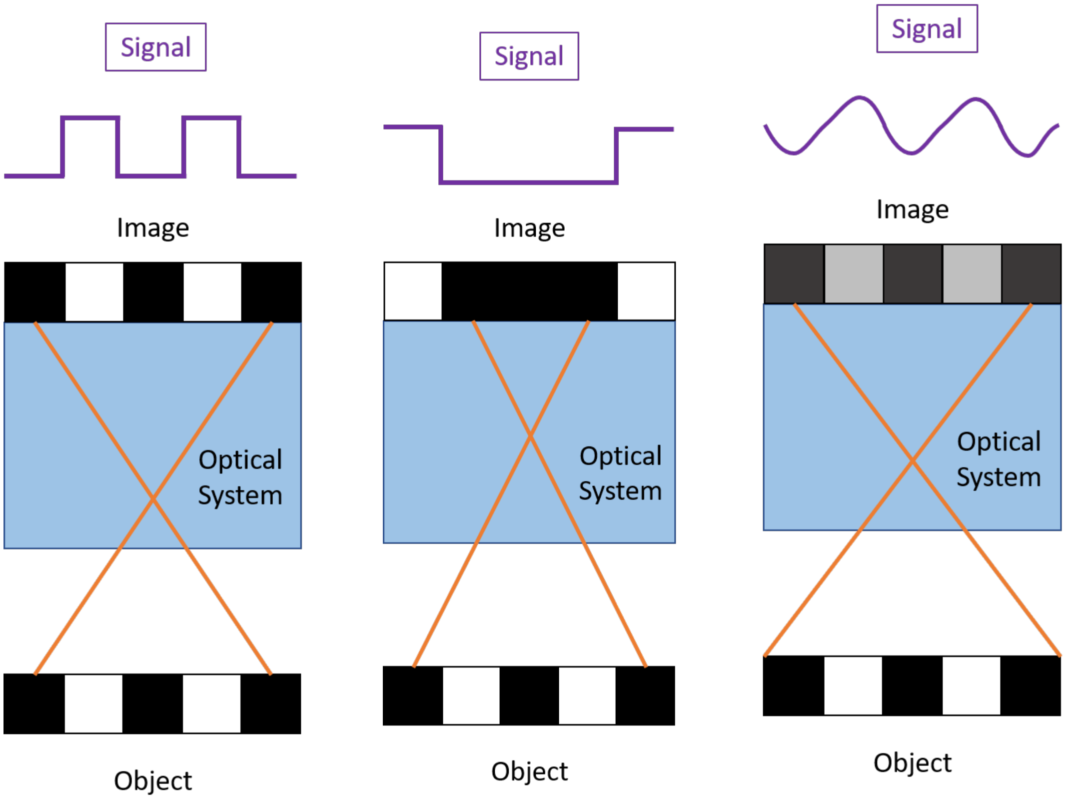

(a) Resolved image

(b) Unresolved image

(c) Reduced contrast resolved image

Figure 5.1: Demonstration of the resolution and contrast of an optical system

resolution in addition to the ability of the focusing method (Section 2.3) to delineate the in-focus frame at the correct distance. Noise from non-focused particles, misalignment of optical components, and nonuniformity in the beam can also introduce error into this measurement. As discussed in Section 2.3.3, the axial location measurement is accurate within 2.3 particle diameters for the PECA method and 1.74 particle diameters for the hybrid method. While these proportionalities serve as a good starting point for estimating the resolution of the system, the accuracy and precision of size and three-dimensional location are specific to the optical components and camera used. Thus, to allow for an accurate evaluation of the results, it is necessary to experimentally benchmark the

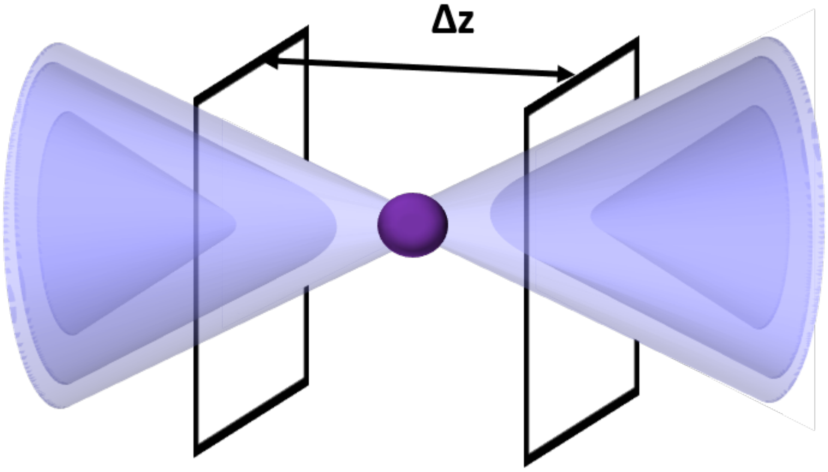

Figure 5.2: Spacing of reconstruction frames relation to axial precision

resolution limits for this setup before taking any measurements.

A summary of the resolution studies that were conducted is presented below. The theoretical background for evaluating holographic imaging resolution is introduced, followed by a description of the computational tools used for analyzing the results. The experimental method and results are presented for the USAF target and then the dust samples of sugar and lycopodium, before a final summary and discussion of the results concludes the chapter.

5.1 Summary of Resolution Studies

Table 5.1 summarizes the different resolution studies that were performed along with the section in which they are presented. The USAF target was used to determine the in-plane image resolution. In order to quantify the in-plane resolution for comparison between studies, the mean resolution and the standard deviation are calculated for each data set. For the in-plane resolution, measurements were taken with and without the magnifying lens for comparison. The in-plane image resolution focused with a magnification of 4.52x was omitted since the depth results showed the magnification value used in the calculations to

Table 5.1: Summary of resolution studies and results

Resolution Study			Resolution	
Section	Object	Magnification	In-Plane Image	Axial Depth
5.4.3	USAF Target	1	X	X
5.4.3	USAF Target	4.52	–	X
5.4.4	USAF Target	4.63	X	X
5.5.1	Sugar	1	–	X
5.5.2	Lycopodium	1	–	X
5.5.3	Lycopodium	4.63	–	X

be incorrect.

For the axial resolution, the average error and the residual standard error (RSE) were calculated for each study. The average error indicates whether the error values for that set are skewed in one direction. It is important to note that since the error can be positive or negative, this value does not denote the amount of error, e.g., a set with a large amount of error could have an average of zero if the error values are evenly distributed on either side. To quantify the amount of error, the RSE was calculated using [23],

$$RSE = \sqrt{\frac{1}{n-2}\sum_{i=1}^{n}(y_i - \hat{y}_i)^2}, \tag{5.1}$$

where n is the number of data points, y_i is the DIH measured location, and $\hat{y}_i$ is the actual target location (as measured by the micrometer) relative to the initial location. The axial depth location was calculated for the USAF target, sugar, and lycopodium without a lens and the USAF target and lycopodium with a lens.

5.2 Theory

Thomas Kreis has provided a detailed mathematical frequency analysis of the Fresnel [26] and convolution reconstruction methods [27], which can be used for a more rigorous understanding of the effect these methods have on the output

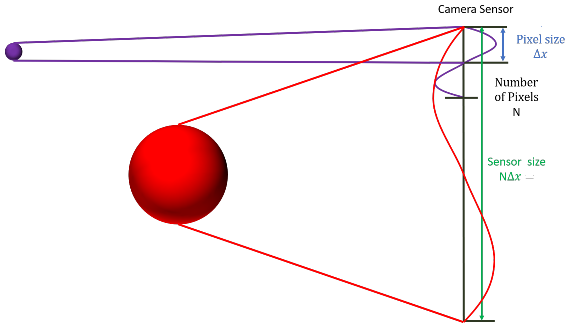

Figure 5.3: Relationship between object size, object distance, sensor size, and signal frequency

resolution of hologram systems. In its relation to holography, the spatial frequency of the output image results from the angle between the two interfering waves. Smaller objects and shorter distances will create the highest frequency patterns. The ability to reproduce an image is limited by the bandwidth of frequencies that the camera can record. The highest frequency is limited by the Nyquist frequency of the pixel pitch. In other words, any interference pattern with a spatial frequency (h_f) greater than half of the pixel frequency (f_p) (which is the inverse of the pixel pitch (pix_p)),

$$f_h \leq \frac{1}{2} f_p \quad \text{or} \quad f_h \leq \frac{1}{2pix_p} \tag{5.2}$$

will be aliased, and not able to contribute to the hologram reconstruction. On the other end, the overall size of the camera sensor will limit the lowest spatial frequencies. Since the diameters of the particles being imaged are small relative to the overall sensor size, the main concern is the high-frequency patterns. These frequency limits and how they relate to the size of the particle and sensor is shown in Figure 5.3.

While understanding the effect of the camera sensor on the image resolution can help assess the expected output resolution, once a camera is selected for the setup, those limits are set. As far as further improvements that can be made from the computational side, Kreis notes that in hologram reconstruction, it is the transfer function that limits the frequencies of the output based on the distance. He further suggests that by breaking up the reconstruction process into multiple reconstructions, each having a shorter reconstruction distance, higher frequencies can be reproduced, increasing the resolution of the output image. The obvious trade-off here is that the processing time increases with each reconstruction, so the total number of reconstructions is limited. This process, known as cascaded free space propagation (CFSP), is implemented as an option in the HoloPy program. For the resolution studies, initial testing of the CFSP method results indicated that the computational time was reasonable up to 5 CFSPs but improvements in image quality significantly decreased after 3 CFSPs. Therefore 3 CFSPs were used in reconstructing the images for all resolution analysis studies.

Another conclusion from Kreis's analysis was that as the fill factor of the camera decreases, at high frequencies, the contrast between light and dark will also decrease. This relationship is significant since the camera used in this system has a fill factor of only 48%, meaning that the contrast of the output image is less than a camera with 100% fill factor. This lack of contrast will make it more difficult to accurately detect particle edges and use sharpness as a focusing method, possibly effecting the resolution limits.

5.3 Software Tools

HoloPy is an open-source python-based software package developed by the Manoharan Lab at Harvard University to work with digital holograms [6]. HoloPy functions were used in these resolution studies to pre-process hologram images and reconstruct the image volume through backpropagation. These are only a small set of the many capabilities of HoloPy, which are further defined in the software documentation [30]. The advantage of using HoloPy is that the extensive documentation and simplicity of the code allows for implementation into customized programs based on the type of analysis required.

To analyze the image and axial resolution of this holographic imaging system, python code ResAnalysis was developed. This program uses functions of the HoloPy [30] and OpenCV [7] libraries for image processing, including dead pixels removal and background subtraction, the HoloPy propagation function for reconstructing the hologram volume, and an algorithm based on the PECA method (Section 2.3.2 developed by Pan and Meng [37]) for finding the in-focus frame and location.

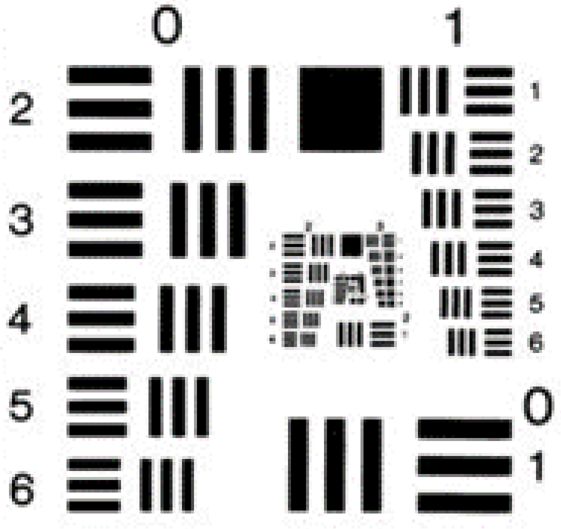

Figure 5.4: USAF 1951 resolution target. Image from Military Standard MIL-STD-150A [17]

5.4 USAF Target Resolution

5.4.1 Method

A 1951 USAF positive test target (MIL-STD-150A [17]) was used as the imaged object for measuring the resolution of this hologram system. When creating a reconstructed image of this target from the hologram, the smallest set of lines that appear as three distinct lines in the final image, determine the resolution of that image. The USAF chart labels each set of line sizes by a group and element number. In Figure 5.4, group 0, element 1 consists of the set of lines at the bottom right, group 0 elements 2-6 are on the left-hand side, and group 1 elements 1-6 are on the top right. The resolution of the image is determined from these group (g) and element (el) numbers and can be reported either as the thickness of the line pair (in meters) or as the number of line pairs per mm (lpmm),

$$Resolution = \frac{\frac{32000}{2^{(6+g)}}}{2^{\frac{1}{6}(el-1)}} \text{ [m]} \tag{5.3}$$

or

$$Resolution = 2\left(g + \frac{e-1}{6}\right) \text{ [lpmm]} \tag{5.4}$$

The ResAnalysis program does not have any automated particle locating method, so the pixel numbers surrounding the particle of interest must be manually entered. For the USAF target, the particle of focus was the group of pixels which contained element 4-1. This section was selected because it is a relatively small area where the individual lines remained distinct enough to find when the image was unfocused. A hologram image of the USAF target captured for the resolution analysis is shown in Figure 5.5a. In order to find the focused location for this image, the pixel numbers surrounding element 4-1 (Figure 5.5c) must be entered into the ResAnalysis code. The software is then able to locate the

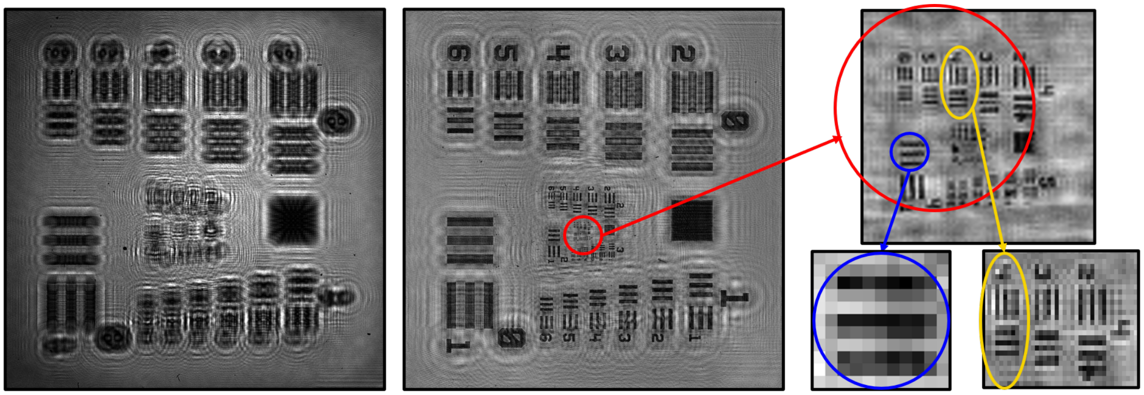

a) Hologram Image b) Focused Image c) Focusing Point d) Resolution (4-4)

Figure 5.5: USAF 1951 target hologram focusing method

in-focus image (Figure 5.5b). Based this focused image the smallest distinguishable line set is element 4-4 (Figure 5.5d), meaning that from equation 5.3 the resolution is 23 [µm].

Similar to the method used in calibrating the collimating lens in Section 4.2.1, the USAF target was used as the object and processed using the ResAnalysis program. The target was initially placed on the table close to where the center of the dispersion chamber would be located. Images were taken at 10 locations in each direction 0.5 mm apart. For each processed hologram image, the in-plane image resolution was recorded along with the z location of the reconstructed image. This reconstructed distance was then compared to the actual distance the target had been moved to determine the axial resolution of the image. This process was repeated with the inclusion of the lens on the camera.

5.4.2 USAF Target Resolution Without Magnification

The resolution data collected for the USAF target without a camera lens is presented in Table 5.2. The smallest resolvable set of lines for all the images were between 18 µm and 25 µm with an average resolution of 20.31 µm and a standard deviation of 1.88 µm. Considering that the pixels are 20 µm x 20 µm, this is a

Table 5.2: USAF 1951 target in-plane resolution based on location

Image Number	Distance	Chart		Resolution	
		Group	Element	µm	lp/mm
1	-5	4	4	22	23
2	-4.5	4	5	20	25
3	-4	4	6	18	29
4	-3.5	4	5	20	25
5	-3	4	5	20	25
6	-2.5	4	5	20	25
7	-2	4	5	20	25
8	-1.5	4	6	18	29
9	-1	4	5	20	25
10	-0.5	4	5	20	25
11	0	4	5	20	25
12	0.5	4	5	20	25
13	1	4	4	22	23
15	1.5	4	5	20	25
16	2	4	5	20	25
17	2.5	4	5	20	25
18	3	4	3	25	20
19	3.5	4	3	25	20
20	4	4	4	22	23
21	4.5	4	5	20	25
22	5	4	5	20	25

reasonable result for the resolution. The variation in these results is most likely a result of the amount of noise present in the individual images and how well the pixel edges lined up with the edges of the lines on the target.

In addition to the in plane-resolution, the depth of each image was calculated using the ResAnalysis code as described in Section 5.3. The depth measurements calculated from these images are presented in Figure 5.6a. The orange points are the hologram-calculated locations relative to the actual location of the target. The blue line is added as a reference to show the deviation of the calculated location from the measured location. Although this graph adequately demonstrates the scale of these deviations relative to the overall distances, it does not provide much insight into the relative differences in deviations from one point to another.

In order to better differentiate the deviations from one point to another, the data is presented in Figure 5.6b as the amount of error between the measured and

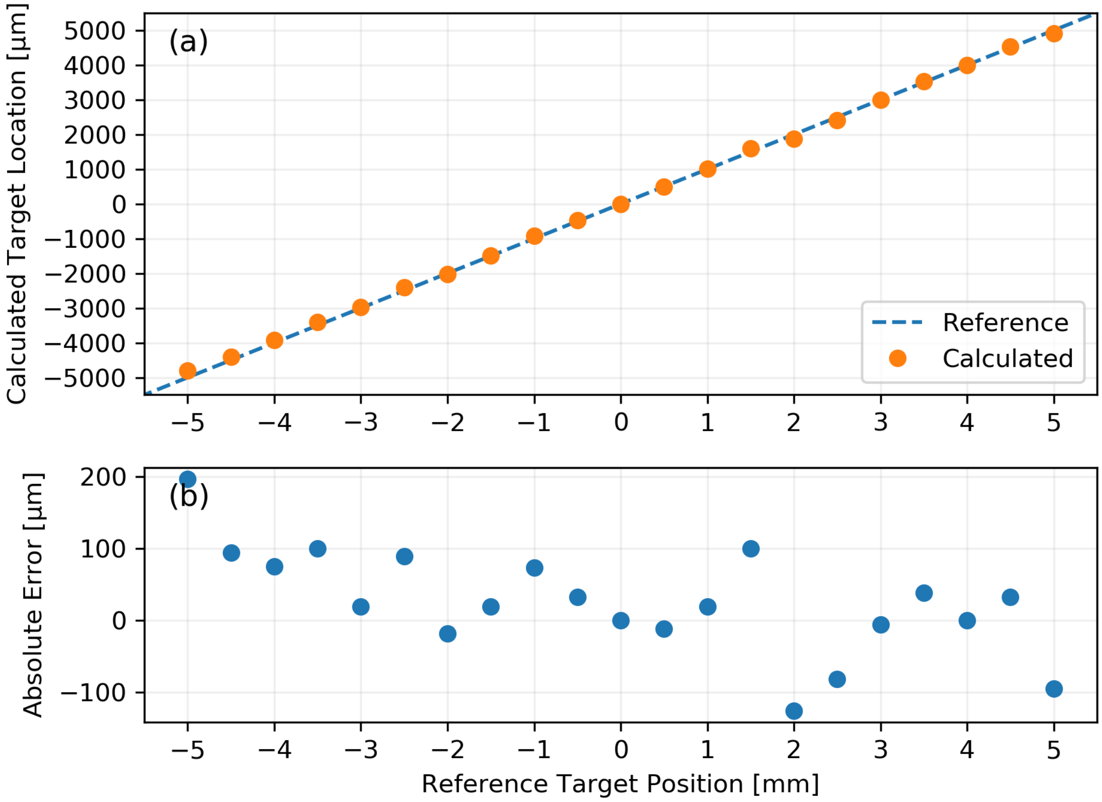

Figure 5.6: USAF 1951 target DIH calculated location and absolute error without magnification

calculated location for each image. All the deviations in this graph are less than 200 µm, and only one is more than 150 µm. The axial RSE of this error is 80.41 µm with an average error of 26 µm. Considering that the size of the ”particle” used for focusing the target is approximately 150 µm and that the PECA method is able to reliably focus to depths around 2x the particle size, these results match expectations for focusing.

Another important point to note in Figure 5.6b is that there is no significant correlation between the location and the amount of error. This lack of correlation demonstrates that there is no skewing of the location of the measurements along the path of the beam. In other words, the measurements are not deteriorating as the image moves away from the center starting point, at least over the range measured here. Since this range covers the majority of the inside of the chamber, there is no concern that the validity of particle location measurements will be different at different parts of the chamber. This result was expected since the collimation calibrations performed before collecting this data were meant to correct for these type of deviations. However, these additional data also demonstrate the validity of that method in correcting for any measurement skewing only relying on locations at the front and back of the area of interest instead of multiple images over the entire range.

5.4.3 USAF Target Resolution 4.57x Magnification

The magnification factor used in the ResAnalysis program was calculated using the method in Section 4.2.2 and found to be 4.57x. The location and error data using this magnification factor are presented in Figure 5.7. In comparison to the results without the lens, Figure 5.7b shows not only a greater error from the known location but a clear trend of an increase in error as the target moved away from the camera. The collimated lens for this setup had already been calibrated and the only other variable that had changed with the addition of the lens was the magnification factor.

5.4.4 USAF target resolution 4.63x Magnification

Since the magnification factor has an impact on the effective pixel size used in the reconstruction of the holograms, the magnification factor input into the ResAnalysis program has a direct impact on the output focused distance. By making slight adjustments to the magnification factor and recalculating the distance, the correlation between the error and location can be removed. Through an iterative process, it was found that using a magnification of 4.63x instead of

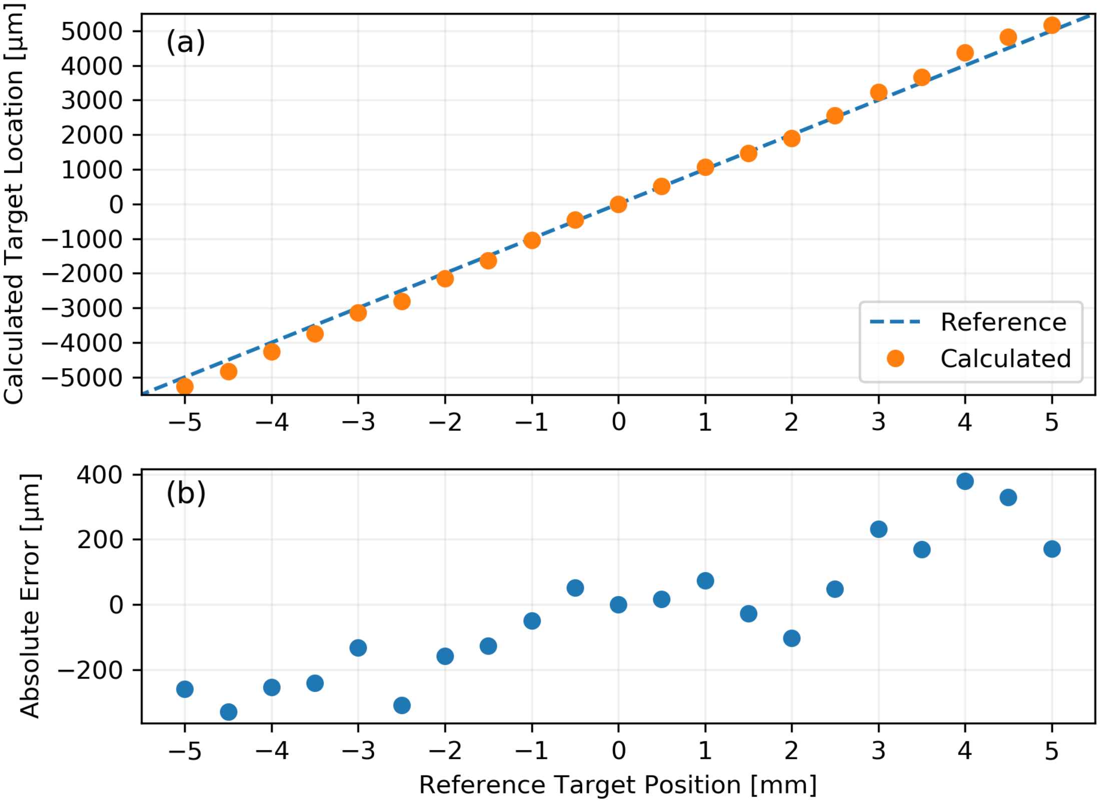

Figure 5.7: USAF 1951 target DIH calculated location and absolute error with lens magnification of 4.57x

4.57x succeeded in removing this correlation. The results using this updated magnification factor are presented in Figure 5.8.

The maximum error for the measurements shown in Figure 5.8 is under 150 µm with the majority being less than 100 µm. The RSE of the error was 66.63 µm with an average of 8 µm. Compared to the RSE of 80.41 µm measured without the lens, this is a slight improvement, but there does not seems to be a significant improvement in the accuracy of the depth measurement by increasing the magnification. This seems to point to the fact that the precision of this measurement is being limited more by the focusing method in relation to the particle size than the magnification of the image.

Table 5.3: USAF 1951 target in-plane resolution based on location with lens magnification of 4.63x

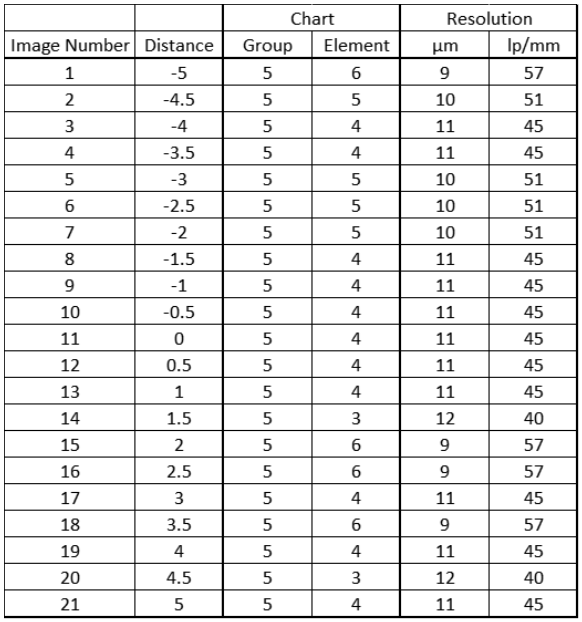

		Chart		Resolution	
Image Number	Distance	Group	Element	µm	lp/mm
1	-5	5	6	9	57
2	-4.5	5	5	10	51
3	-4	5	4	11	45
4	-3.5	5	4	11	45
5	-3	5	5	10	51
6	-2.5	5	5	10	51
7	-2	5	5	10	51
8	-1.5	5	4	11	45
9	-1	5	4	11	45
10	-0.5	5	4	11	45
11	0	5	4	11	45
12	0.5	5	4	11	45
13	1	5	4	11	45
14	1.5	5	3	12	40
15	2	5	6	9	57
16	2.5	5	6	9	57
17	3	5	4	11	45
18	3.5	5	6	9	57
19	4	5	4	11	45
20	4.5	5	3	12	40
21	5	5	4	11	45

Using this updated magnification factor, the in-plane image resolution was determined from the group and element numbers. The resolution of these magnified images as shown in Table 5.3 is between 9 µm and 12 µm with an average of 10.51 µm and a standard deviation of 1.1 µm. Based on the effective size of the pixels being 4.3 µm this resolution is less than expected. Upon inspection of these images in comparison to those captured without the lens, it appears that the lower resolution limit is being caused more by blurring and noise in the image than relative pixel size. This provides a possible explanation for the resolution being worse than expected. Even though the resolution is less than expected it should still be sufficient for measurements of lycopodium particles.

Based on these results, it is clear that a slight change in the magnification factor, 0.05 in this case, can result in significant changes to the resulting depth measurements. Therefore the lack of precision inherent in the dot chart method used in Section 4.2.2 means that it is not sufficient as a stand alone method in

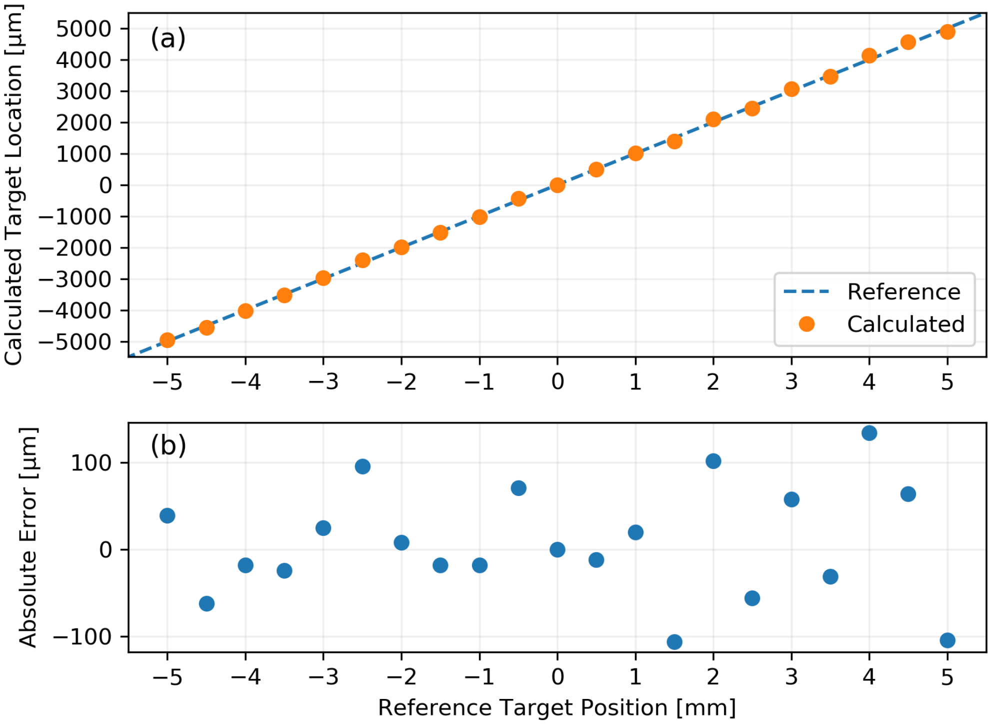

Figure 5.8: USAF 1951 target DIH calculated location and absolute error with lens magnification of 4.63x

determining the magnification and should be paired with a secondary calibration check similar to the one used for adjusting the collimating lens.

5.5 Dust Resolution

Although the USAF 1951 target was useful in determining the image resolution and providing an estimate of the axial resolution, it makes sense to use actual particles similar to those used in the dust dispersion chamber for a more realistic axial resolution measurement. The two particles used for this imaging were sugar and lycopodium. Sugar provided a particle size large enough for focusing without the camera lens, and lycopodium provided a smaller particle size with a more spherical shape and opaque optical qualities. The dust sample was sprinkled onto a borosilicate glass slide and placed in the mount. The

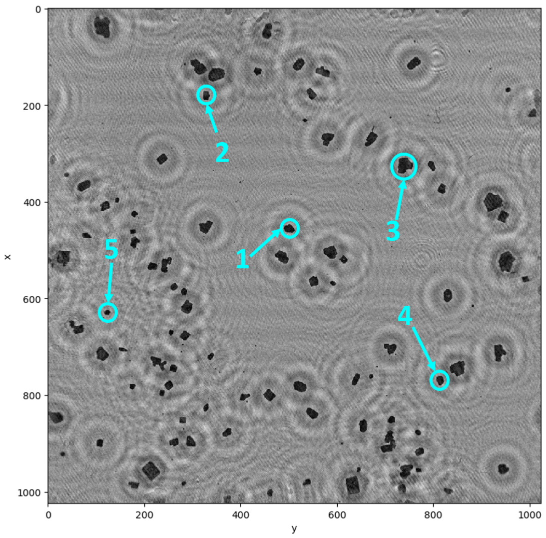

Figure 5.9: Location of sugar particles used for depth resolution analysis without magnification

ResAnalysis program was modified to iterate the PECA focusing method for five manually entered particle locations. Similar to the USAF target, the glass slide was imaged at 21 locations spaced by 0.5 mm.

5.5.1 Sugar Resolution Without Magnification

Although the USAF 1951 target was useful in determining the in-frame resolution of the reconstructed holograms, the opaque parts of the target are not three dimensional in the same sense as a dust particle. To get a more representative measure of the resolution of reconstructed holograms of dust particles, sugar particles were sprinkled on a piece of glass and imaged in the same method as the USAF 1951 target. The large size of the sugar particles allowed for imaging without the use of a magnification lens and therefore served as a good starting point for this analysis. The five particle locations selected for imaging are shown in Figure 5.9.

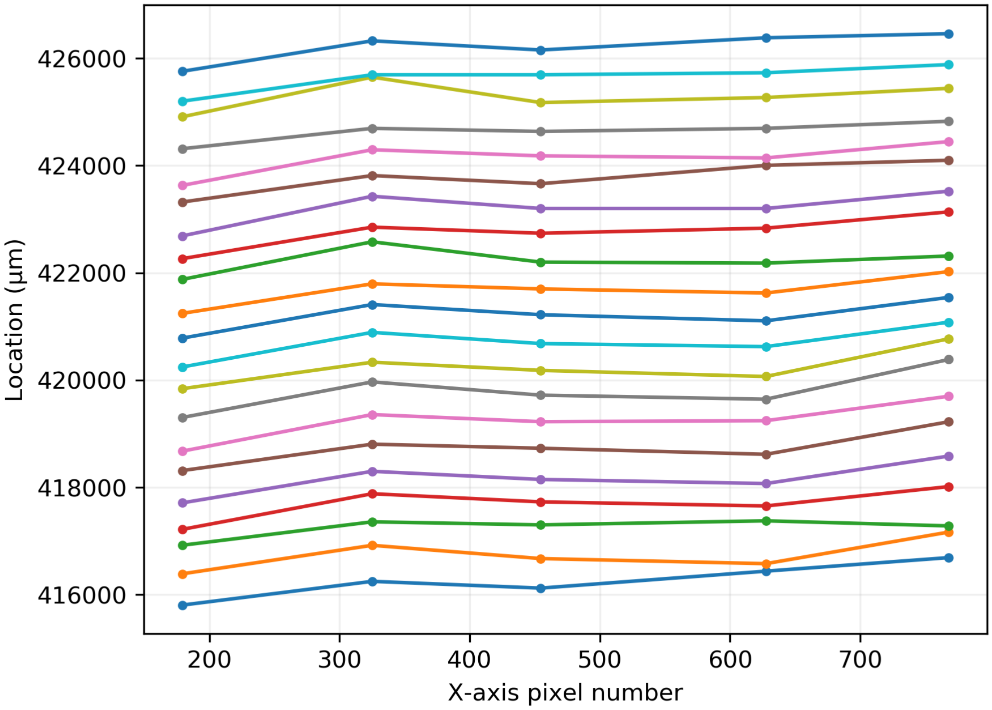

Figure 5.10: Sugar particle locations for images spaced by 0.5 mm captured without magnification; each series consisting of 5 particles is taken from a single image at a specific location

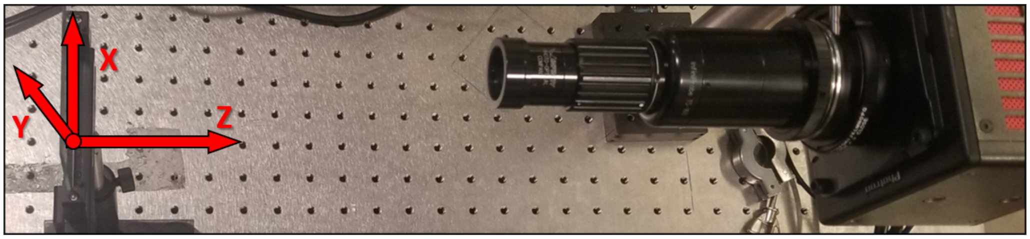

Figure 5.11: Axis locations relative to the resolution target and camera

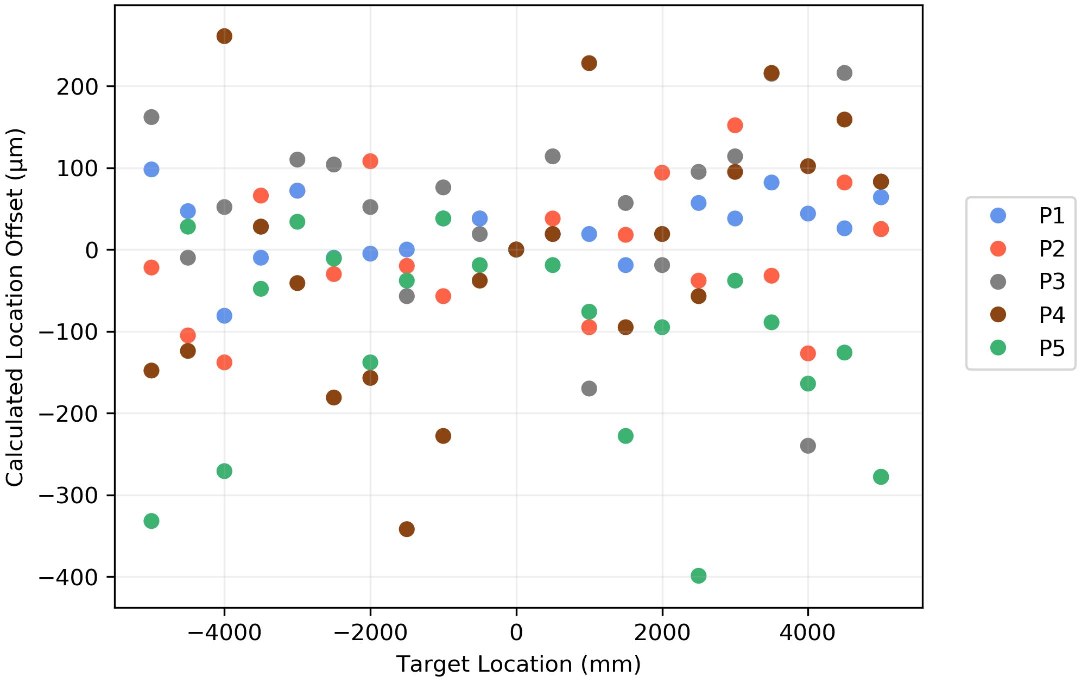

Figure 5.12: Error in DIH calculated sugar particle location as a function of the location of the glass slide; no magnification

Figure 5.10 shows the location of the focused particles at each 500 µm increment for which an image was taken. The lines connect particles captured in a single image. The X-axis on this chart matches the X-axis of the glass piece on which the particles were placed. As shown in Figure 5.11, this axis matches the rotational angle of the target mount relative to the camera and is therefore the most likely to cause misalignment between particles in the same image. This would explain the upward trend of each of the image sets in Figure 5.10. Outside of a few outliers, the particle locations relative to each other remain consistent from one image to the next as they are moved away from the camera. Also, the distance each particles moves between frames appears close to the actual 500 µm that the translational stage was moved.

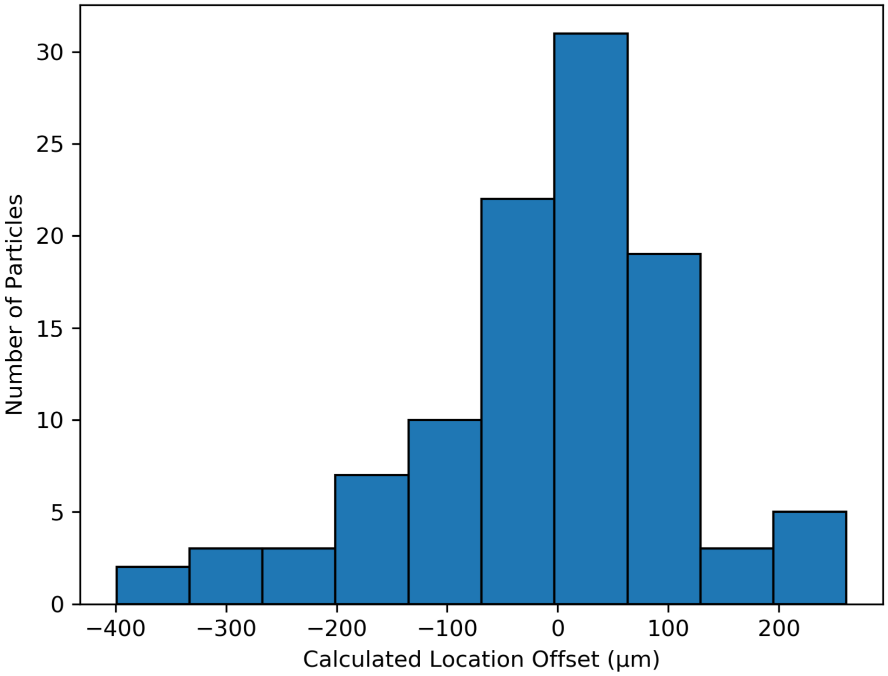

Figure 5.13: Distribution of sugar particle location error without magnification

To quantify the hologram calculated distance between images as compared to the known movement of the particles, the center image was treated as the zero point for determining the error between the calculated and measured distance for other locations. These errors are presented in Figure 5.12 as a function of the target location. This figure does not show any trends correlating the amount of error to the location of the measurement. In other words, the ability of this hologram method to determine the relative distance between two particles is not a function of the distance between the particles or the distance from the camera; at least over the range of distances used here. Figure 5.13 shows that the calculated error is not skewed to one side or another which is confirmed by average error being only -8.61 μm. The RSE for the location of the sugar particles was 121.78 μm which is significantly higher than the USAF target values. One possible reason for this discrepancy in resolution is that the translucence of the sugar particles and the misalignment between edges of the pixels and edges of the particles makes it more difficult for the program to determine a clear focused location compared to the USAF 1951 target.

5.5.2 Lycopodium Resolution Without Magnification

Lycopodium dust has the advantage of being opaque compared to sugar crystals which are somewhat translucent. The opaqueness of the lycopodium particles removes the additional variable of particle translucence that may have impacted the ability to focus on certain particles. Lycopodium is also one of the dusts used in the dispersion analysis performed in Chapter 7, and therefore it is useful to quantify the accuracy of the depth measurements taken for this dust. The main difficulty of measuring the lycopodium with this optical setup is that the particle sizes are small and therefore will only be captured by a couple of pixels if magnification is not used. For this reason, the depth resolution analysis for lycopodium was performed first without any magnification and then repeated with the magnifying camera lens.

For the analysis without magnification, Figure 5.14 shows the locations of the particles used for focusing. Since the particles are so small, some of these selected ″particles″ may not be a single particle but in fact an agglomerate of a couple of particles. The possible use of agglomerates in this analysis, results in some particles images that are not as spherical as would be expected for a single particle. This misshapeness though, should not affect the ability of the holography method to focus on the particles.

Figure 5.15 shows the five particle locations for each image taken at the 0.5 mm increments. Similar to the results from the sugar analysis, the general locations of the particles relative to each other remains consistent from one image

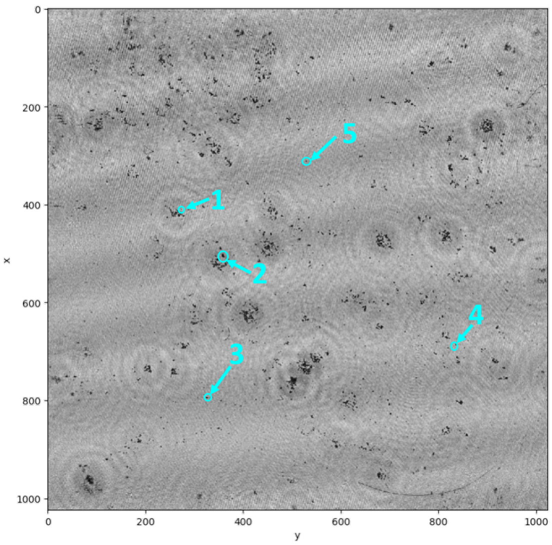

Figure 5.14: Location of lycopodium particles used for depth resolution analysis; no magnification

to the next. Unlike the sugar data, the set of particles for each image are not significantly angled in either direction, which would suggest that the glass plate was setup parallel to the front face of the camera when taking these images.

The error data for this lycopodium analysis is presented as a function of location in Figure 5.16 and as a histogram distribution in Figure 5.17. Similar to the sugar results, the error amount does not appear to be a function of the location of the particle in the image or the distance between the particle and the camera. From the histogram, there is a small set of outliers on the negative side, but the number of these is small enough that they are not of concern.

Compared to an RSE of 121.78 µm for the sugar particles, the lycopodium has an RSE of 146.19 µm with an average error of -35.08 µm. The decrease in accuracy for the lycopodium is probably a result of having fewer pixels to use when determining an in focus images. Fewer pixels used by a particle makes it more likely that slight changes in the values of any one of these pixels, caused by noise or other imperfections, could drastically change what is considered an in

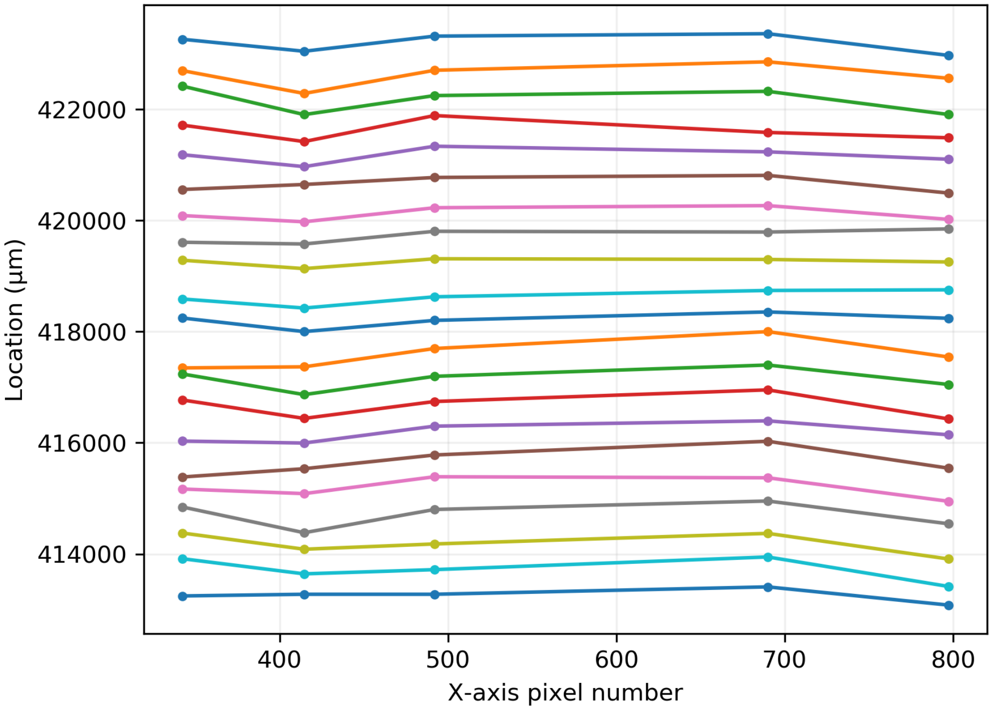

Figure 5.15: Lycopodium particle locations for images spaced by 0.5 mm captured without magnification; each series consisting of 5 particles is taken from a single image at a specific location

focus image. In actuality, the fact that the lycopodium and sugar particles had similar levels of accuracy may have been a result of the improvement from more opaque particles of a smaller size being offset by the decrease in number of pixels per particle. If this hypothesis is correct then magnified lycopodium particles should produce the most accurate results.

5.5.3 Lycopodium Resolution 4.63x Magnification

In order to determine the effect that using a lens to magnify the hologram images would have on the accuracy of the depth measurements, the resolution analysis was repeated with lycopodium and the camera magnification lens. The

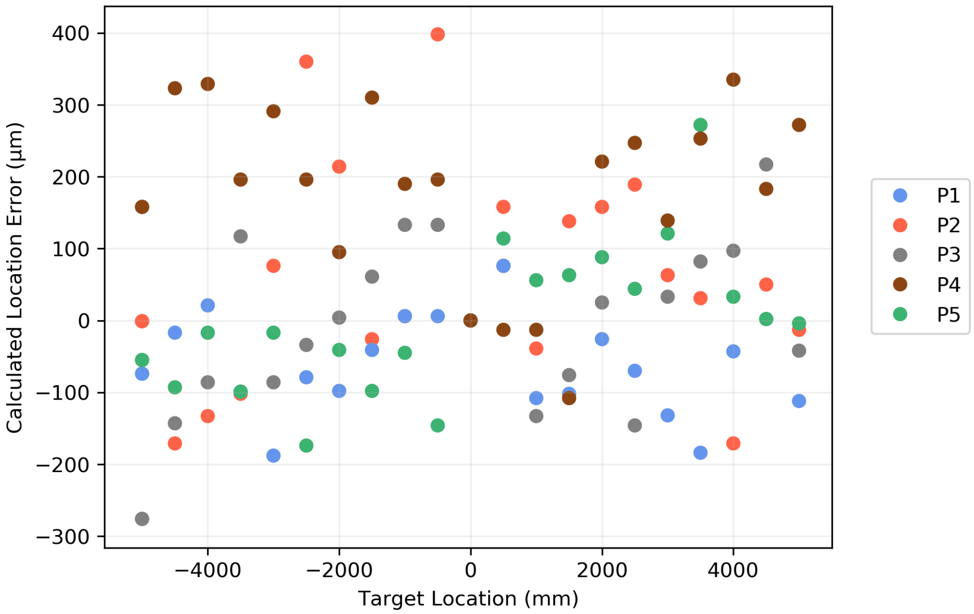

Figure 5.16: Error in DIH calculated lycopodium particle location as a function of the location of the glass slide; no magnification

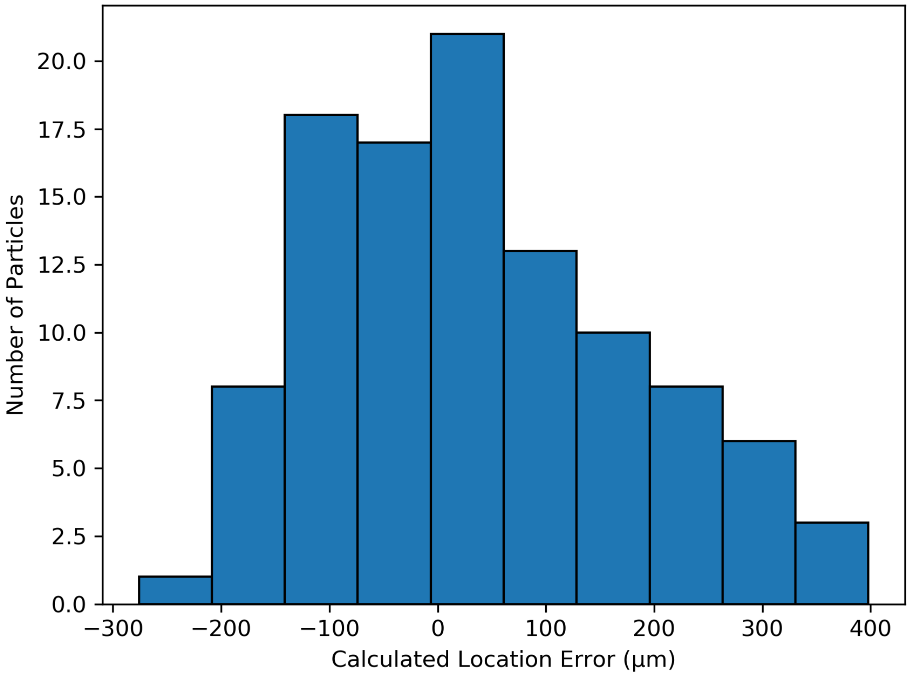

Figure 5.17: Distribution of lycopodium location errors without magnification

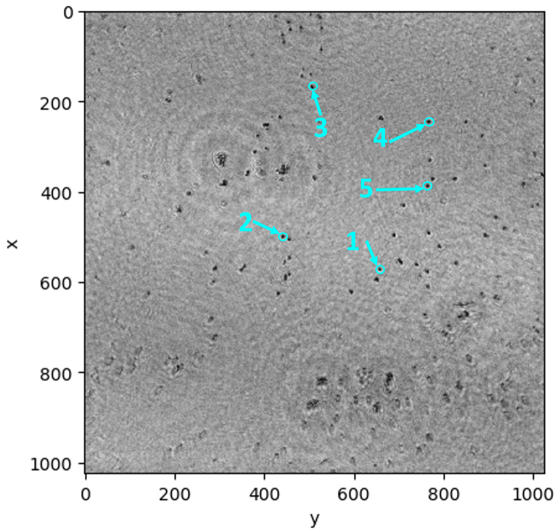

Figure 5.18: Location of lycopodium particles used for depth resolution analysis with magnification of 4.63x

locations of the lycopodium particles used in this analysis are shown in Figure 5.18. It is obvious that this image is magnified since the particles appear much larger than what was seen in Figure 5.14.

Figure 5.19 shows the depth measurement for the lycopodium particles measured with the magnification lens. The consistency of the particles relative locations from one frame to the next is noticeably better when using the lens than the two data sets collected without the lens (Figure 5.10 and Figure 5.15)

To better quantify this improvement, the error data is presented as a function of location in Figure 5.20 and as a histogram in Figure 5.21. Unlike the data sets collected without a lens, the direction of offset does seem to have a slight correlation with the distance from the camera. As discussed in Sections 4.2.2 and 5.4 the addition of the lens means that the magnification factor has an impact on the focusing distance. While a calibrating method was used prior to this analysis to determine the magnification factor of the setup, these results indicate the either the focal point of the camera changed or that the method was not able to

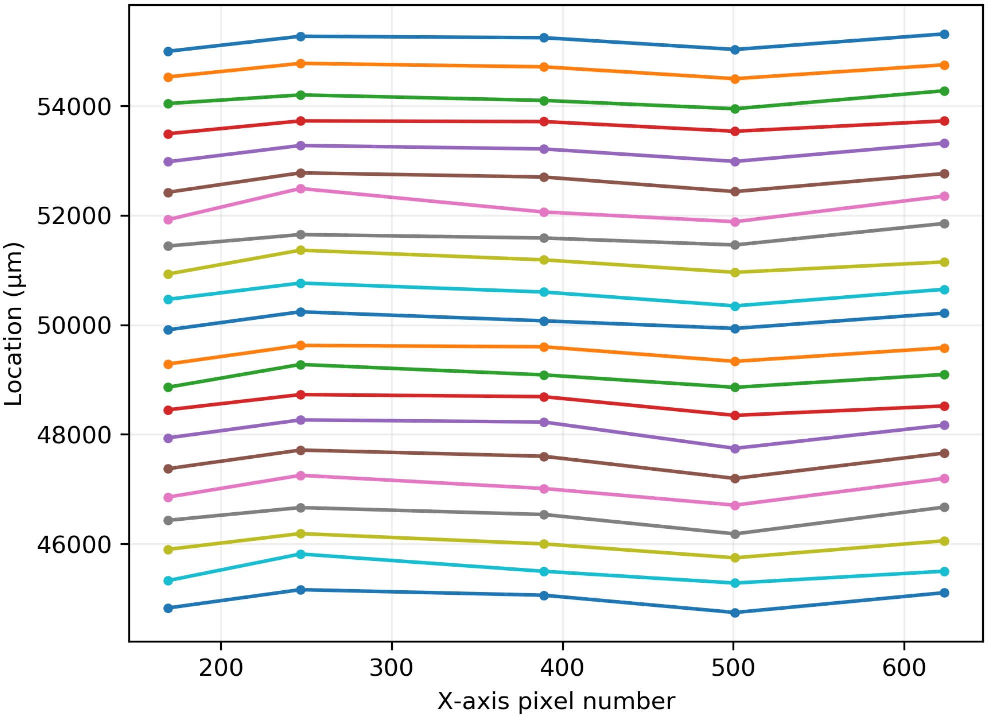

Figure 5.19: Lycopodium particle locations for images spaced by 0.5 mm captured with magnification of 4.63x; each series consisting of 5 particles is taken from a single image at a specific location

determine the magnification factor with sufficient precision.

In either case, the overall amount of offset is still an improvement from the lensless data sets. The RSE for the lycopodium with magnification was 98.5 μm (with an average error of -5.70 μm), compared to RSEs of 121.78 μm and 146.19 μm for particles located without magnification. This level of accuracy should be acceptable for most particle flow reconstructions, where relative particle depth is not as critical as particle size and general bulk flow characteristics. If more accuracy is needed, it appears that there is room from improvement in the calibration of the magnification factor created by the camera lens.

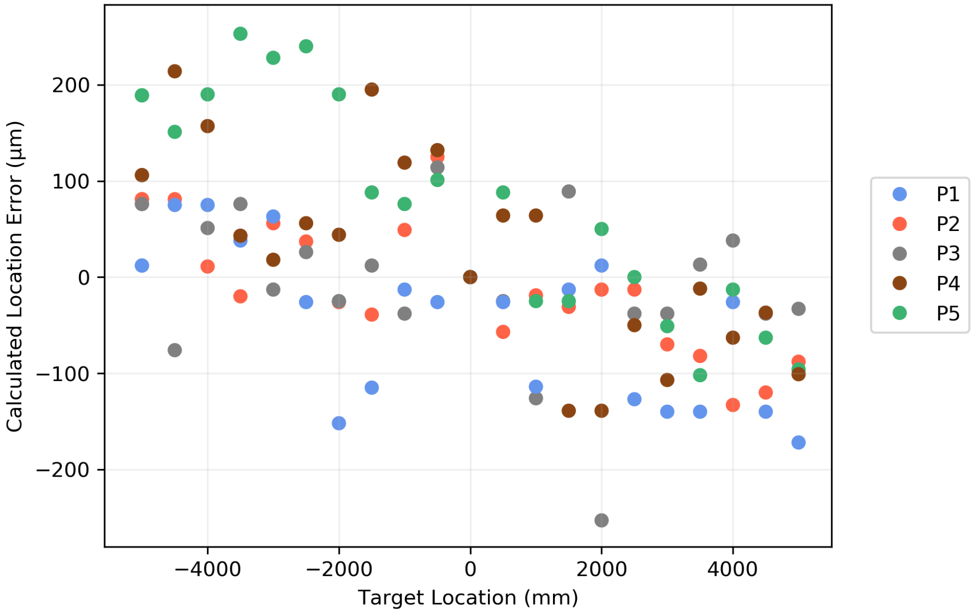

Figure 5.20: Error in DIH calculated lycopodium particle location as a function of the location of the glass slide; magnification of 4.63x

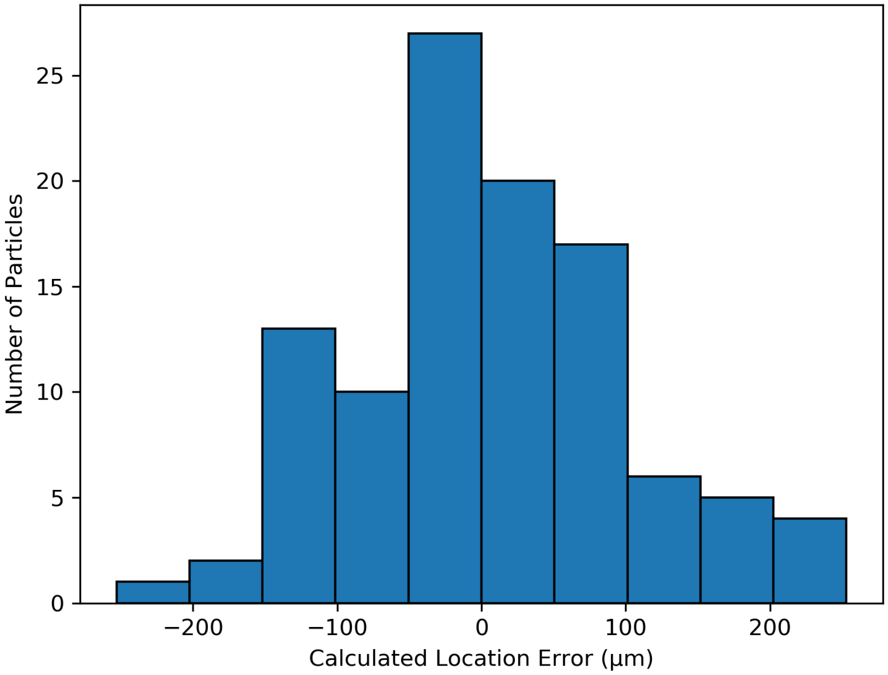

Figure 5.21: Distribution of lycopodium location errors with magnification 4.63x

5.6 Results and Discussion

Table 5.4 summarizes the results of each of the resolution studies that were performed. For the in-plane image resolution, the magnification increased the resolution of these images but not to the degree expected. As the effective pixel size decreased by a factor of 4.63, the smallest resolvable particle should also decrease by the same amount, but the decrease in error shown in these results is only about half of the original amount. While the level of resolution with the magnifying lens is acceptable for the particles being sized in this work, if smaller particles are used, further investigation into improving the resolution of this lens would be required. The average error was minimal enough that none of these data sets were considered skewed.

The axial depth location was calculated for the USAF target, sugar, and lycopodium without a lens. The USAF target had significantly less error than either of the dust particles, which can be attributed to the ‘particle’ edges for the target being more clearly defined and in line with the vertical and horizontal edges of the pixels. The sugar particle having less error than the lycopodium is likely a result of the lycopodium being only a few pixels in size and, therefore, any noise being magnified by the lack of data per particle. The axial depth RSE with the magnification lens was measured for both the lycopodium and the USAF target, and similar to the in-plane image resolution, there was a noticeable

Table 5.4: Summary of resolution studies and results

Resolution Study			Image Resolution [µm]		Axial Resolution	
Section	Object	Magnification	Mean	St Dev	Average Error	Axial RSE
5.4.2	USAF Target	1	20.31	1.88	26.00	80.41
5.4.3	USAF Target	4.52	–	–	-24.48	210.28
5.4.4	USAF Target	4.63	10.51	1.1	8.00	66.63
5.5.1	Sugar	1	–	–	-8.61	121.78
5.5.2	Lycopodium	1	–	–	-35.08	146.19
5.5.3	Lycopodium	4.63	–	–	-5.70	98.58

improvement but significantly less than the scale of the change in effective particle size. Comparing the improvement in mean image resolution ($\approx$ 1.9x) to the decrease in RSE for the USAF target ($\approx$ 1.2x) and lycopodium ($\approx$ 1.5x) with the addition of the magnification lens, all three improvements are on a similar scale. Although there is not sufficient data here to draw any conclusions about the relationship between the lens and resulting resolution, there do appear to be additional factors, besides magnification, which are affecting the amount of improvement in both the in-plane and axial resolution.

CHAPTER 6

DUST DISPERSION SETUP

The function of the dispersion chamber is to provide an enclosed volume for containing the dust cloud as it exits the dispersion nozzle. Because the field of view for holographic imaging of dust particles is limited to sizes on the scale of one cubic inch, the method does not lend itself well to visualizing the turbulent flow fields for the entire chamber. Instead, the best use for holographic imaging is recording detailed particle interactions at specific points of interest in the chamber. The two points in the Siwek chamber of greatest interest are the ignition point and the dispersion nozzle. To accurately recreate the turbulence at the ignition point for imaging would require a complete redesign of a 20-L chamber, which would be an overly expensive and time-consuming process with minimal additional insight from the current turbulence and composition measurement methods. In contrast, imaging of the flow near the nozzle can be investigated without recreating the entire chamber and provides more opportunity for new insight on particle interactions during dispersion.

Table 6.1: Siwek vessel test method parameters

Parameter	Value
Chamber volume	20 [L]
Initial Chamber Pressure	0.4 [bara]
Reservoir Volume	0.6 [L]
Reservoir Initial Pressure	21 [bara]
Ignition Delay time	60 [ms]

6.1 Dust Dispersion Chamber

Without the need to match the 20-L Siwek chamber design, a smaller chamber that would fit better into an optical imaging system was created. The initial chamber design consisted of a pipe in a transparent chamber with a small hole machined in the side to disperse dust through. The walls of this chamber were designed from sheets of acrylic plastic. While this setup provided a clear view for filming the dust flow from the nozzle, when attempting to image the flow with a holographic setup, imperfections in the acrylic distorted the image, as shown in Figure 6.1b. Further testing with a borosilicate glass sample showed some improvement but contained distortion patterns, as seen in Figure 6.1c.

To create a clear holographic image, laser windows (Edmund Optics P/N:38-059) were used in the final version of the chamber design shown in Figure 6.2. Since the entire chamber could not be made out of the laser window material, the remainder of the chamber body was machined out of aluminum. Two separate chamber lids were created, one containing a mesh top (McMaster-Carr P/N:92715T85) and one containing a pressure transducer and ball valve. The first lid allows for constant dust dispersion using a pressurized air stream without any pressure change in the chamber. The second lid design, along

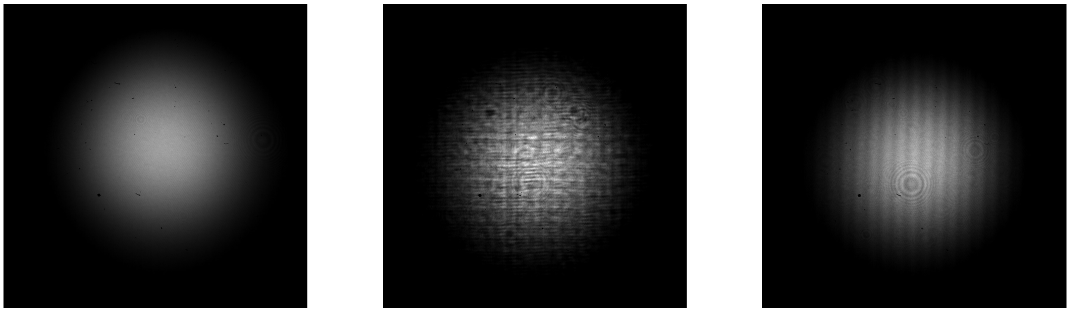
(a) No Chamber (b) Acrylic (c) Borosilicate Glass

Figure 6.1: Distortion caused by different chamber materials

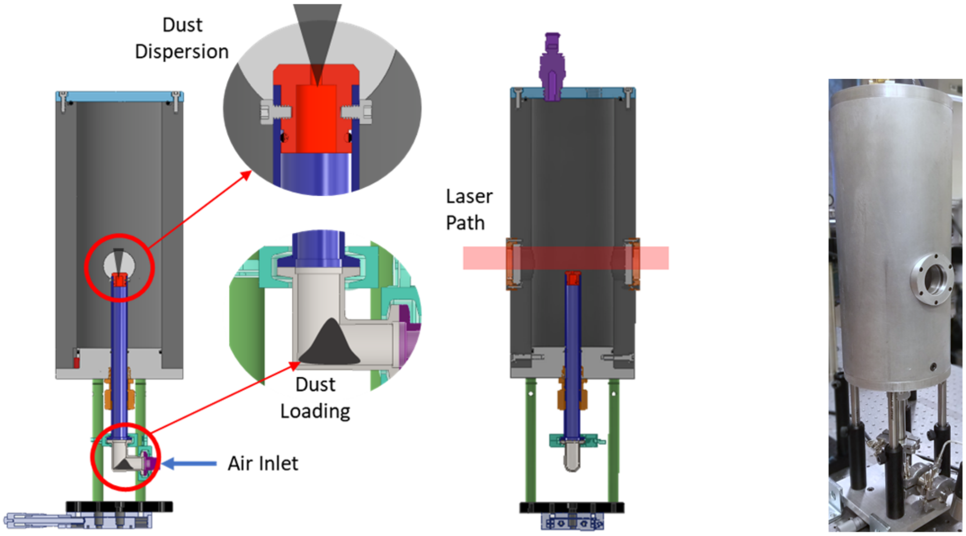

Figure 6.2: Dust dispersion chamber

with the inclusion of O-rings at mating surfaces in the chamber, allows for a vacuum to be pulled inside the chamber before dispersing the dust from a pressurized reservoir, bringing the chamber to atmospheric pressure. This second dispersion method is similar to the method used in the Siwek chamber described in Mercer [32] and shown in Table 6.1.

A singular hole in the dispersion pipe was used for the dispersion nozzle instead of a more complex nozzle such as the perforated annular nozzle. The advantage of a single hole over a more complex nozzle design was that it simplified the flow and provided more control over the dispersion variables. Flow through this nozzle can be modified simply through changes in the chamber or reservoir pressure or by modifying the nozzle size. The nozzle was designed as a pipe with an interchangeable cap containing the nozzle hole to allow for multiple opening sizes. For initial dispersion testing, caps with 2.5 mm and 5 mm holes were manufactured.

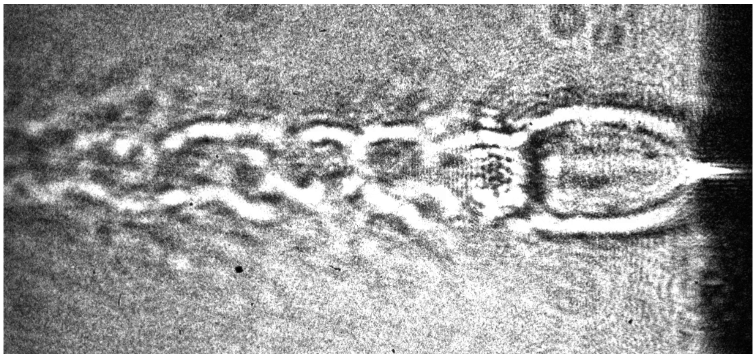

Figure 6.3: Standing shock wave at nozzle exit

The pipe was attached to the chamber through a cord grip which allowed the location of the nozzle to be moved up and down relative to the laser beam. In initial testing of this setup, it was discovered that a standing shock wave was present at the exit of the nozzle at higher pressures. The distortion of light from this wave, shown in Figure 6.3, prevented the imaging of particles at the exit of the nozzle. In order to get clear images for particle sizing, the nozzle was moved down one inch away from the laser beam path.

6.2 Pressure Dispersion System

Before collecting holographic images of dust dispersions, the pressure system was tested without dust over a wide range of conditions to characterize how the different pressures, timing controls, and nozzle diameters affected the flow into the chamber. The data presented in this chapter provides a detailed picture of the properties of the dust flow into the chamber and serves the purpose of relating the holographic results to the fundamental fluid dynamics at work.

Figure 6.4 shows a schematic and Figure 6.5 a picture of the entire dust dispersion system. When dispersing dust into the chamber, the dust sample is first loaded into the elbow part of the pipe (8) and clamps are used to seal these pipes. The filling hose (2) is attached to a pressurized air source (1) and the

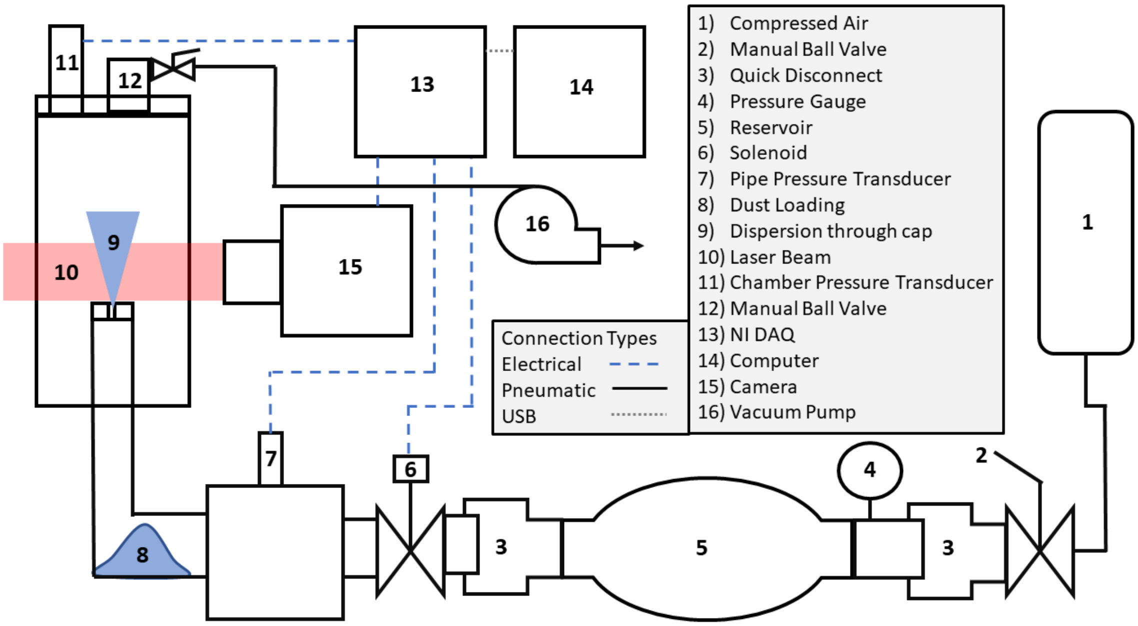

Figure 6.4: Schematic of the entire dust dispersion system

reservoir (5) is filled to the desired pressure, as shown by the pressure gauge (4), before closing a ball valve (2) at the inlet of the reservoir. The ball valve in the lid (12) is opened and a vacuum pump (15) is used to pull a vacuum of 0.4 bara in the chamber. A LabVIEW program (14) and National Instruments 6011 DAQ controller (13) is used to sync the opening of the solenoid (6) with the start of the video recording and to record the pressure in the chamber (11) and the pipe (7) as a function of time.

When selecting the reservoir size, the objective was to roughly match the initial and final pressures used for dispersion in the Siwek chamber (Table 6.1). Based on the volume of the chamber used in this setup (V_c) being 2.5 L, the ideal gas law can be rearranged and to solve for the necessary reservoir volume (V_r) to meet the Siwek pressures (P_{0c} = 0.4 bara, P_{0r} = 21 bara, and P_f = 1.01325 bara),

$$V_r = \frac{V_c(P_{0c} - P_f)}{P_f - P_{0r}} \tag{6.1}$$

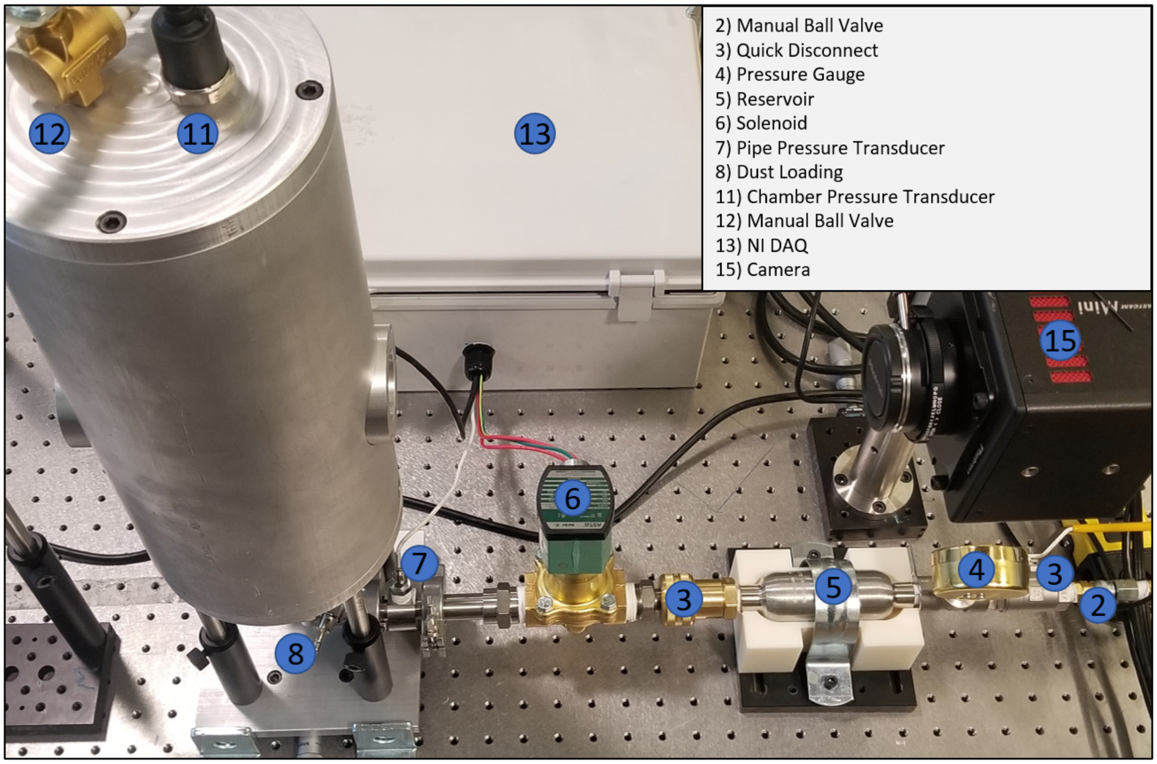

Figure 6.5: Picture of the entire dust dispersion system

From this calculation, the size of the reservoir should be 76.7 ml. A 75 ml reservoir was selected for use in this setup, understanding that the total volume of air in this section would be larger when the additional pipes and connections are considered.

In order to determine the exact relationship between the chamber and vessel volume, dispersion tests were run with varying vessel pressures. In these tests, a 0.4 bar vacuum was pulled in the chamber and the solenoid was left open for 2 seconds to ensure that the chamber and reservoir pressure had sufficient time to equilibrate. Figure 6.6 shows the relationship between the initial reservoir pressure and the final volume of the chamber in these tests. Based on these results, to reach a final chamber pressure of 1.01325 bara, when the initial chamber pressure is 0.4 bara, the initial reservoir pressure needs to be around 200

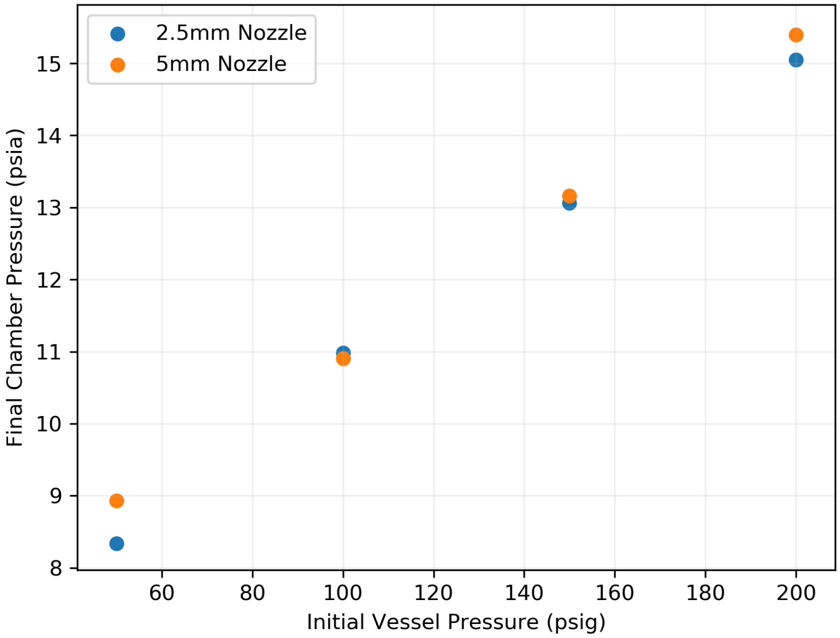

Figure 6.6: Final chamber pressure based on initial reservoir pressure when given time to reach equilibrium

psig. The reason behind aiming for a final pressure of 1.01325 bara (atmospheric) is to match the settings in Table 6.1 and prevent pressurizing the chamber, which may affect the particle flow.

For each dispersion test run, the pressure in the pipe and the pressure in the chamber were recorded as a function of time. For example, the pressure curves from a setup with an initial reservoir pressure of 200 psig and a 2.5 mm nozzle opening are shown in Figure 6.8. Under these conditions, it took 392 ms to complete the dispersion, after the solenoid was opened. Therefore, to match the 60 ms time used for filling the Siwek chamber, the initial pressure in the reservoir would need to be increased, which would also increase the final pressure of the chamber to above atmospheric pressure. In order to prevent over-pressurizing the chamber, the solenoid was used to limit the amount of air flow into the pipe,

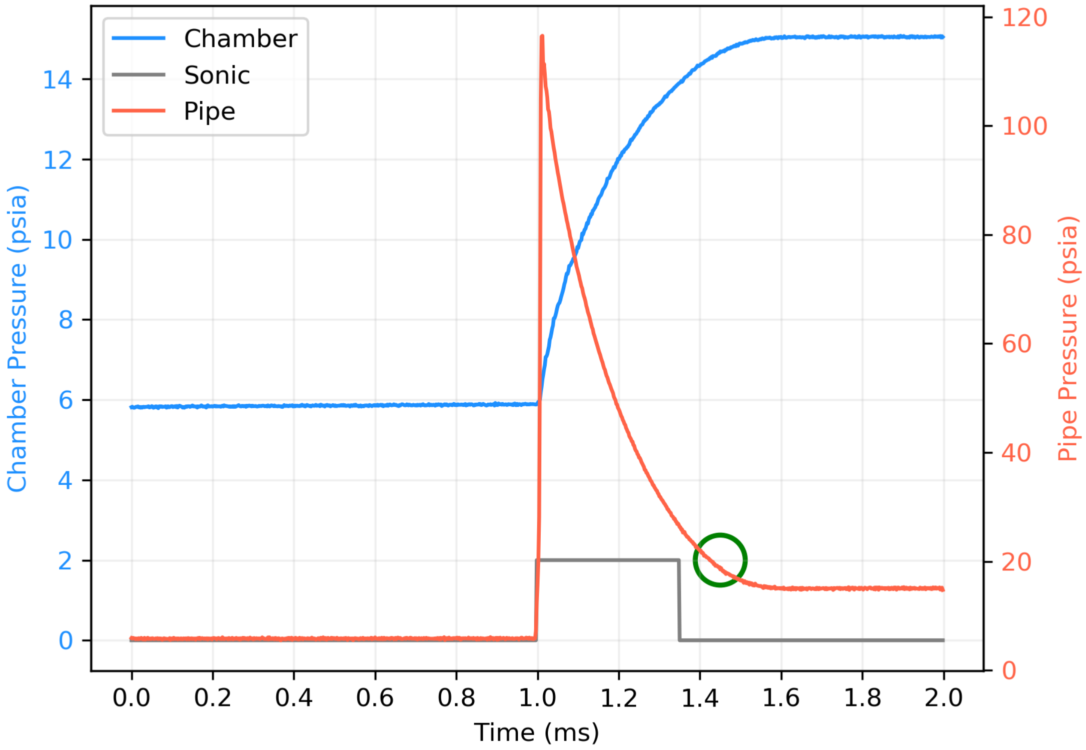

Figure 6.7: Chamber and Pipe pressure for an initial chamber pressure of 200 psi and a 2.5 mm cap

therefore trapping some mass in the reservoir and lowering the final pressure in the chamber. This process can be modeled using idea gas law similar to equation 6.1 but with a separate final pressure for the reservoir and chamber

$$V_r = \frac{V_c(P_{0c} - P_{fc})}{P_{fv} - P_{0v}}. \tag{6.2}$$

Therefore, for a given initial pressure, 200 psig for example, the necessary final pressure of the reservoir (to prevent overfilling the chamber) was determined to be 20.5 psig from equation 6.2. From the graph in Figure 6.7, the time at which the solenoid should be closed to achieve a final reservoir pressure of approximately 20 psi is approximately 0.45 s after the solenoid is opened (circled in green on 6.7).

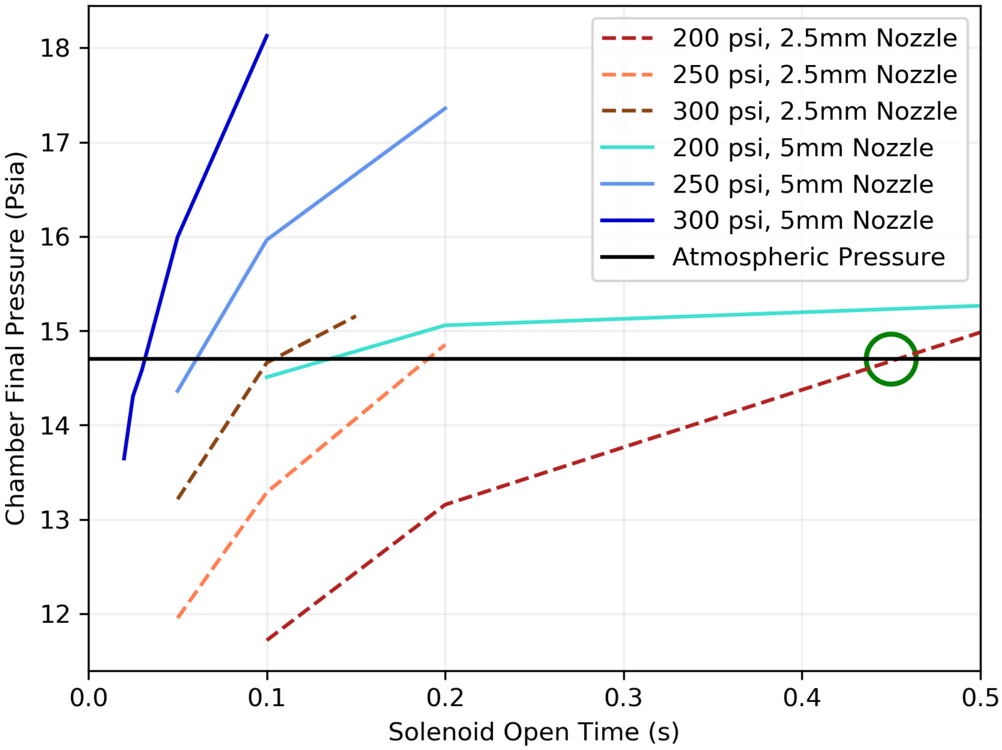

Figure 6.8: Final chamber pressure based on solenoid timing for different initial pressures and nozzle sizes

Figure 6.8 shows the experimentally determined values for the final pressure reached in the chamber based on the amount of time the solenoid was open, the initial vessel pressure, and the cap size. The 200 psi and 2.5 mm cap data shown in red on this graph crosses the line for atmospheric pressure at approximately 0.45s, matching up with the previous estimate using the ideal gas law. Since some of the components used in this setup are only rated to 350 psi, the maximum pressure used in this testing was 300 psi. The minimum pressure tested was 200 psi, since at lower pressures the vessel would not contain enough mass for the chamber to reach atmospheric pressure, regardless of how long the solenoid was open.

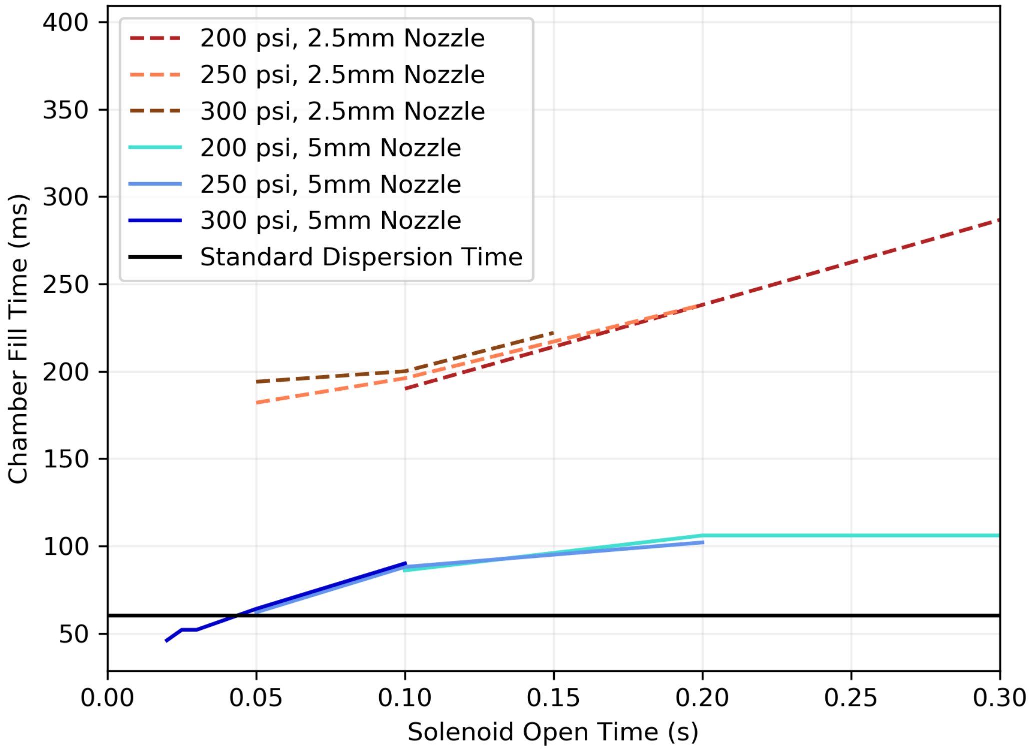

Figure 6.9: Time for complete dispersion based on solenoid timing for different initial pressures and cap sizes

Figure 6.8 serves as a useful guide for determining the relative solenoid timing necessary to prevent over-pressurization of the chamber. This rough estimate can be used to set up a test run for a specific initial pressure where the expected final pressure is slightly over atmospheric. The time to close the solenoid is the point where this line crosses the 14.7 psia line. As previously shown, the dispersion timing curve from this test can be used along with the ideal gas law to refine the solenoid timing necessarily to bring the chamber exactly to atmospheric pressure.

Once the initial and final pressures of the reservoir and chamber are balanced, the final parameter to characterize was the total time to disperse the dust. The dispersion time was defined as the amount of time required, after opening the solenoid, to reach 95% of the final pressure. Dispersion times are plotted as a function of the solenoid open time for different pressures and nozzle sizes in Figure 6.9. Nozzle size has the greatest effect on dispersion time, since the opening is the smallest cross-sectional area in the flow stream and therefore, the choke point of the system. Based on the equation for choked flow,

$$\frac{P^*}{P_0} = \frac{2}{\gamma+1}^{\frac{\gamma}{\gamma-1}} \tag{6.3}$$

where $\frac{P*}{P_0}$ is the pressure ratio at which sonic flow in the nozzle is reached and γ is the heat capacity ratio (1.4 for air), any pressure ratio above 1.89 between the pipe and chamber will result in a sonic choked flow. A line was added to Figure 6.7 to show when the pressure differential meets these conditions and is therefore sonic. Since a large part of this flow period is sonic, an increase in the pressure of the reservoir will not be able to significantly change the dispersion time. The only methods for decreasing the dispersion time are to lower the amount of mass going into the chamber by closing the solenoid earlier or to increase the size of the nozzle opening. These fundamental principles about sonic flows are clearly reflected in the experimental results presented in Figure 6.9.

In summary, if a shorter dispersion time is needed, the solenoid time must be restricted based on the trend shown in Figure 6.9. To avoid over or under pressurizing the chamber, Figure 6.8 can be used to determine the approximate pressure necessary, for a given solenoid time, to ensure the chamber reaches atmospheric pressure. After an initial test run at these conditions, the pipe and chamber pressure curves can refine initial pressure and solenoid timing to get the exact output conditions desired. One last important note on these pressure data results is that for the higher pressures used (>200 psi), the majority of the flow will be a choked sonic flow.

CHAPTER 7

PARTICLE BREAKAGE ANALYSIS

The motivation behind this analysis is to measure the amount of particle breakage using the unique dispersion system developed in Chapter 6, in combination with a holographic particle sizing method utilizing the Sandia Particle Holography Processor (Section 7.1), to analyze images captured with the optical system described in Chapter 4. The validity of this method compared with previous particle breakage analysis can then be quantified. The two dust samples selected for particle size measurement were lycopodium and ascorbic acid. Some background on each of these materials and reasoning for their selection is provided in Section 7.2. Comparisons of the pre- and post-dispersion particle diameter distribution and percentage change are provided in Section 7.3 for the lycopodium at 200 psi and the ascorbic acid at 100, 200, and 300 psi. A summary of these results and a detailed discussion are presented in Section 7.4.

7.1 HoloSand

The software used for analyzing the particle size in the post dispersion dust cloud was the Sandia Particle Holography Processor (HoloSand) suite of MATLAB based scripts and functions. HoloSand was developed by Dr. Daniel Guildenbecher and the Sandia National Laboratory for analyzing particle motion recorded in hologram images [20]. Previous studies have used this software to track blood splatter droplets [10] and to analyze dust dispersion in an Kühner MIKE3 MIE device [44]. The code relies on the Hybrid method developed by Gao et al. [18] and Guildenbecher et al. [21] for particle focusing and detection, which is described in more detail in Section 2.3.3. The most significant advantage of using this method is that particle detection is included as a part of the focusing

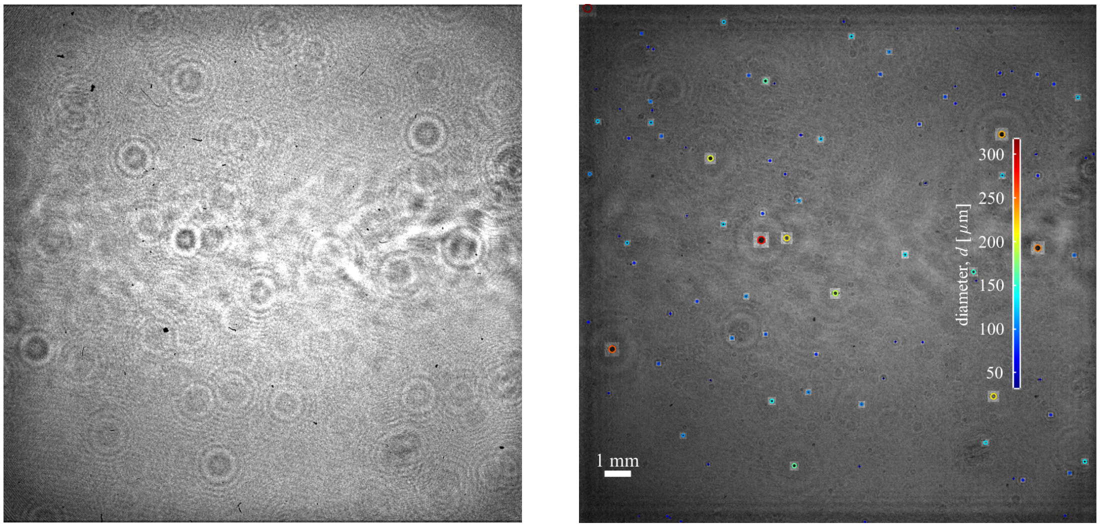

(a) Frame from dispersion video (b) HoloSand results from frame (a)

Figure 7.1: HoloSand input and output frame from ascorbic acid video

method, so unlike the ResAnalysis code, there is no need to enter particle locations manually. HoloSand was used to measure the diameters of the particles in each frame during the dispersion process. Figure 7.1b demonstrates an example of the output image that HoloSand produces from a single frame, shown in Figure 7.1a, of an ascorbic acid dispersion video. In addition to this output image, the program saves the particle location and size data for use in subsequent analysis.

7.2 Dust Materials

Two dust samples were selected for comparison and validation of the accuracy of this holographic imaging system in recording particle sizes during dispersion into the chamber. These dust samples were lycopodium and ascorbic acid. Both materials have been investigated in studies by Sanchirico et al. [42] and Bagaria et al. [5] [4] into the degree of dust breakage resulting from dispersion. Of the dust samples that Sanchirico tested, lycopodium had the most elasticity and experienced the most negligible breakage, whereas ascorbic acid

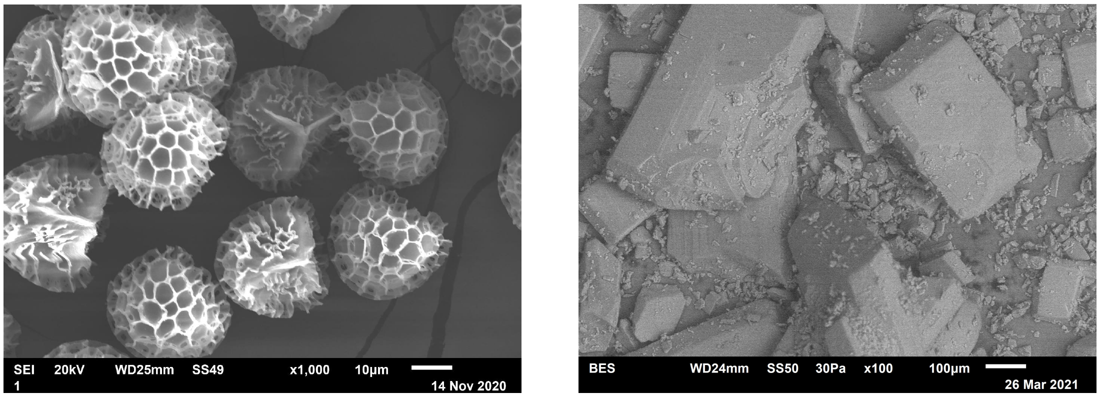

(a) SEI of lycopodium at 1000x

(b) BES of ascorbic acid as 100x

Figure 7.2: SEM images of pre-dispersion dust samples

exhibited the least elasticity and experienced extensive breakage. Being at opposite ends of the spectrum as far as particle breakage, these two materials were selected as they provide a comparison to each other and to previous results.

Each sample was imaged before testing using a JEOL JSM 6510 LV SEM to estimate the shape and size of the particles. In the 1000x secondary electron image (SEI) of lycopodium, Figure 7.2a, the particles appear monodisperse in the range of approximately 30 - 40 μm. The sponge-like structure of these particles explains the high elasticity (Young's modulus of 2.3 GPa) observed by Bagaria et al. [4]. The 100x backscatter electron image (BEI) of ascorbic acid, Figure 7.2b, shows a wider range of particle sizes with the largest lengths in the range of 300-400 μm. The more crystalline structure of these particles matches with the brittle Young's modulus of 40.36 GPa measured by Bagaria et al [4]. In addition to the difference in material properties, the significant difference in the average and range of the diameter distribution will be useful in testing the feasibility of accurately imaging particles both with and without magnification.

The pre-dispersion particle size distribution was collected using a Malvern Mastersizer 3000 with a Fraunhofer scattering model. The pre-dispersion particle size distributions are presented for comparison to the DIH measured post-dispersion distributions in Figure 7.6 for lycopodium and Figure 7.9 for ascorbic acid.

7.3 Hologram Results

7.3.1 Lycopodium

Table 7.1 shows the system settings for each dispersion test that was performed and analyzed. For the lycopodium dispersion the time frame where the dispersion was occurring, and a significant number of particles were detected, was approximately 75 ms. After this time period, the accumulation of particles on the windows of the chamber began blocking out diffraction patterns from the particles in the chamber, and therefore HoloSand was unable to continue detecting particles.

To reduce the noise from the variation in number of particles from one frame to the next, the measured diameters from 32 consecutive frames (5 ms) were combined into one data set. Figure 7.3 shows a histogram of the diameters from one such dataset captured from 40 ms to 45 ms after the beginning of the dispersion process. The range of particle sizes in this dataset is greater than expected, and further discussion of this discrepancy is included in comparison to the volumetric pre-dispersion particle distribution later. This histogram is based

Table 7.1: Dispersion trial settings

Material	Magnification	Pressure [Psi]	Solenoid Time [s]	Cap Size [mm]	Concentration [g/m^3]	Dust Amount [g]
Lycopodium	4.63	200	0.2	2.5	100	0.25
Ascorbic Acid	1	100	1	2.5	250	0.75
	1	200	0.2	2.5	250	0.75
	1	200	0.1	2.5	250	0.75

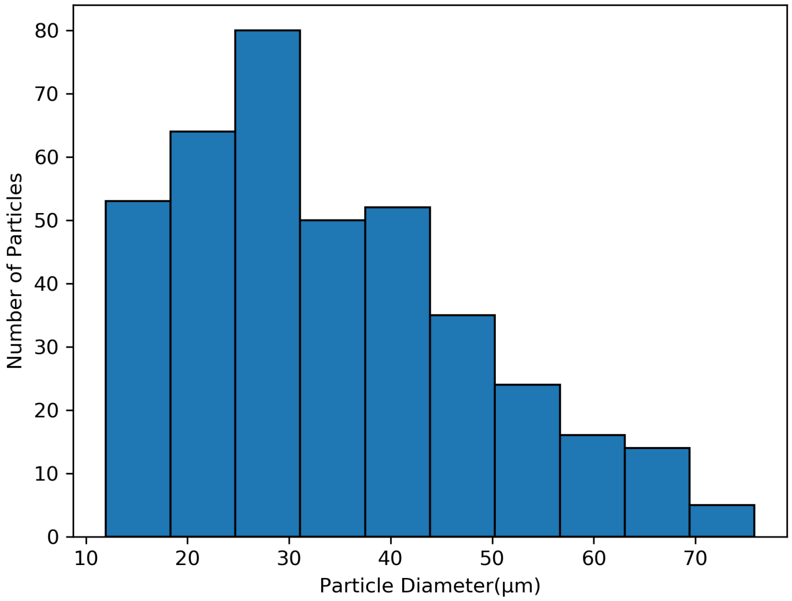

Figure 7.3: Lycopodium particle size distribution 45 ms into dispersion

on the diameter of the particles and for this lycopodium dataset the center of this distribution is around 30 µm. Figure 7.4 combines all of the data sets into one plot and demonstrates that the particle size distribution is consistent throughout the dispersion process.

For reference, Figure 7.5 shows the number of particles present in each distribution in Figure 7.4. This chart demonstrates that the amount of particles entering the frame increased throughout the dispersion process until reaching a peak and then sharply falling off. Based on visual inspection of the images from this time frame, the reason for this decrease in particles numbers is an accumulation of dust particles on the widows of the chamber scattering the laser light to the point where individual particles are no longer decipherable. The particles on the windows are not within the focusing distance set in the HoloSand program, therefore, the program will not interpret them as particles. This is by

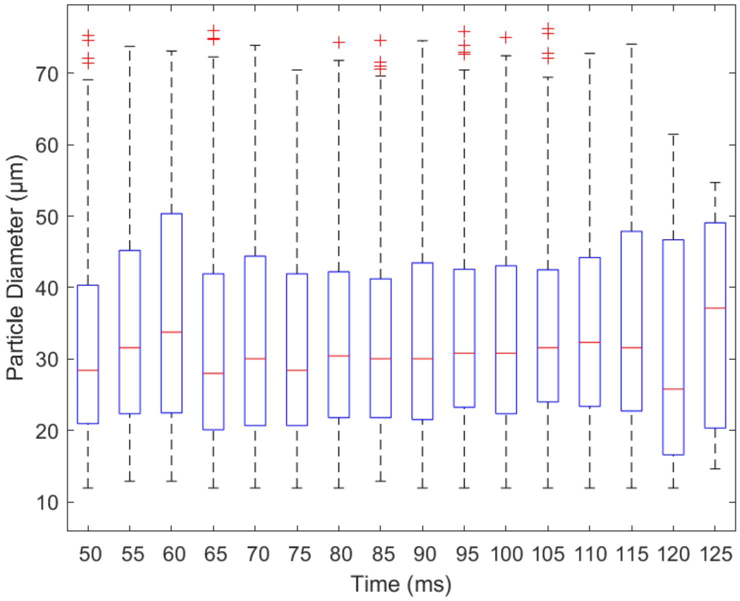

Figure 7.4: Lycopodium particle distributions over time

design since these particles are not randomly passing though frame but remain in view from one frame to the next and might skew the size distribution if they are identified as particles.

In order to get a complete distribution for comparison to the pre-distribution particle size analysis, all particle sizes for the entire run were combined one distribution in Figure 7.6. This distribution is presented as a volume weighted distribution on a logarithmic scale for comparison to the particle analysis data. The two values used to quantify the location of this distribution, the particle diameter median and mode are shown for both the pre-dispersion and post-dispersion dust clouds. The percentage of decrease in each of the values was also calculated and presented in Table 7.2 . As is expected based on previous studies and the material properties of the lycopodium, the median and mode of the distribution are relatively consistent. The mode diameter decreased from 27.4 µm to 24.1 µm and the median actually slightly

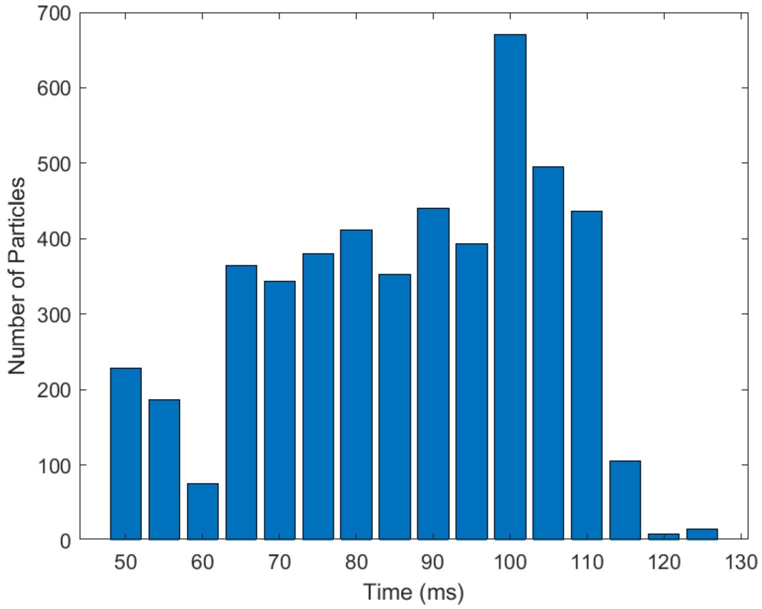

Figure 7.5: Number of lycopodium particles per group in Figure 7.4

increased from 30 µm to 30.8 µm, but neither of these values is large enough to be considered significant breakage or agglomeration.

While the center of the particle distribution remained fairly constant, as expected, the width of the distribution did expand during the dispersion process. This spreading of the distribution points to either some level of particle breakage and agglomeration or a lack of accuracy in the holographic particle sizing method. Some possible issues from the software analysis include, recording noise as particles, counting multiple particles as one, and blurring of particles causing incorrect sizes in the image. Further investigation into the possible reasons for this distribution change could include post dispersion testing of the lycopodium samples, further video analysis of dispersion under different conditions, and further work with the HoloSand program to attempt to determine if some error or noise in the process is causing this spread.

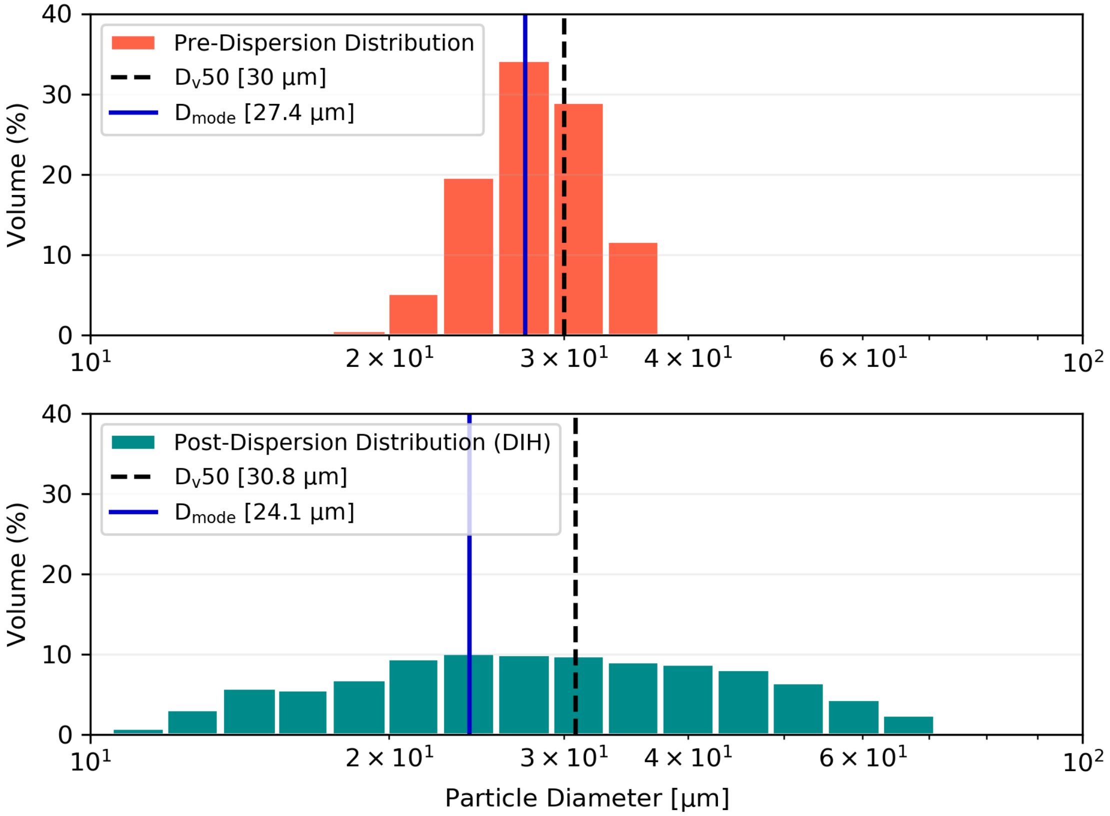

Figure 7.6: Volume based lycopodium particle size distribution pre and post-dispersion

7.3.2 Ascorbic Acid

The hologram measured particle size data collected for ascorbic acid was similar to that of lycopodium but was dispersed in three separate trials with pressures of 100 psi, 200 psi, and 300 psi respectively. The concentration used for these trials was 250 $\mathrm{g\,m^{-3}}$ and since the particles were large enough to detect without magnification the lens was removed from the camera to increase the field of view. The summary of all the trial settings is included in Table 7.1.

The video captured for these three distribution was 100 ms total with the frames being broken up into set of 5 ms, similar to the lycopodium dispersion. Figure 7.7 demonstrates that the particle diameter distribution does not

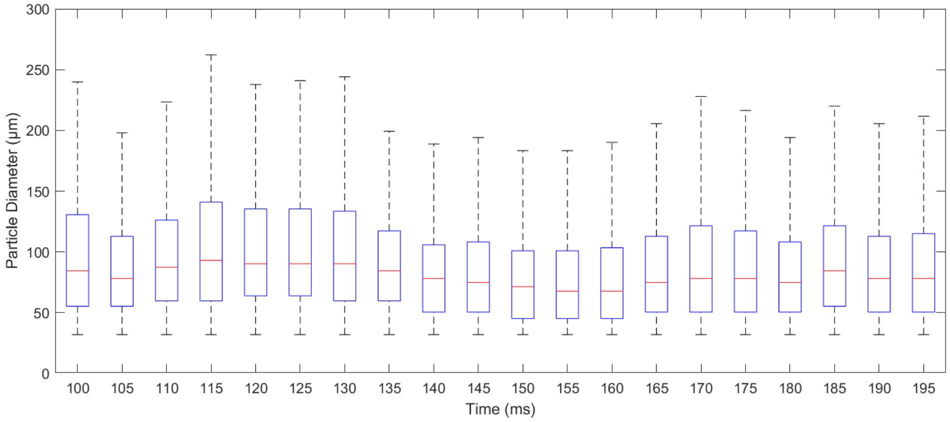

Figure 7.7: Ascorbic acid particle distributions over time

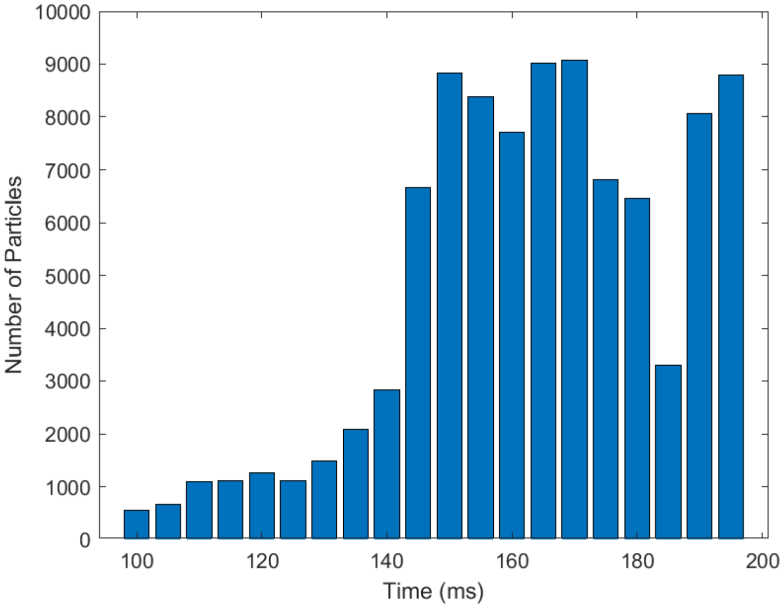

Figure 7.8: Number of ascorbic acid particles per group in Figure 7.7

significantly change throughout the dispersion process. The larger number of particles that were detected throughout this dispersion led to a larger number of outliers from the data which were removed from this figure for clarity. The number of particles detected throughout the dispersion process is shown in Figure 7.8. Although this figure shows an increase in the number of particles throughout the dispersion, this change does not have a noticeable impact on the distribution in Figure 7.7. Therefore, it can be assumed that the particle distribution is relatively consistent throughout the dispersion process and even if the entire dispersion is not captured and analyzed, a segment of 100 ms should be sufficient to measure the particle distribution.

To compare to the pre-dispersion data, the DIH particle data was weighted by volume and plotted against a logarithmic scale in Figure 7.9. Unlike the lycopodium, which saw little to no change in the location of the particle distribution, the dispersion process for ascorbic acid resulted in a downward shift in the center of the distribution. The median particle diameter decreased from 190 µm to 87.4 µm and the mode diameter decreased from 240 µm to 76.0 µm after dispersion into the chamber at 100 psi. Additionally, as the pressure of dispersion increased the distribution shifted downward. At 200 and 300 psi the distribution takes on a bimodal distribution with the two modes located at 66.9 µm and 35.3 µm. While the location of these modes does not change between 200 and 300 psi the volume percentage of the lower mode is greater for the 300 psi dispersion. The median of the distribution decreases from 87.4 µm at 100 psi to 74.8 µm at 200 psi and 71.4 µm at 300 psi. In summary, these results demonstrate that the dispersion process causes a particle size reduction for the ascorbic acid which increases with pressure.

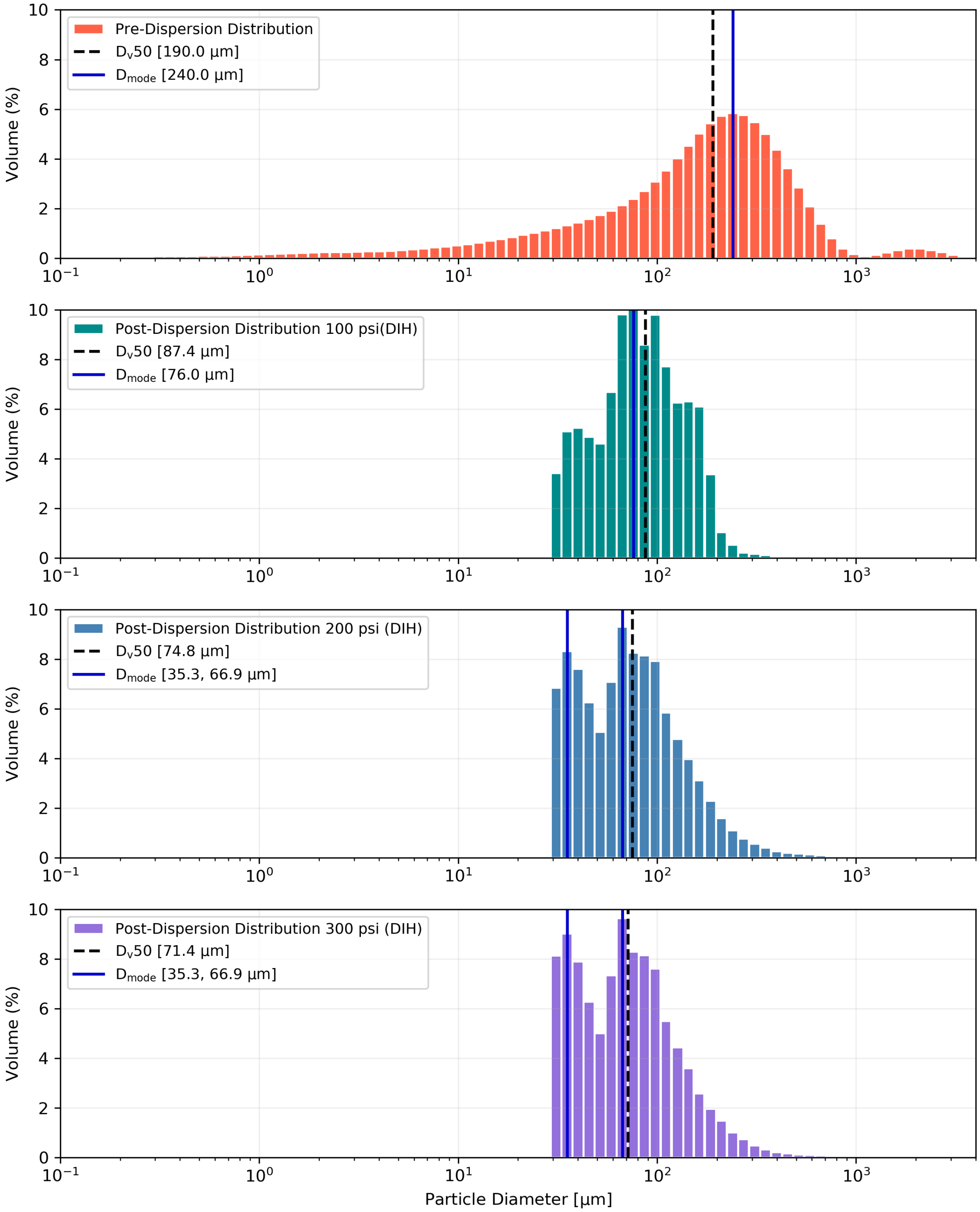

Figure 7.9: Volume based ascorbic acid particle size distribution pre- and post-dispersion

7.4 Discussion

The change in particle size observed for both the lycopodium and ascorbic acid dispersion trials is summarized in Table 7.2. The percent of change of particle diameter ($\%\Delta D$) for the median and mode is calculated from the equation

$$\%\Delta D = 100 * \frac{D_0 - D_f}{D_0} \tag{7.1}$$

where D_0 is the initial and D_f the final median or mode. A positive value for this percentage represents a decrease in particle size (most likely as a result of breakage) and a negative number represents an increase (most likely due to to agglomeration).The causes of particle breakage in the dispersion process are particle collisions with the sides of the pipe, the opening of the nozzle, the sides of the chamber, and other particles in the turbulent flow. While this method of measuring particle sizes near the nozzle during the dispersion process should avoid capturing breakage from the chamber walls and turbulence in the chamber, there is no way to delineate the extent to which the pipe walls, nozzle, and pipe turbulence is contributing to the breakage. Due to the small amount of material dispersed in each test, post dispersion particle processing was not feasible, but if enough tests were conducted to collect a large enough sample of post dispersion dust, this analysis might be used to compare the amount of breakage observed near the nozzle exit to the amount that occurs in the chamber.

Table 7.2: Comparison of change in particle median and mode after dispersion

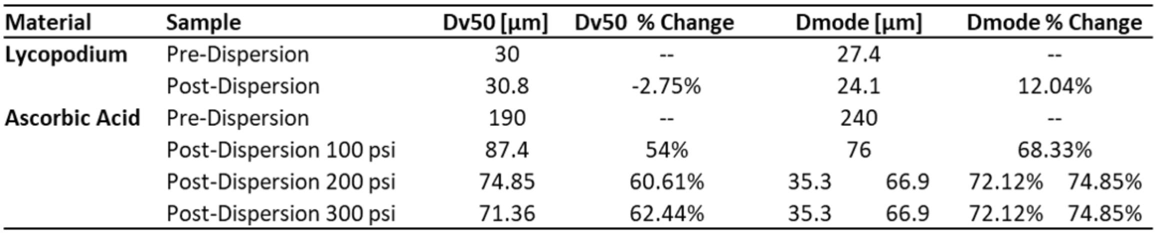

Material	Sample	Dv50 [µm]	Dv50 % Change	Dmode [µm]	Dmode % Change
Lycopodium	Pre-Dispersion	30	--	27.4	--
	Post-Dispersion	30.8	-2.75%	24.1	12.04%
Ascorbic Acid	Pre-Dispersion	190	--	240	--
	Post-Dispersion 100 psi	87.4	54%	76	68.33%
	Post-Dispersion 200 psi	74.85	60.61%	35.3 66.9	72.12% 74.85%
	Post-Dispersion 300 psi	71.36	62.44%	35.3 66.9	72.12% 74.85%

Table 7.3: Breakage class requirements as defined by Bagaria et al. [4]

Breakage Class	Diameter Change
BCI	$\Delta D\% \geq 50\%$
BCII	$20\% < \Delta D\% < 50\%$
BCIII	$\Delta D\% \leq 20\%$

Comparison between the lycopodium and ascorbic acid results show a significant difference between the amount of breakage. This matches results from previous studies. In one such study, Sanchirico et al. [42] defined a classification system for dusts based on the percentage decrease of diameter, with Class 1 including dusts for which $\Delta D < 50\%$ and Class 2 dusts where $\Delta D > 50\%$. Bagaria et al. [4] expanded this categorization into three breakage classes (BC) based on the requirements in Table 7.3. Based on these requirements, the DIH particle sizing data would classify the ascorbic acid as BCI and the lycopodium as BCIII which are the same classifications that Bargaria et al. found for these materials.

The ascorbic acid median particle distributions in Table 7.2 also demonstrates a relationship between the pressure of the dispersion and the amount of breakage. As the dispersion pressure increased, the median diameter of the particles decreased. That an increased in pressure would lead to more particle breakage was an expected result which has been shown by a number of previous studies with other chambers [42] [13] [5]. Without further studies at additional pressures, it is not possible to define a specific relationship between the pressure and amount of particle breakage for the ascorbic acid for comparison to other results, but the general trend is in the expected direction.

CHAPTER 8

SUMMARY AND FUTURE WORK

The objective of this thesis was to design and implement a DIH imaging system capable of analyzing dust particles as they are dispersed through a nozzle into an enclosed chamber and to use this system to quantify and characterize the particle breakage behavior. In order to capture holographic images, an optical system was designed, modeled, built, and successfully used to capture holographic videos. A dust dispersion system and testing chamber were constructed to control the dust flow parameters throughout the dispersion process. Testing this system provided empirical relationships between the pressure, solenoid timing, and chamber fill timing, which provided a road map of the adjustments necessary for control of the flow parameters in the system.

Resolution analysis was performed with and without a magnifying lens. The objects of focus in the analysis included a USAF resolution target, sugar particles, and lycopodium particles. The resolution results collected without the lens resulted in an average of 20.31 µm for the in-plane image resolution and a residual standard error (RSE) between 80.41 -146.19 µm for the axial depth measurement. The USAF target had the least error between the three objects, and the lycopodium particles had the most. Since the USAF target has the most clearly defined edges compared to the dust particles, it makes sense that it would have the highest level of resolution and the least amount of error. Sugar being more resolvable than lycopodium points to the pixel size and image quality being a more prominent cause of the measurement error than the reconstruction method.

When adding a camera lens with a magnification factor of 4.63x, the in-plane image resolution improved to an average of 10.51 µm, and the RSE of the axial depth was 66.63 µm for the USAF target and 98.58 µm for the lycopodium.

While all of these results show improved resolution with the addition of the lens, it is not a linear relationship between the decrease in relative particle size and an increase in resolution. This indicates that the lens introduces some error into the measurement process that has not been accounted for. Further studies and research into other magnification lenses may be necessary to improve the resolution further. The in-plane image resolution data collected in this work is valuable in quantifying the uncertainty of the particle diameters. The axial or depth resolution will become applicable for future work where the holographic images are used to locate particles in three-dimensional space with the end goal of recording the three-dimensional velocity field of the dust flow into the chamber.

Measurements of the change in the distribution of particle diameters for lycopodium and ascorbic acid showed a negligible ($< 15\%$) decrease for the lycopodium particles but a significant ($> 50\%$) decrease for ascorbic acid dust. The likely cause of this decrease is particle breakage as the dust is forced up the pipe, through the nozzle, and allowed to mix in the chamber. Presently, the amount of breakage occurring at each location has not been determined, but this question provides a possible avenue for future research. The percentage of particle breakage for these two materials and the increase in breakage at higher pressures for brittle materials are similar to dust particle breakage results from dispersions in the 20-L Siwek chamber. This agreement with past results validates using the holographic imaging technique in combination with this optic and dust dispersion system design for further investigation of dust particle breakage during dispersion into combustion testing chambers.

8.1 Future Work

While the resolution analysis conducted in Chapter 5 provides a solid baseline for the accuracy and precision of the particle sizing and locating results obtained with this holographic imaging system, there are several paths for expanding this analysis. The holographic images were reconstructed using the PECA and Hybrid method, but many other reconstruction algorithms are available. Since the actual particle breakage measurement was conducted using the HoloSand set of MATLAB functions, it would be insightful to organize the HoloSand functions into a resolution analysis program for comparison with the results from ResAnalysis. The method used in this resolution study could also be expanded to compare some of the other commercially available holographic imaging software packages or benchmark a newly designed program optimized for use in dust dispersion and combustion research.

Due to time limitations, dispersions of only two dust materials and a couple of pressures were completed and thoroughly analyzed. Continuing analysis of dust dispersions using this experimental system could encompass different materials at multiple pressures, utilizing different nozzle sizes or designs. Ideally, a complete design of experiments would be used to quantify the effect that each variable has on the particle breakage that occurs during dispersion.

Although this work has shown holography to be a valuable method for recording the particle size distribution throughout the dispersion process, the real strength of holographic imaging is the ability to locate and track particles in three-dimensional space for use in PIV. The recent work of Schweizer et al. [44] has provided a proof of concept for the use of HoloSand in the measurement of velocity profiles in dust combustion chambers. One limitation of that study was the use of a modified Hartmann tube, which does not contain a dispersion nozzle. Consequently, these results do not apply to either the 20-L Siwek or the 1 m^3 chambers. The holographic system developed in this paper is better suited for measuring particle flows with a nozzle dispersion system and, therefore, would provide more insight into the particle kinetics in the Siwek and 1 m^3 chamber.

One obstacle to overcome in recording three-dimensional near-nozzle high-speed flows is distortion of the laser caused by shock waves created when the flow exiting the nozzle becomes supersonic. This distortion obstructs the view of particles exiting the nozzle and prevents sizing or flow tracking directly next to the nozzle exit. To measure particle size distributions, the widow was moved approximately an inch above the nozzle and away from this shock wave as it was not critical to measure particle size directly at the nozzle exit. If imaging at the nozzle becomes an area of interest for future work, Mazumdar et al. have developed a novel method for canceling out shockwaves distortion through DIH [31] which would be worth investigating further.

REFERENCES

[1] Juliana Kuhlmann Abrantes. *Holographic Particle Image Velocimetry for Wall Turbulence Measurements*. PhD thesis, Ecole Centrale de Lille, 2012.

[2] Mike Adams, Thomas M. Kreis, and Werner P. O. Jueptner. Particle Size and Position Measurement with Digital Holography. *Optical Inspection and Micromeasurements II*, 3098(September 1997):234–240, 1997.

[3] Paul R. Amyotte and Michael J. Pegg. Lycopodium dust explosions in a hartmann bomb: effects of turbulence. *Journal of Loss Prevention in the Process Industries*, 2(2):87 – 94, 1989.

[4] Pranav Bagaria, Qiang Li, Ashok Dastidar, and Chad Mashuga. Classification of particle breakage due to dust dispersion. *Powder Technology*, 342:204–213, 2019.

[5] Pranav Bagaria, Jiaqi Zhang, Entao Yang, Ashok Dastidar, and Chad Mashuga. Effect of dust dispersion on particle integrity and explosion hazards. *Journal of Loss Prevention in the Process Industries*, 44:424–432, 2016.

[6] Solomon Barkley, Thomas Dimiduk, Jerome Fung, David Kaz, Vinothan N. Manoharan, Ryan McGorty, Rebecca Perry, and Anna Wang. Holographic Microscopy with Python and HoloPy. *Computing in Science and Engineering*, pages 1–8, 2019.

[7] G. Bradski. The OpenCV Library. *Dr. Dobb's Journal of Software Tools*, 2000.

[8] Richard Siwek Christoph Cesana. *Manual for 20-L Apparatus*. Cesana AG, 2020.

[9] A. E. Dahoe, R. S. Cant, M. J. Pegg, and B. Scarlett. On the transient flow in the 20-liter explosion sphere. *Journal of Loss Prevention in the Process Industries*, 14(6):475–487, 2001.

[10] Reetam Das. Digital in-line holography of blood atomization. Master's thesis, Iowa State University, 2019.

[11] A. Di Benedetto, V. Di Sarli, and P. Russo. On the determination of the minimum ignition temperature for dust/air mixtures. *Chemical Engineering Transactions*, 19:189–194, 2010.

[12] Valeria Di Sarli, Enrico Danzi, Luca Marmo, Roberto Sanchirico, and Almerinda Di Benedetto. CFD simulation of turbulent flow field, feeding and dispersion of non-spherical dust particles in the standard 20-L sphere. *Journal of Loss Prevention in the Process Industries*, 62(October):103983, 2019.

[13] Valeria Di Sarli, Roberto Sanchirico, and Almerinda Di Benedetto. On the effect of initial pressure on the minimum explosive concentration of dust in air. *Powder Technology*, 336:567–572, 2018.

[14] Bing Du, Weixing Huang, Long Liu, Tan Zhang, Hao Li, Yidan Ren, and Hanlin Wang. Visualization and analysis of dispersion process of combustible dust in a transparent Siwek 20-L chamber. *Journal of Loss Prevention in the Process Industries*, 33:213–221, 2015.

[15] Zdzislaw Dyduch, Adrian Toman, and Wojciech Adamus. Measurements of turbulence intensity in the standard 1 m3 vessel. *Journal of Loss Prevention in the Process Industries*, 40:180–187, 2016.

[16] R. K. Eckhoff. Current status and expected future trends in dust explosion research. *Journal of Loss Prevention in the Process Industries*, 18(4-6):225–237, 2005.

[17] United States Air Force. Photographic Lenses. Military Standard MIL-STD-150A, Department of Defense, May 1959.

[18] Jian Gao, Daniel R. Guildenbecher, Phillip L. Reu, and Jun Chen. Uncertainty characterization of particle depth measurement using digital in-line holography and the hybrid method. *Optics Express*, 21(22):26432, 2013.

[19] J.W. Goodman. *Introduction to Fourier Optics*. Electrical Engineering Series. McGraw-Hill, 1996.

[20] Daniel Guildenbecher. Sandia particle holography processor v. 1.0, version 00, 12 2015.

[21] Daniel R. Guildenbecher, Jian Gao, Phillip L. Reu, and Jun Chen. Digital holography simulations and experiments to quantify the accuracy of 3D particle location and 2D sizing using a proposed hybrid method. *Applied Optics*, 52(16):3790–3801, 2013.

[22] FLIR Systems Inc. ”How to Evalute Camera Sensitivity: Comparing camera performance using the EMVA1288 imaging performance standard”. Technical report, FLIR, 2018.

[23] Gareth James. *An Introduction to Statistical Learning: with Applications in R (Springer Texts in Statistics)*. Springer, sep 2017.

[24] Omotayo Kalejaiye, Paul R. Amyotte, Michael J. Pegg, and Kenneth L. Cashdollar. Effectiveness of dust dispersion in the 20-L Siwek chamber. *Journal of Loss Prevention in the Process Industries*, 23(1):46–59, 2010.

[25] Myung K. Kim. Principles and techniques of digital holographic microscopy. *SPIE Reviews*, 1(1), 2010.

[26] Thomas M. Kreis. Frequency analysis of digital holography. *Optical Engineering*, 41(4):771, 2002.

[27] Thomas M. Kreis. Frequency analysis of digital holography with reconstruction by convolution. *Optical Engineering*, 41(8):1829, 2002.

[28] Lumentum. *Helium-Neon Laser Heads 1100 Series*, 2019.

[29] Kevin Mallery and Jiarong Hong. Regularized inverse holographic volume reconstruction for 3D particle tracking. *Optics Express*, 27(13):18069, 2019.

[30] Manoharan Lab, Harvard University. *HoloPy Documentation*, November 2020.

[31] Yi Chen Mazumdar, Michael E. Smyser, Jeffery D. Heyborne, Mikhail N. Slipchenko, and Daniel R. Guildenbecher. Megahertz-rate shock-wave distortion cancellation via phase conjugate digital in-line holography. *Nature Communications*, 11(1):1–10, 2020.

[32] David B. Mercer, Paul R. Amyotte, Debbie J. Dupuis, Michael J. Pegg, Arief Dahoe, Wouter B.C. De Heij, John F. Zevenbergen, and Brian Scarlett. The influence of injector design on the decay of pre-ignition turbulence in a spherical explosion chamber. *Journal of Loss Prevention in the Process Industries*, 14(4):269–282, 2001.

[33] Raul Casta neda and Jorge Garcia-Sucerquia. Single-shot 3d topography of reflective samples with digital holographic microscopy. *Appl. Opt.*, 57(1):A12–A18, Jan 2018.

[34] Georges Nemetallah, Rola Aylo, and Logan Williams. *Analog and digital holography with MATLAB*. SPIE Press, Bellingham, Washington, 2015.

[35] Russell A. Ogle. *Dust Explosion Dynamics*. Elsevier, Cambridge, MA, 2017.

[36] G. Pan and Hui Meng. Digital in-line holographic piv for 3d particulate flow diagnostics. *Proceedings of 4th International Symposium on Particle Image Velocimetry*, 01 2001.

[37] Gang Pan and Hui Meng. Digital holography of particle fields: reconstruction by use of complex amplitude. *Applied Optics*, 42(5):827, 2003.

[38] Photron. *Mini AX Fastcam*, 2019.

[39] Ye Pu and H. Meng. An advanced off-axis holographic particle image velocimetry (HPIV) system. *Experiments in Fluids*, 29(2):184–197, 2000.

[40] U.S. Chemical Safety and Hazards Investigation Board. Csb releases call to action on combustible dust hazards. `https://www.csb.gov/csb-releases-call-to-action-on-combustible-dust-hazards/`, October 2018. (Accessed on 04/05/2021).

[41] U.S. Chemical Safety and Hazards Investigation Board. Dust incidents 2006-2017. `https://www.csb.gov/assets/1/6/csb_dust_incidents.pdf`, 2018. (Accessed on 04/05/2021).

[42] Roberto Sanchirico, Valeria Di Sarli, Paola Russo, and Almerinda Di Benedetto. Effect of the nozzle type on the integrity of dust particles in standard explosion tests. *Powder Technology*, 279:203–208, 2015.

[43] Ulf Schnars. *Digital holography : digital hologram recording, numerical reconstruction, and related techniques*. Springer, Berlin, 2005.

[44] Christian Schweizer, Shrey Prasad, Ankit Saini, Chad V. Mashuga, and Waruna D. Kulatilaka. High-speed digital in-line holography for in-situ dust cloud characterization in a minimum ignition energy device. *Powder Technology*, 376:612–621, 2020.

[45] Sidney A. Self. Focusing of spherical Gaussian beams. *Applied Optics*, 22(5):658, 1983.

[46] Thorlabs, Inc. *K310-Spatial Filter*.

[47] Thorlabs, Inc. *Principles of Spatial Filters*.

[48] Mostafa Toloui and Jiarong Hong. High Fidelity Digital Inline Holographic Method for 3D Flow Measurements. *Optics Express*, 23(21):321–342, 2015.

[49] Jingjie Yuan, Weixing Huang, Bing Du, Niansheng Kuai, Zongshan Li, and Jingyi Tan. An extensive discussion on experimental test of dust minimum explosible concentration. *Procedia Engineering*, 43:343–347, 2012.